NORTHWESTERN UNIVERSITY

Mechanics and Electromagnetic Modeling of Injectable, Implantable, and Skin Integrated Electronics.

A DISSERTATION

SUBMITTED TO THE GRADUATE SCHOOL
IN PARTIAL FULFILLMENT OF THE REQUIREMENTS

for the degree

DOCTOR OF PHILOSOPHY

Mechanical Engineering

By

Raudel Avila

EVANSTON, ILLINOIS

June 2023

ABSTRACT

Mechanics and Electromagnetic Modeling of Injectable, Implantable, and Skin Integrated Electronics.

Raudel Avila

Bio-integrated electronics with advanced monitoring capabilities have garnered considerable interest as a means of expanding patient care beyond traditional hospital and clinic settings. These mechanically soft microsystems, many of which are bioresorbable and wireless, have the potential to replace bulky, rigid, and wired medical technologies by matching or exceeding their performance. Combined advances in material science, mechanical engineering, and electrical engineering form the foundations of thin, soft electronic/optoelectronic platforms that have unique capabilities in wireless monitoring and control of various biological processes in cells, tissues, and organs through different characterization and/or stimulation platforms (e.g., light/drugs). Biomedical applications typically involve a demanding set of considerations in material selection, performance, size, electromagnetic efficiency, and stretchability to enable compliant systems for control, power delivery, actuation, data processing, and/or communication.

In this dissertation, I examine the design and optimization of bioelectronics platforms through systematic numerical and analytical modeling. The goal is to identify scaling relationships and construct models from physical parameters related to mechanical and electromagnetic performance parameters to inform the development of skin-integrated and implantable bioelectronic platforms that can administer drugs in a programable fashion, wirelessly pace the heart, induce vibrotactile sensations at different tissue depths, and monitor physiological signals through mechanically compliant device architectures.

First, I examine injectable drug delivery systems with electrochemical actuation, which provide programmable volume and flow rates in miniaturized form factors. This technology is particularly useful for in vivo pharmacological experiments in freely moving animals where flow rate control and delivery time are important. However, for programmable drug delivery, the available flowrate and drug delivery time modeling strategies fail to consider key variables of the bioelectronics system – microfluidic resistance and flexible membrane stiffness. I present an analytical model that accounts for all the variables that influence drug delivery in non-dimensional parameters related to pressure, volume, and microfluidic channels. This approach does not require numerical simulations and allows for a faster system optimization based on a scalable understanding of the non-dimensional parameters for different *in vivo* experiments involving programmable drug delivery systems for neuroscience and clinical research.

Next, I consider a leadless, battery-free, fully implantable cardiac pacemaker for postoperative control of cardiac rate and rhythm. This device completely dissolves and is cleared by natural biological processes after a defined operating timeframe where the bioresorbable aspect is governed by a reaction-diffusion process between the biofluids and the pacemaker materials and geometries. I discuss the design and performance of this temporary device to effectively pace hearts of various sizes in mouse, rat, rabbit, canine, and human cardiac models, with tailored geometries and operating timeframes, powered by a wireless energy transfer link that relies on inductive coupling between an external transmission coil and the internal pacemaker. The safety and reliability of the device is examined in the context of thermal and electromagnetic exposure with biological tissues to ensure that the maximum temperature increase and specific absorption rate from the electromagnetic fields is below the safety limits. This bioresorbable approach

overcomes the key disadvantages of traditional temporary pacing devices and may serve as the foundation for the next generation of postoperative temporary and wireless pacing technology.

Then, I consider skin-integrated electronic platforms using vibro-tactile actuators for sensory perceptions in virtual or augmented reality applications. Through finite element modeling, and comparison with three-dimensional digital image correlation measurements, I investigate the vibrational dynamics induced by the three main classes of vibro-tactile actuators in a bilayer elastomer structure that captures essential mechanical properties of human skin to provide a fundamental understanding of the mechanics associated with coupling between vibro-tactile actuators and the skin. These studies examine the effects of key parameters relevant to the mechanics and resulting sensations, such as those related to contact area, actuation amplitude and spatiotemporal distributions of displacements in terms of both surface and body waves.

Lastly, I examine materials strategies and design concepts for enhanced mechanical performance and water diffusion in skin-integrated electronics used for continuous monitoring of vital signs in critically ill patients in neonatal and pediatric intensive care units (NICUs and PICUs). Current approaches require multiple sensors taped to the skin and connected via hard-wired interfaces to external data acquisition electronics. Through numerical modeling, I identify materials strategies and design concepts that significantly improve these skin-integrated platforms using optimized materials, open (i.e., “holey”) layouts and pre-curved designs to reduce the stresses at the skin interface, facilitate release of interfacial moisture from trans epidermal water loss and allow visual inspection of the skin for rashes or other forms of irritation.

ACKNOWLEDGEMENTS

During my time at Northwestern University, I had the pleasure of collaborating with and learning from an extraordinary group of people. First, I would like to express my deepest appreciation to my advisor Prof. Yonggang Huang and my mentor Dr. Yeguang Xue for hosting me during my summer 2016 Research Experience for Undergraduate which ultimately led me to join Northwestern University and pursue a Ph.D. in mechanics and electromagnetic modeling of bioelectronics. Second, I want to thank Prof. John A. Rogers for the extensive guidance and collaboration over six years and working with him and his group to elevate the impact of research by combining modeling and experiments. Third, I would like to thank Prof. Sinan Keten, Prof. Jiaxing Huang, and Prof. Q. Jane Wang for their time to serve as my dissertation committee members and writing letters of support for my future academic career. Fourth, I want to thank my colleagues in Huang's group: Prof. Zhaoqian Xie, Prof. Yujun Deng, Prof. Kan Li, Dr. Heling Wang, Dr. Haiwen Luan, Dr. Yeguang Xue, and Mr. Shupeng Li. Fifth, I want to thank my collaborators in Rogers' group: Prof. Yeonsik Choi, Dr. Yixin Wu, Dr. Aurelie Hourlier-Fargette, Ms. Claire Liu, Dr. Jean Won Kwak, Dr. Abraham Vazquez-Guardado, Ms. Joanna Ciatti, Dr. Da Som Yang, Prof. Kyeongha Kwon, Prof. Hyoyoung Jeong, Dr. Jin-Tae Kim, Dr. Geumbe Lee, Prof. Yei Hwan Jung, Prof. Di Lu, Dr. Sung Soo Kwak, Dr. Jae-Hwan Kim and Ms. Surabhi Madhvapathy. I would like to acknowledge the funding support during my Ph.D. from the National Science Foundation Graduate Research Fellowship, Ford Foundation Pre-Doctoral Fellowship, Walter P. Murphy Fellowship, and Terminal Year Fellowship. Lastly, I want to thank my family and many close friends of mine for their continued support over my Ph.D. journey.

PREFACE

The dissertation is submitted to The Graduate School of Northwestern University in partial fulfillment of the requirements for the Doctor of Philosophy degree in Mechanical Engineering. The work presented in the dissertation was conducted under the supervision of my advisor, Prof. Yonggang Huang, and in collaboration with Prof. John A. Rogers. My Ph.D. research focuses on fundamental theory and engineering modeling strategies to target emerging bioelectronics technologies to study the structural designs, soft materials mechanics, wireless platforms, and antenna designs for deployment of flexible and stretchable devices in healthcare and biomedical settings.

In wide cross-disciplinary collaborations, my main contribution is design and optimization of bioelectronics platforms including: injectable electrochemical microelectronics platforms for drug delivery, biocompatible and dissolvable pacemakers, ultra-soft biosensors with holey architectures for continuous monitoring of NICU and PICU patients, implantable optogenetic devices, bioresorbable temperature sensors, miniaturized pressure sensors for prosthetics, and skin-integrated vibrotactile sensors.

In this dissertation, I will not present the intricate experimental techniques such as device fabrication or the clinical test data and detailed set up. For additional information regarding these aspects, please consult the relevant journal publications. The author's publications related to these topics are available for reference (*denotes authors contributed equally):.

Chapter 1

1. Avila R., Li C., Xue Y., Rogers J.A., and Huang Y., "Modeling programmable drug delivery in bioelectronics with electrochemical actuation," *Proceedings of the National Academy of Sciences*, 2021, 118(11), e2026405118.
2. Avila R., Wu Y., Rogers J.A., and Huang Y., "A mechanics model for injectable microsystems in drug delivery," *Journal of the Mechanics and Physics of Solids*, 2021, 156, 104622.
3. Avila R., Ciatti J.L., Vazquez-Guardado A., Wu Y., Zhang Y., Garziera R., Rogers J.A., and Huang Y., "Electrochemical bioelectronics in drug delivery – effect of the initial gas volume," *Journal of Applied Mechanics*, 2022, 89(1), 011012.
4. Avila R., Wu Y., Garziera R., Rogers J.A., and Huang Y., "Analytical Modeling of Flowrate and Its Maxima in Electrochemical Bioelectronics with Drug Delivery Capabilities," *Research*, 2022, Article ID 9805932.

Chapter 2

1. Choi Y.S., Jeong H., Yin R.T., Avila R., Pfenniger A., Tzavelis A., Lee J.Y.,, Lee Y.J., Chen S.W., Kim S., Yoo J., Knight H.S., Ahn H., Wickerson G., Higbee-Dempsey E., Russo B.A., Napolitano M.A., Holleran T.J., Miniovich A.N, Lee G., Vázquez-Guardado A., Geist B., Kim B., Han S., Brennan J.A., Aras K., Kwak S.S., Kim J., Yang X., Burrell A., Chun K.S., Wu C., Rwei A.Y., Spann A.N., Banks A., Johnson D., Zhang Z.J., Haney C.R., Jin S.H., Sahakian A.V., Huang Y., Trachiotis G.D., Knight B.P., Arora R.K., Efimov I.R., and Rogers J.A., "A closed-loop network of wireless, body integrated devices for temporary electrotherapy," *Science*, **376**, 1006 (2022).

2. Choi Y.S., Yin R.T., Pfenniger A., Koo J., Avila R., Lee K.B., Chen S.W., Lee G., Li G., Qiao Y., Murillo-Berlioz A., Kiss A., Han S., Lee S.M., Li C., Xie Z., Chen Y.Y., Burrell A., Geist B., Jeong H., Kim J., Yoon H.J., Banks A., Kang S.K., Zhang Z.J., Haney C.R., Sahakian A.V., Johnson D., Efimova T., Huang Y., Trachiotis G.D., Knight B.P., Arora R.K., Efimov I.R., and Rogers J.A., "Fully implantable and bioresorbable cardiac pacemakers without leads or batteries," *Nature Biotechnology*, 39, 1228-1238 (2021).
3. Choi Y.S., Hsueh Y.Y., Koo J., Yang Q., Avila R., Hu B., Xie Z., Lee G., Ning Z., Liu C., Xu Y., Lee Y.J., Zhao W., Fang J., Deng Y., Lee S.M., Vázquez-Guardado A., Stepien I., Yan Y., Song J.W., Haney C., Oh Y.S., Liu W., Yun H.J., Banks A., MacEwan M.R., Ameer G.A., Ray W.Z., Huang Y., Xie T., Franz C.K., Li S., Rogers J.A., "Stretchable, dynamic covalent polymers for soft, long-lived bioresorbable electronic stimulators designed to facilitate neuromuscular regeneration," *Nature Communications*, 11, 1-14, 2020.

Chapter 3

1. Kim J.*, Shin H.*, Yoo J.*, Avila R.*, Huang Y., Jung Y., Colgate J., and Rogers J.A., "Mechanics of Vibrotactile Sensors for Applications in Skin-Interfaced Haptic Systems," *Extreme Mechanics Letters.* 2022, 101940.

Chapter 4

1. Kwak S.S.*, Yoo S.*, Avila R.*, Chung H.U.*, Jeong H., Liu C., Vogl J.L., Kim J., Park Y., Ryu H., Yoon H.J., Kim J., Koo J., Oh Y.S., Kim S.B., Xu S., Xie Z., Huang Y., and Rogers J.A., "Skin-integrated devices with soft, holey architectures for wireless

physiological monitoring, with applications in the neonatal intensive care unit," *Advanced Materials*, 2021, 2103974.

If there are any unclear expressions or explanations in this dissertation, please refer to the journal publication for a complete description and details of both modeling and experimental methods.

Raudel Avila

Evanston, Illinois

March 2023

TABLE OF CONTENTS

LIST OF TABLES

LIST OF FIGURES

function $f(V)$ is obtained from finite element analysis (FEA) using the Marlow hyperelastic. The maximum flowrate is labeled as the peak value of the flowrate temporal profile. (B) representative example of the flowrate temporal profile showing the analytical slow + fast solution where the function $f(V)$ is obtained from bending-dominated deformation. The dimensions of the flexible membrane are thickness h = 150 μm and radius R_0 = 1.20 mm. The electrical current is 0.5 mA and the cross section of the microchannels is 50 μm The three non-dimensional values are M^* = 0.0009, P_0^* = 0.1013, and V_0^*= 0.9162.

Figure 1.12. Maximum Flowrate. (A) drug delivery temporal flowrate showing the maximum (peak) flowrate value when the electrical current changes from 0.10 mA to 1.00 mA. (B) maximum flowrate as a function of the electrical current. The dimensions of the flexible membrane are thickness h = 150 μm and radius R_0 = 1.20 mm. The cross section of the microchannels is 50 μm The two non-dimensional values are P_0^* = 0.1013, and V_0^*= 0.9162. 81

Figure 1.13 Parametric Study of the Maximum Flowrate. Changes in the maximum flowrate when (A) the microchannel cross-section is reduced from 50 μm to 18 μm which increases the non-dimensional parameter M^*, (B) the electrolyte chamber goes from full to partially full (50%) which introduces an initial gas volume via the non-dimensional parameter V_0^* , and (C) the initial environmental pressure in the 84

tissue/organ changes which affects the non-dimensional parameter P_0^*. The dimensions of the flexible membrane are thickness h = 150 μm and radius R_0 = 1.20 mm.

Figure 2.1. Materials, design, and proposed utilization of a bioresorbable, implantable, leadless, battery-free cardiac pacemaker. (A) Schematic illustration of the device mounted on the myocardial tissue. The electronic component consists of three functional parts: a wireless receiver, a radiofrequency *PIN* diode, and a dielectric interlayer. All components of the device naturally bio resorb via hydrolysis and metabolic action in the body. (B) Images of dissolution of a device associated with immersion in PBS (pH = 7.4) at physiological temperature (37°C). Scale bar, 10 mm. (C) Schematic illustration of the wireless and battery-free operation of an implanted device via inductive coupling between an external transmission coil (Tx) and the receiver (Rx) coil on the device. (D) Bio resorption thereby eliminates the device after a period of therapy, to bypass needs for device removal. 92

Figure 2.2 Long-range electromagnetic characteristics of bioresorbable, leadless cardiac pacemakers. Simulated results of the electromagnetic field distribution near the coupled Rx and Tx coils for a separation distance of (left) 3 mm and (right) 20 mm (transmitting power = 1 W). 95

Figure 2.3. Electrical performance characteristics of the wireless power transfer 97

system. (A) Schematic illustration of the circuit diagram for the transmission of RF power at ~13.5 MHz. (B) Measured RF behavior of the stimulator (black, S_{11}; red, phase). (C) Simulation results for inductance (*L*) and Q factor as a function of frequency. (D) An alternating current (sine wave) applied to the Tx coil. (E) Example direct current output of ~13.2 V wirelessly generated via the Rx coil of the bioresorbable device. (F) Output voltage as a function of transmitting frequency. (G) Output voltage as a function of the distance between the Tx and Rx coils (transmitting voltage = 10 V_{pp}; transmitting frequency = ~13.5 MHz).

Figure 2.4. Electromagnetic characteristics of bioresorbable, leadless cardiac pacemakers with various sizes of wireless power harvesting units. The sizes of the Rx coils are 25 (blue), 18 (red), 12 (black), and 8 mm (green). (A) Simulated scattering parameters (S11) of the wireless power harvesting units with different sizes of receiver coils. The resonance frequency of each coil is 4.24, 8.03, 13.91, 17.33 MHz, respectively. (B) Simulated Q factors of the wireless power harvesting units, respectively. (C) Experimental results for the output voltage as a function of input voltage at a coil-to-coil distance of ~1 mm and load resistance of 5 kΩ. (D) Simulated power transfer efficiency as a function of changes in coil-to-coil distance. 99

Figure 2.5. Long-range wireless operation *in vitro* test of a bioresorbable cardiac pacemaker system. (A) Schematic illustrations of three different designs of Tx coil: (i) Tx coil I (solenoid type; 4 turns; 35 mm diameter); (ii) Tx coil II (solenoid type; 4 100

turns; 100mm diameter); Tx coil III (square; 1 turn; 260 × 280 mm^2). (B) Photograph of bioresorbable pacemaker (diameter of Rx coil = 25 mm) and Tx coil II. Scale bar, 50 mm. (C) Wireless energy transfer through slices of pork with thicknesses of 20 mm. (D) Wireless energy transfer through slices of pork with thicknesses of 120 mm. Changes in output power of the bioresorbable pacemaker as a function of coil-to-coil distance (input frequency = 13.56 MHz; Input power = 2-12 W; load resistance = 5000 Ω): (E) Tx coil I; (F) Tx coil II; (G) Tx coil III.

Figure 2.6. Computational results for distributions of the electric field within the cardiac tissue and relationships to design parameters associated with the contact electrodes in (A) three-dimensional (3D) and (B) two-dimensional (2D; x, z-axis) space, respectively. (C) Simulated range of electric field at electric field of 100 mV/mm as a function of electrode spacing with different input voltage (black, 0.5 V; red, 1.0 V; blue, 1.5 V; green, 2.0 V; violet, 2.5 V). 102

Figure 2.7. Modeling and experimental studies of mechanical reliability of the bioresorbable, leadless cardiac pacemaker. (A) Photograph (left) and FEA (right) results for devices during compressive buckling (20%). (B) Photograph of twisted by 180°, (C) and (D) bent (bend radius = 4 mm) devices. (E) Output voltage of a device as a function of bending radius (left), compression (middle), and twist angle (right) at different distances between the Rx and Tx coils (black, 1 mm; red 6 mm). (n = 3 independent samples). Scale bar, 10 mm. 104

of the hole spacing, using measured diffusion coefficients (5.56 x10^{-7} m^2/min at 25^{o}C and 1.18 x 10^{-6} m^2/min at 35^{o}C).

Figure 4.8. Modeling results of diffusion for different hydrogel adhesive designs at 25^{o}C and 35^{o}C. (A) Schematic illustration of the device attached on the skin using the hydrogel adhesive. (B) Three hydrogel adhesive designs such as non-holey, holey, and holey with microchannels. (C) Normalized water concentration as a function of time for hydrogel swelling at 25^{o}C and 35^{o}C for three hydrogel adhesive designs. 146

CHAPTER 1

Modeling Electrochemical Bioelectronics in Programmable Drug Delivery Applications

Drug delivery systems featuring electrochemical actuation represent an emerging class of biomedical technology with programmable volume/flowrate capabilities for localized delivery. Recent work establishes applications in neuroscience experiments involving small animals in the context of pharmacological response. However, for programmable delivery, the available flowrate control and delivery time models fail to consider key variables of the drug delivery system – microfluidic resistance and membrane stiffness. Here we establish an analytical model that accounts for the missing variables and provides a scalable understanding of each variable's influence in the physics of delivery process (i.e., maximum flowrate, delivery time). This analytical model accounts for the key parameters – initial environmental pressure, initial volume, microfluidic resistance, flexible membrane, current and temperature – to control the delivery and bypasses numerical simulations allowing faster system optimization for different *in vivo* experiments. We show that the delivery process is controlled by 3 non-dimensional parameters, and the volume/flowrate results from the proposed analytical model agree with the numerical results and experiments. These results have relevance to the many emerging applications of programmable delivery in clinical studies within the neuroscience and broader biomedical communities.

Background

1.1. Drug delivery techniques for treatment, cure, diagnosis, and prevention of illnesses have substantially evolved from systemic absorption of pharmacological agents through tissue membranes to localized drug release in regions of interest [1]. Modern drug delivery methods help researchers study the effects of a medication intended for a specific body region while decreasing the potential side effects from unwanted interactions in other body regions [2]. In drug delivery, the effect of pharmacological ingredients, drug amount, target regions, delivery rates, and dosage time, varies between delivery approaches [1,3] ranging from ubiquitous ingestible tablets/capsules to injectable microsystems.

The growing opportunities in localized delivery and clinical research motivated the development of microsystems for volume and flowrate control [4–10] in pharmacological experiments involving small animals [11–19]. Design of implantable microsystems requires compact size, power consumption, and biocompatible material considerations19 that vary between actuation methods (e.g., magnetic, thermal, optical, mechanical, or electrochemical) to deliver the drug without complications [9]. A biocompatible encapsulation limits any negative effects derived from implantation or during continuous operation while in proximity with surrounding tissues/fluids. Excessive thermal heating and high-power consumption can 1) affect animal behavior and damage the implanted region and 2) require bulk electronics (i.e., battery) that increase the size and overall weight of the microsystem.

In implantable delivery systems, electrochemical actuation offers 1) low power consumption, 2) negligible heat generation, 3) reconfigurable volume sizes (e.g., small or large drug reservoirs), 4) higher flowrates and fast response time [9,20], 5) simplified implantation and

unrestricted movement of animals for in vivo studies, and in some cases 6) refillable [7,15,16,21] for repeated studies. Wireless electrochemical actuation features an inductive link to harvest the electrical current applied to a set of interdigitated electrodes in contact with an electrolyte solution and initiate the chemical reaction [22–26]. Continuous gas formation (i.e., hydrogen H_2 and oxygen O_2) gradually increases the pressure inside the electrolyte reservoir to deform a flexible polymer membrane [15,16, 22, 27] pushing the drug via partially implanted microchannels to the target region inside the animal. Figure 1.1 illustrates the schematics of an electrochemical pump. Electrochemical actuation systems have been used to target localized delivery of insulin [28], cancer agents [29,30], hormone [31] and intraocular [21] drug delivery, as well as therapeutic drug studies [4,32].

In 2019, a wireless, battery-free, and refillable electrochemical microsystem combined optogenetic and pharmacological stimulation in a single experiment with programmable flowrates and unrestricted animal movement [15,16]. These miniaturized injectable devices overcome the limitations of supplementary hardware required in combined stimulation and offer compatible form factors for large-scale manufacturing, making it a suitable option for widespread use in animal behavioral studies [31,33,34] where accurate control of volume and flowrate are critical. Programmed drug delivery influences the pharmacodynamic response in the animals [31] and excessively high or low rates can damage neighboring tissues or block the microfluidic channels [15], respectively. To predict the fluid delivery rates, a linear relationship between the effective current and flowrate has been used in the past [35,36]. However, this model neglects the microfluidic resistance and flexible membrane mechanics and overestimates the flowrate [15]. Recently, a numerical model, derived from the rate form of the ideal gas law, was proposed and it

accounts for the 1) microfluidic cross-sectional area and length, and 2) flexible membrane elasticity [16]. Still, the model requires extensive numerical simulations to predict volume and flowrates, and it is difficult to find time scaling relationships for drug delivery. Here, we develop an analytical model that gives an accurate relation between the current and flowrate and offers a simple analytical solution of the drug delivery process, while considering all important factors in the microsystem design, including microchannel and flexible membrane which are difficult to account for in prior studies, without the need for numerical simulations. The flexible membrane effects were derived from mechanics theory for an arbitrary flexible polymer and used in the volume and flowrate calculations. Motivated by the ongoing adoption of implantable electrochemical microsystems in drug delivery, the analytical model described in the following identifies the key parameters that control the volume and flowrate during the drug delivery and gives researchers much larger design space (e.g., geometrical, flexural, and fluidic) for electrochemical microsystems in future clinical studies. This chapter presents results from experiments and previous numerical models to validate the proposed theory.

1.2.

Modeling Drug Delivery

Figure 1.1 illustrates the drug delivery process using electrochemical actuation where electrical current i in the interdigitated electrodes initiates (Figure 1.1A) a chemical reaction that increases the pressure P inside the electrolyte reservoir due to gas formation. The buildup pressure continuously deforms the flat flexible polymer membrane (Figure 1.1B) into a spherical cap and pushes the drug out of the reservoir through a network of microfluidic channels and into the target

delivery region (Figure 1.1C). For electrochemical actuation devices, the drug delivery process can be derived from the ideal gas law $P(V + V_0) = nRT$ by writing the rate form as

$$\dot{P}(V + V_0) + P\dot{V} = \dot{n}RT \tag{1.1}$$

where P is the pressure, V_0 and V are the initial gas volume and volume change inside the electrolyte reservoir, respectively, $\dot{n} = \frac{3i}{4F}$ is the gas generation rate related to the effective current i and F is the Faraday's constant, R is the ideal gas constant, and T the temperature. The force equilibrium gives

$$P = \frac{12\mu L\dot{V}}{ab^3\left(1 - 0.63\frac{b}{a}\right)} + f(V) + P_0 \tag{1.2}$$

where the first term $\frac{12\mu L\dot{V}}{ab^3\left(1-0.63\frac{b}{a}\right)}$ represents the microfluidic resistance [37, 38] for a rectangular cross-section, a, b, and L are the width, height, and length of the delivery channel (Figure 1.1), respectively, and μ is the viscosity of the drug (valid for b < a, for a square cross-section it simplifies ~ $\frac{32\mu L\dot{V}}{a^4}$); the second term $f(V)$ is the pressure needed to deform the flexible membrane leading to the volume change V inside the electrolyte reservoir, and this pressure-volume relationship $f(V)$ of the flexible membrane could be determined numerically by the finite element analysis (FEA) as in prior studies, but now completely analytical as discussed later in this paper; and the third term P_0 is the initial environmental pressure.

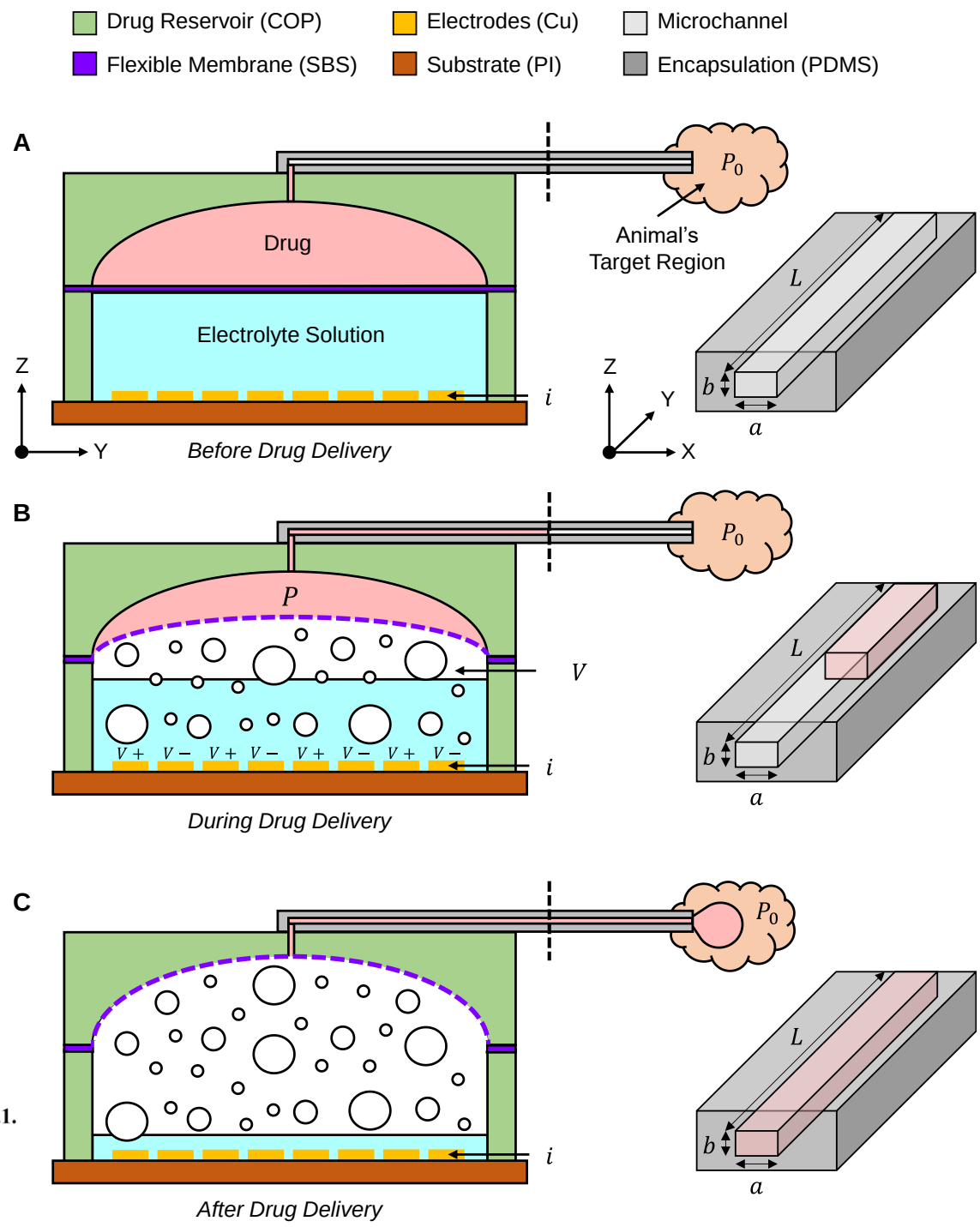

Figure 1.1.

Schematic diagram of the electrochemical micropump system. (A) Before, (B) During, and (C) After the drug delivery process highlighting the relevant volume, pressure, and microchannel parameters in the drug delivery process.

Substituting the gas generation rate and pressure into Eq. 1.1 yields a second order ordinary-differential-equation (ODE) of the form

$$\left[\frac{32\mu L}{a^4}\ddot{V} + f'(V)\dot{V}\right](V + V_0) + \left[\frac{32\mu L}{a^4}\dot{V} + f(V) + P_0\right]\dot{V} = \frac{3iRT}{4F} \tag{1.3}$$

that describes the drug delivery process with square cross-section microfluidic channels. Eq. 1.3 was solved numerically [15,16] with the initial conditions $V(t = 0) = 0$, and $\dot{V}(t = 0) = 0$ to determine the delivered drug volume and flowrate versus time. The numerical solution of Eq. 1.3, while very useful, fails to provide a scalable understanding of each parameter in drug delivery.

The following non-dimensional variables and parameters are introduced: normalizing pressure terms P, $f(V)$ and P_0 by the ratio $\frac{Eh}{R_0}$, where E, h and R_0 are the flexible membrane Young modulus, thickness, and radius, respectively; normalizing the volume terms by R_0^3, i.e., $V_0^* = \frac{V_0}{R_0^3}$ and $V^* = \frac{V}{R_0^3}$; rewriting the function $f(V)$ by a normalized function $\frac{Eh}{R_0}G\left(\frac{V}{R_0^3}\right)$, where G is a non-dimensional function; and introducing a non-dimensional time of the form $t^* = t\left(\frac{3iRT}{4FEhR_0^2}\right)$. Eq. 1.3 can then be rewritten non-dimensionally as

$$\left[M^*\frac{d^2V^*}{dt^{*2}} + G'(V^*)\frac{dV^*}{dt^*}\right](V^* + V_0^*) + \left[M^*\frac{dV^*}{dt^*} + G(V^*) + P_0^*\right]\frac{dV^*}{dt^*} = 1 \tag{1.4}$$

where the non-dimensional parameter $M^* = \frac{24\mu L}{a^4}\frac{iRTR_0^2}{Fh^2E^2}$ represents the microfluidic resistance and it combines the effects of microfluid channel (a and L), drug (μ), flexible membrane (E, h and R_0), current (i) and temperature (T); and $V_0^* = \frac{V_0}{R_0^3}$, and $P_0^* = \frac{P_0 R_0}{Eh}$ represent the initial volume and initial environmental pressure, respectively. These three non-dimensional parameters control the drug delivery process. We integrate Eq. 1.4 to yield the following first-order ODE for V^*

$$(V^* + V_0^*)\left[M^*\frac{dV^*}{dt^*} + G(V^*)\right] + V^*P_0^* - t^* = 0 \tag{1.5}$$

with the initial conditions $V^*(t^* = 0) = 0$.

For vanishingly small M^*, i.e., negligible microfluidic resistance, the equation above is simplified to the following

$$t^* = (V^* + V_0^*)\,G(V^*) + V^*P_0^* \tag{1.6}$$

which gives the normalized time in terms of the normalized drug volume (and initial environmental pressure P_0^* and initial volume V_0^*). It is useful to estimate the drug delivery time $t_{delivery}$ for a given drug volume V, and $t_{delivery}$ is linear with respect to V_0^* and P_0^*. Its inverse, i.e., the drug volume versus time, is denoted by $V_{SOL}^*(t^*)$, which is the solution of Eq. 1.5 at the limit M^*=0, though it does not satisfy the initial condition $\dot{V}(t = 0) = 0$.

1.2.1. Derivation of the Analytic Solution using Perturbation Analysis

For small but non-vanishing M^* (i.e., accounting for the microfluidic resistance), Eq. 1.5 is solved by the singular perturbation method as

$$V^* = V^*_{SOL}(t^*) - \frac{M^*}{V^*_0\left(\frac{64h^2}{3\pi R_0^2} + \frac{P^*_0}{V^*_0}\right)^2}\left[1 - e^{-\left(\frac{64h^2}{3\pi R_0^2}+\frac{P^*_0}{V^*_0}\right)\frac{t^*}{M^*}}\right] \tag{1.7.1}$$

where the first term on the right-hand side is the solution of Eq. 1.6, the second term decays exponentially with time, and together they satisfy the initial condition $\dot{V}(t=0) = 0$. The derivation and perturbation solution are detailed next.

The rate form of the ideal gas law after substituting the microfluidic (for a square cross-section) and membrane resistance and gas generation rate in Eq. 1.3 is copied below

$$\left[\frac{32\mu L}{a^4}\ddot{V} + f'(V)\dot{V}\right](V + V_0) + \left[\frac{32\mu L}{a^4}\dot{V} + f(V) + P_0\right]\dot{V} = \frac{3iRT}{4F} \tag{1.7.2}$$

With the pressure terms normalized by $\frac{Eh}{R_0}$ [e.g., $P^*_0 = \frac{P_0 R_0}{Eh}$ and $f(V) = \frac{Eh}{R_0}G\left(\frac{V}{R_0^3}\right)$, where G is a nondimensional function], the volume terms normalized by R_0^3 (e.g., $V^*_0 = \frac{V_0}{R_0^3}$, and $V^* = \frac{V}{R_0^3}$), and normalized time $t^* = t\left(\frac{3iRT}{4FR_0^2hE}\right)$, the above equation becomes

$$\left[\frac{24\mu L}{a^4}\frac{iRTR_0^2}{Fh^2E^2}\frac{d^2V^*}{dt^{*2}} + G'(V^*)\frac{dV^*}{dt^*}\right](V^* + V_0^*) \tag{1.7.3}$$

$$+\left[\frac{24\mu L}{a^4}\frac{iRTR_0^2}{Fh^2E^2}\frac{dV^*}{dt^*} + G(V^*) + P_0^*\right]\frac{dV^*}{dt^*} = 1$$

In addition to the normalized initial volume V_0^* and initial environmental pressure P_0^*, Eq. 1.7.3 features another non-dimensional parameter $M^* = \frac{24\mu L}{a^4}\frac{iRTR_0^2}{Fh^2E^2}$ representing the normalized microfluidic resistance. The above equation, can be rewritten in the form $\frac{d}{dt^*}\left[(V^* + V_0^*)\left(M^*\frac{dV^*}{dt^*} + G(V^*) + P_0^*\right)\right] = 1$. Its integration, together with the initial conditions $V(t=0) = 0$, and $\dot{V}(t=0) = 0$, give Eq. 1.5, and is copied below

$$(V^* + V_0^*)\left[M^*\frac{dV^*}{dt^*} + G(V^*)\right] + V^*P_0^* - t^* = 0 \tag{1.7.4}$$

with the initial condition $V^*(t^*=0) = 0$. For $M^* = 0$ (i.e., no microfluidic resistance), its solution V_{SOL}^* satisfies Eq. 1.6, i.e.

$$(V_{SOL}^* + V_0^*)\,G(V_{SOL}^*) + V_{SOL}^*P_0^* - t^* = 0 \tag{1.7.5}$$

It satisfies $V_{SOL}^*(t^*=0) = 0$ but not $\frac{dV_{SOL}^*}{dt^*}(t^*=0) = 0$. Therefore, the singular perturbation is used to solve Eq. 1.7.5 next. First, we write the solution in the form

$$V^* = V^*_{SOL} + M^*\bar{V}^*(\eta) \tag{1.7.6}$$

for small M^*, where $M^*\bar{V}^*$ is the correction term, $\bar{V}^*$ is a function of $\eta = \frac{t^*}{M^*}$. The derivative of Eq. 1.7.6 then becomes $\frac{dV^*}{dt^*} = \frac{dV^*_{SOL}}{dt^*} + \frac{d\bar{V}^*}{d\eta}$. Substitution of Eq. 1.7.6 and its derivative into Eq. 1.7.4 gives

$$(V^*_{SOL} + M^*\bar{V}^* + V^*_0)\left[M^*\frac{dV^*_{SOL}}{dt^*} + M^*\frac{d\bar{V}^*}{d\eta} + G(V^*_{SOL} + M^*\bar{V}^*)\right] + V^*_{SOL}P^*_0 + P^*_0M^*\bar{V}^* - t^* = 0 \tag{1.7.7}$$

For small M^*, the Taylor series expansion gives $G(V^*_{SOL} + M^*\bar{V}^*) = G(V^*_{SOL}) + G'(V^*_{SOL})M^*\bar{V}^*$. Subtraction of Eq. 1.7.4 from Eq. 1.7.7 yields

$$(V^*_{SOL} + V^*_0)\left[\frac{dV^*_{SOL}}{dt^*} + \frac{d\bar{V}^*}{d\eta} + G'(V^*_{SOL})\bar{V}^*\right] + G(V^*_{SOL})\bar{V}^* + P^*_0\bar{V}^* = 0 \tag{1.7.8}$$

where only the first order terms of M^* are kept. Note that $\bar{V}^*$ is a function of η, not t^*, and $t^* = \eta M^*$. Eq. 1.7.8 then becomes

$$[V^*_{SOL}(\eta M^*) + V^*_0]\frac{d\bar{V}^*}{d\eta} + \{[V^*_{SOL}(\eta M^*) + V^*_0]G'[V^*_{SOL}(\eta M^*)] + G[V^*_{SOL}(\eta M^*)] + P^*_0\}\bar{V}^* + [V^*_{SOL}(\eta M^*) + V^*_0]\left.\frac{dV^*_{SOL}}{dt^*}\right|_{t^*=\eta M^*} = 0 \tag{1.7.9}$$

For a finite η and very small M^*, ηM^* is approximately zero such that $V_{SOL}^*(\eta M^*) = V_{SOL}^*(0) = 0$, $G[V_{SOL}^*(\eta M^*)] = G[V_{SOL}^*(0)] = 0$, and $\left.\frac{dV_{SOL}^*}{dt^*}\right|_{t^*=\eta M^*} = \left.\frac{dV_{SOL}^*}{dt^*}\right|_{t^*=0} = \frac{1}{V_0^* G'(0)+P_0^*}$ from Eq. 1.7.5. Then, Eq 1.7.9 is simplified to

$$\frac{d\bar{V}^*}{d\eta} + \left[G'(0) + \frac{P_0^*}{V_0^*}\right]\bar{V}^* = -\frac{1}{V_0^* G'(0) + P_0^*} \tag{1.7.10}$$

Its solution is $\bar{V}^* = -\frac{1}{V_0^*\left[G'(0)+\frac{P_0^*}{V_0^*}\right]^2} + De^{-\left[G'(0)+\frac{P_0^*}{V_0^*}\right]\eta}$, where D is a constant determined from the initial condition $\left.\frac{dV^*}{dt^*}\right|_{t^*=0} = 0$, therefore $\left.\frac{d\bar{V}^*}{d\eta}\right|_{t^*=0} + \left.\frac{dV_{SOL}^*}{dt^*}\right|_{t^*=0} = 0$, as

$$D = \frac{1}{V_0^*\left[G'(0) + \frac{P_0^*}{V_0^*}\right]^2} \tag{1.7.11}$$

It is noted that $G'(0)=\frac{R_0^4}{Eh}f'(0)$, and $f'(0)$ is determined from the linear elastic plate theory for a circular plate subjected to uniform lateral pressure as $f'(0) = \frac{16Eh^3}{\pi R_0^6(1-\nu^2)}$ ($\nu = 0.5$ for incompressible material). These give the solution in Eq. 1.7.1 which satisfies the zero-flowrate initial condition. The flowrate expression is obtained from 1.7.1 by taking its derivative with respect to time as $\frac{dV^*}{dt^*}$.

Figures 1.2A and 1.2B show the results in Eq. 1.5 (numerical solution) and Eq. 1.7 (semi-analytical model with function $f(V)$ still determined from FEA) when M^* changes for the base line values $V_0^* = 0.79$, $P_0^* = 0.06$, and $\frac{h}{R_0} = \frac{1}{8}$ obtained from the experiments. For both volume V^* and flowrate $\frac{dV^*}{dt^*}$, the numerical solution and semi-analytical model agree very well for values of $M^* \sim 10^{-4}$ and $\sim 10^{-3}$, though the results deviate at $M^* \sim 10^{-2}$ because M^* is no longer small (assumption in Eq. 1.7). The volume V^* decreases as the microfluidic resistance M^* increases (Figure 1.2A). It also decreases as the initial volume V_0^* increases (Figure 1.2C) because, for small V_0^*, the PV term quickly overwhelms the initial volume term PV_0 resulting in a faster volume increase with time. On the contrary, for large V_0^*, the term PV_0 dominates for a substantial time, taking longer for the term PV to outperform it over time slowing down the volume increase. Similarly, the volume V^* decreases as the initial environmental P_0^* increases (Figure 1.2D) because, for small P_0^*, the change in pressure due to microfluidic channel $\frac{32\mu L\dot{V}}{a^4}$ and flexible membrane deformation $f(V)$ quickly overcomes the environmental pressure P_0 for a faster volume increase; for large P_0 (e.g., drug delivery at different organ/tissues), the pressure increments due to $\frac{32\mu L\dot{V}}{a^4}$ and $f(V)$ are insignificant as compared to the initial environmental pressure slowing down the drug volume delivery.

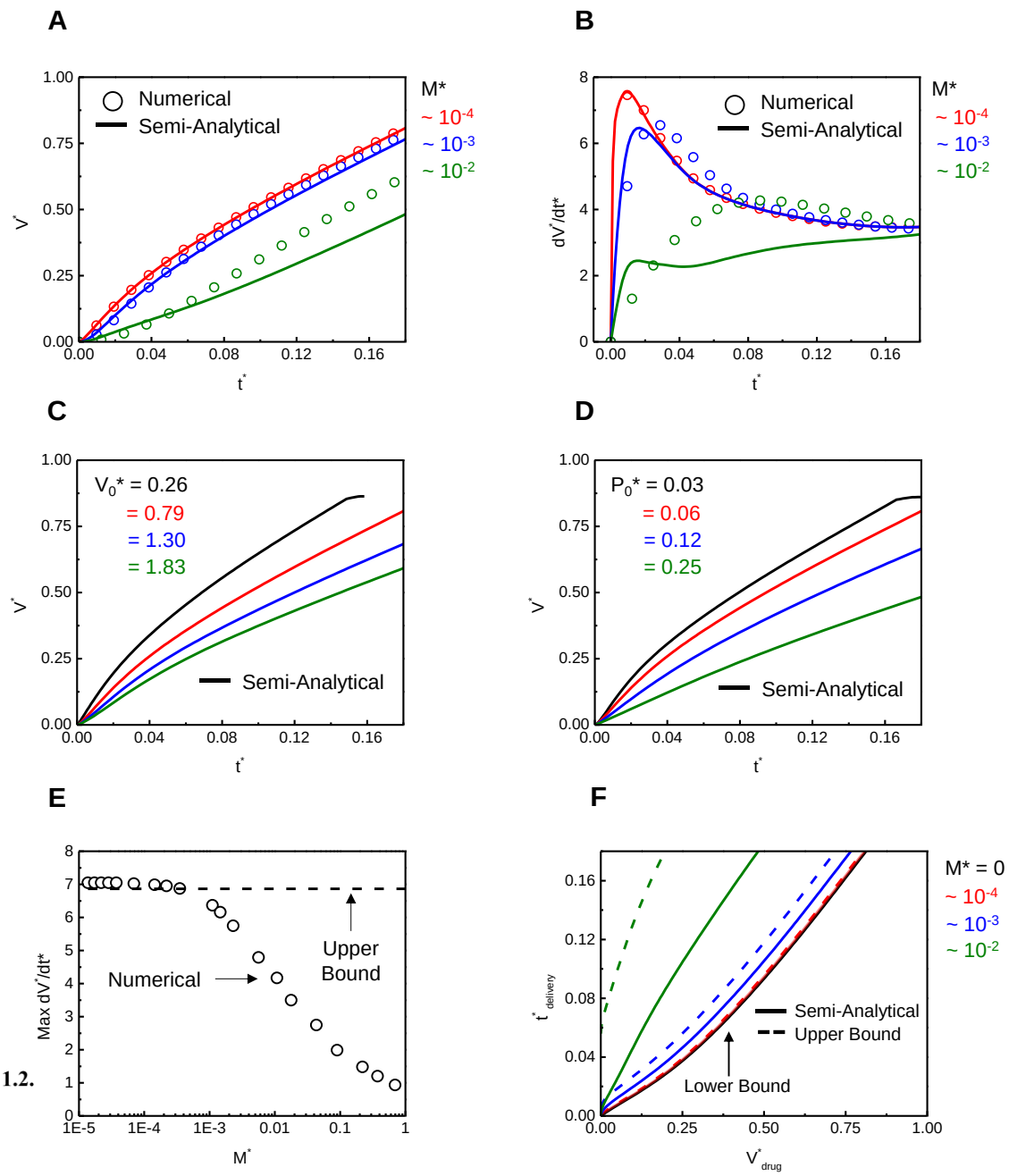

Figure 1.2. Drug delivery models and scaling results. (A) Numerical and semi-analytical model results for normalized drug volume delivery and (B) normalized flow rate over normalized time for different M^*. Normalized drug volume delivery for different (C) initial volume V_0^* and (D) initial environmental pressure P_0^*. (E) Maximum normalized flowrate and the upper bound. (F) Critical normalized time to deliver normalized drug volume for different M^*, the lower bound corresponds to $M^* = 0$.

1.2.2. Derivation of the Flowrate and Critical Delivery Time

The non-dimensional maximum flowrate $\frac{dV^*}{dt^*}$, which is the peak value in Figure 1.2B, is important in drug delivery. Figure 1.2E reveals that the maximum flowrate $\frac{dV^*}{dt^*}$ remains relatively constant for small microfluidic resistance M^*<10^{-4} and monotonically decreases as M^* increases from 10^{-4} to 1 therefore providing a parameter to control the maximum flow rate. In addition, the upper bound maximum (dimensional) flowrate is derived analytically as

$$\dot{V}_{max} = \frac{3iRT}{4F\left[\frac{16Eh^3V_0}{\pi R_0^6(1-\nu^2)} + P_0\right]} \tag{1.8}$$

which is linearly proportional to the current i and temperature T and decreases as the initial environmental pressure P_0 or the product $\frac{Eh^3V_0}{R_0^6(1-\nu^2)}$ of initial volume and bending stiffness of the flexible membrane increases, where ν is the Poisson's ratio of the membrane. This upper bound solution is independent of the material constitutive model, accurate for small M^*, and overestimates as M^* increases. Figure 1.2F shows the critical nondimensional time $t^*_{delivery}$ required to deliver a nondimensional volume V^*_{drug} of drug as M^* increases. For $M^* = 0$, the solution simplifies to Eq. 1.6, which becomes the lower bound (black line) as there is no microfluidic resistance. As M^* increases, the time to deliver the drug also increases, and its upper bound estimate is given analytically by

$$t^*_{delivery} = \left\{\left[V^* + \frac{M^*}{V_0^*\left(\frac{64h^2}{3\pi R_0^2} + \frac{P_0^*}{V_0^*}\right)^2}\right] + V_0^*\right\}\frac{R_0}{Eh} f\left\{\left[V^* + \frac{M^*}{V_0^*\left(\frac{64h^2}{3\pi R_0^2} + \frac{P_0^*}{V_0^*}\right)^2}\right]R_0^3\right\} + P_0^*\left[V^* + \frac{M^*}{V_0^*\left(\frac{64h^2}{3\pi R_0^2} + \frac{P_0^*}{V_0^*}\right)^2}\right] \quad (1.9)$$

where the term $f(V)$ depends on the material's constitutive model. The semi-analytical solution in Eq. 1.7 is clearly between the lower- and upper- bound estimate (Figure 1.2F) and the $f(V)$ in Eq. 1.9 was determined from FEA using the Marlow hyper elastic constitutive model based on the stress-strain relationship of the flexible membrane discussed later in this chapter.

In animal behavioral studies involving drug delivery, the precise control of flowrate is critical to avoid tissue damage in the surrounding areas caused by high flowrates and this can be achieved by adjusting the current in the experiment [15,16]. Figure 1.3A shows that the upper bound and the numerical results of the maximum flowrate, which agree very well with the experiments in [15] for small current (< 0.3 mA), and they deviate at larger currents (> 0.3 mA) due to increasing bubble formation near the electrodes reducing the contact area between the electrodes and electrolyte solution. The top x-axis of Figure 3A shows the equivalent M^* for the effective current values. In the delivery presented in Figure 1.3B for [16] where i = 0.3 mA, the flowrate rapidly increases and reaches the maximum flowrate~1.5 μL/min within a few seconds. This is also confirmed by the numerical results as well as the semi-analytical model, which agree well with the experiments in [16]. The upper bound solution is also shown in Figure 1.3B, which

overestimates the maximum flowrate by~5%. The parameters used in the analytical and numerical models for Figure 1.3 are listed in Table 1.

Table 1.1. Properties and representative values of parameters used in the numerical and analytical models.

Parameter	Value	Units
P_0	101.3	kPa
R_0	5	mm
E_{SBS}	15	MPa
E_{SIS}	6	MPa
h	150	μm
F	96485	C/mol
T	300	K
R	8.3144	J/mol K
i	0.5	mA
a, b	10-200	μm
L	10	mm
μ	0.89	mPa-s

The delivery requirements can vary between slow or instant stimulation depending on the type of biomedical experiment and target locations inside the animal body. Programmable control over the flowrate and total delivery time are critical in many neuroscience experiments to avoid

any damage to the surrounding locations and ensure that the stimulation was completed within a required timeframe. Depending on the type of stimulation, the system can be designed using the three non-dimensional parameters proposed in the analytical model for programmable operation of flowrates/time scales range prior to fabrication of the physical device. During the delivery, the non-dimensional parameters serve as the programmable controls to adjust flowrates and delivery timescale by adjusting parameters like the effective current depending on the experimental requirements (e.g., low flowrates preferred in the brain to avoid damage, and high flowrates to quickly suppress/reverse side effects).

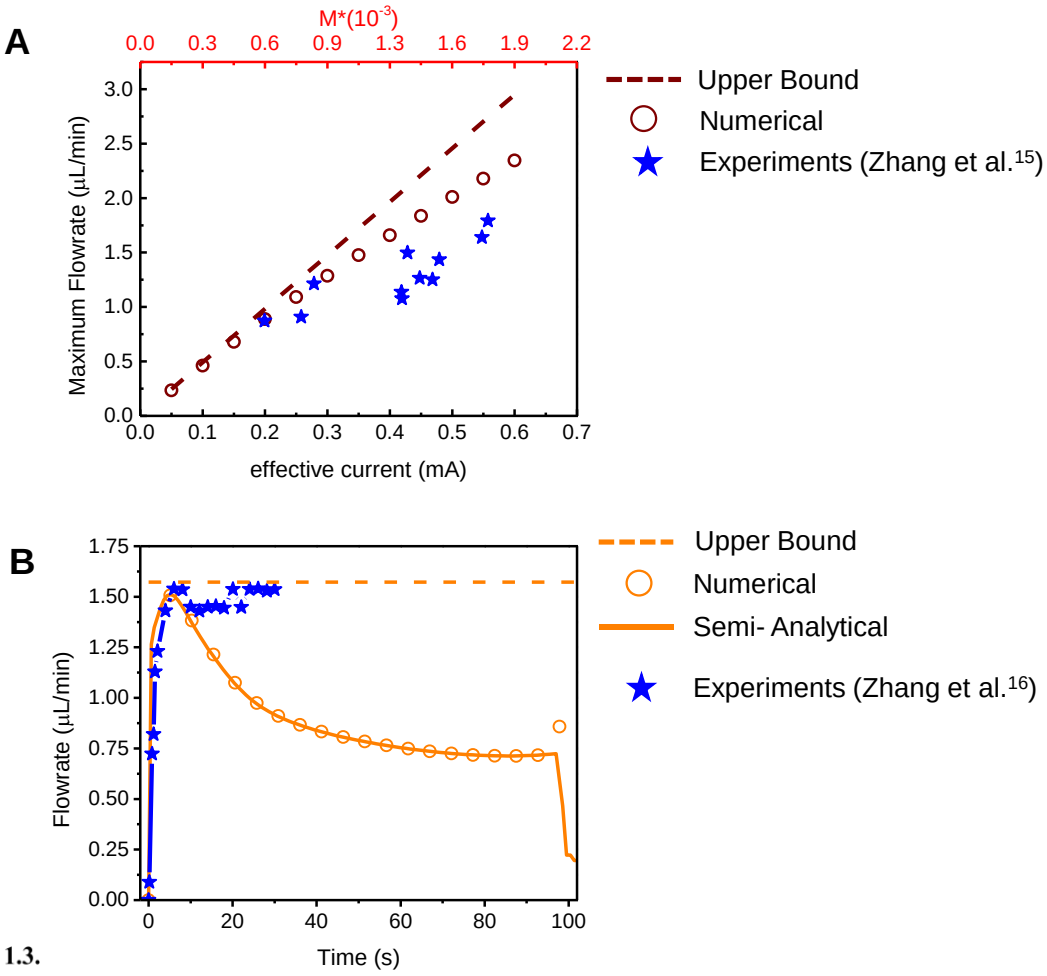

Figure 1.3. Drug delivery experiments and modeling. (A) Maximum flowrate as a function of effective current for the upper bound solution (wine dashed line), numerical (wine circles) and experiments data in [15] (blue stars) for a system with microchannel cross-section 30 µm × 30 µm. (B) Flowrate as a function of time models for the upper bound solution (orange dashed line), numerical (orange circles), semi- analytical model (orange continuous line) and experiments data in [16] (blue stars) for a system with microchannel cross-section 60 µm × 60 µm..

1.3.

Mechanics of the Flexible Membrane

The semi-analytical model presented in Eq. 1.7 requires FEA to determine the function $f(V)$ related to the stiffness of the flexible membrane. Figure 1.6A shows the deformed profile of the flexible membrane obtained by FEA. The profile shows zero slope at the clamped edges under

small pressure suggesting the bending-dominated deformation. For large pressure, however, this zero slope becomes invisible, suggesting the stretching-dominated deformation. The analytical solutions of $f(V)$ are obtained in the following for different constitutive models of polymers, including linear elastic, Mooney Rivlin [37], and Marlow [38] hyperelastic models, where the last one can fit any stress-strain curve of polymers [39].

Bending solution (i.e., bending-dominated deformation): Under small pressure the deformation is linear elastic (and all hyperelastic models degenerate to linear elasticity). The flexible membrane can be modeled as a clamped, elastic thin plate with bending stiffness $\frac{Eh^3}{12(1-v^2)}$, [40]. The volume *V* of the deformed membrane is linearly proportional to the pressure *p*, and this *p*~*V* relation [40] gives

$$f(V) = \frac{16Eh^3}{\pi R_0^6(1-v^2)}V \tag{1.10}$$

1.3.1. Linear Elastic Membrane Solution

Linear elastic membrane solution (i.e., stretching-dominated deformation): Under large pressure the deformation is stretching-dominated, i.e., the bending deformation becomes negligible. For a linear elastic polymer, the equi-biaxial tensile stiffness $\frac{Eh}{1-v}$ replaces the bending stiffness $\frac{Eh^3}{12(1-v^2)}$ in the analysis, which yields the following nonlinear *p*~*V* relation (due to large deformation)

$$f(V) = \frac{64Eh}{3\pi^3 R_0^{10}(1-v)}V^3 \tag{1.11.1}$$

For a thin circular membrane with thickness h, Young modulus E and Poisson ratio ν under stretching-dominated deformation, the in-plane stress state is approximately equi-biaxial $\sigma_{rr} \approx \sigma_{\theta\theta}$ (denoted by σ) and out-of-plane stress $\sigma_{zz} = 0$. It is related to the strains $\varepsilon_{rr} \approx \varepsilon_{\theta\theta}$ (denoted by ε) via the linear elastic model

$$\sigma = \sigma_{rr} \approx \sigma_{\theta\theta} = \frac{E}{1-\nu}\varepsilon \tag{1.11.2}$$

The deformation of a flat flexible membrane with radius R_0 to a spherical cap of radius r is shown in Figure 1.4, and the radii are related by $R_0 = r\sin\phi$, where the angle ϕ is shown in Figure 1.4. The strain ε in the spherical cap is defined from $R_0 = \frac{r\phi}{1+\varepsilon}$, which gives the $\varepsilon - \phi$ relation as

$$\frac{\sin\phi}{\phi} = \frac{1}{1+\varepsilon} \tag{1.11.3}$$

The Taylor series expansions of ϕ and ε in the above equation are $1 - \frac{1}{6}\phi^2 + \cdots \approx 1 - \varepsilon + \frac{1}{2}\varepsilon^2 + \cdots$, which gives a first-order approximation $\phi \approx \sqrt{6\varepsilon}$. The stress is then obtained from Eq. 1.11.2 as $\sigma = \frac{E}{1-\nu}\frac{\phi^2}{6}$. The force equilibrium requires the pressure difference $P - P_0$ on two sides of the membrane be balanced by the stress σ at the clamped edge as

$$\pi R_0^2(P - P_0) = 2\pi\sigma h R_0 \sin\phi \tag{1.11.4}$$

Using $\sin\phi \approx \phi$ for small deformation (as for linear elasticity), and substituting $\sigma = \frac{E}{1-\nu}\frac{\phi^2}{6}$ into Eq. 1.11.4, give $P - P_0$ in terms of ϕ

$$P - P_0 = \frac{Eh}{R_0(1-\nu)}\frac{\phi^3}{3} \tag{1.11.5}$$

The volume of the spherical cap is $V = \frac{1}{6}\pi H(3R_0^2 + H^2)$, where the height H is $H = r - r\cos\phi = (1-\cos\phi)\frac{R_0}{\sin\phi}$. Using $\sin\phi \approx \phi$, the volume is found as

$$V = \frac{\pi}{4}R_0^3\phi \tag{1.11.6}$$

Elimination of ϕ from Eq. 1.11.5 and Eq. 1.11.6 yields the pressure-volume relation in Eq. 1.11.1 for a linear elastic material model. Figure 1.6B shows that, without any parameter fitting, the bending and linear elastic membrane solutions in the two equations above agree well with the FEA results at small and large deformation, respectively.

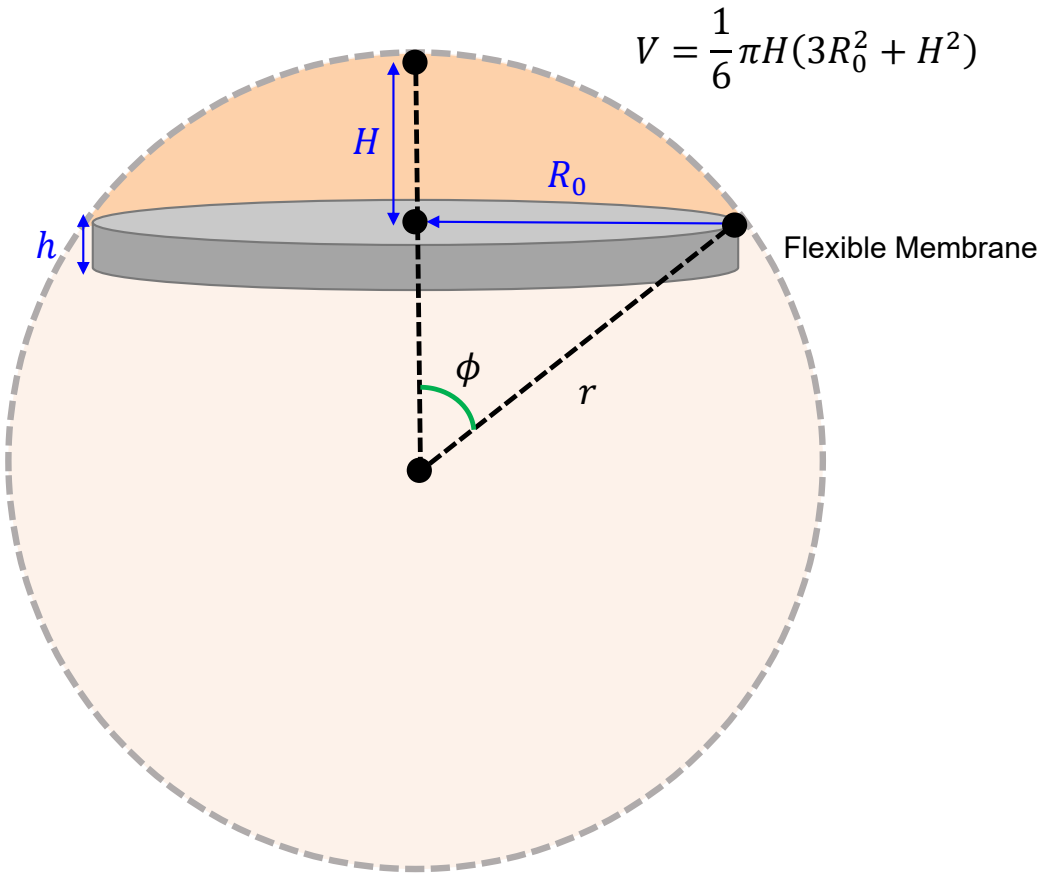

Figure 1.4.

Flexible membrane deformation based on the volume of the spherical cap. R_0 = Flexible membrane radius, h = Flexible membrane thickness, r = Radius of the sphere, ϕ = Polar angle between the center of the sphere to the apex of the spherical cap and the edge of the flexible membrane, H = Height of the spherical cap, V = Volume of the spherical cap.

1.3.2. Mooney Rivlin Membrane Solution

Mooney Rivlin membrane solution (i.e., stretching-dominated deformation): Under large pressure the Mooney Rivlin hyperelastic model might be more suitable for a linear elastic one. For an incompressible Mooney Rivlin hyperelastic material, the approximately equi-biaxial stress in the membrane is given by

$$\sigma = \sigma_{rr} \approx \sigma_{\theta\theta} = 2C_1\left(\lambda^2 - \frac{1}{\lambda^4}\right) - 2C_2\left(\frac{1}{\lambda^2} - \lambda^4\right) \tag{1.12.1}$$

where the stretch λ is related the strain by $\lambda = 1 + \varepsilon = \frac{\phi}{\sin\phi}$ from Eq. 1.11.3, and the material constants C_1 and C_2 are related to the Young modulus (and Poisson ratio) by $C_1 = \frac{E}{5(1+\nu)} = \frac{2E}{15}$ and $C_2 = \frac{E}{20(1+\nu)} = \frac{E}{30}$. The force equilibrium Eq. 1.11.4 now becomes

$$\pi R_0^2(P - P_0) = 2\pi\sigma h' R_0 \sin\phi \tag{1.12.2}$$

where h' is the membrane thickness in the deformed configuration, and is given by $h' = \frac{h}{\lambda^2}$ due to material incompressibility. The following *p*~*V* relation in the form of parametric equations is obtained for a Mooney Rivlin Material

$$f(V) = P - P_0 = \frac{4Eh}{3R_0}\frac{\sin^3\phi}{\phi^2}\left\{\frac{2}{5}\left[\left(\frac{\phi}{\sin\phi}\right)^2 - \left(\frac{\sin\phi}{\phi}\right)^4\right] - \frac{1}{10}\left[\left(\frac{\sin\phi}{\phi}\right)^2 - \left(\frac{\phi}{\sin\phi}\right)^4\right]\right\}, \tag{1.12.3}$$

$$V = \frac{\pi R_0^3}{6}\frac{1-\cos\phi}{\sin\phi}\left[3 + \left(\frac{1-\cos\phi}{\sin\phi}\right)^2\right] \tag{1.13}$$

where the variable ϕ in the parametric equations above is defined as the polar angle that tracks the deformation of the flexible membrane from flat to the shape of a spherical cap. Figure 1.6C shows

that the membrane solution above agrees very well with the FEA results without any parameter fitting, except for very small volume where the bending solution in Eq. 1.10 is more accurate.

1.3.3. Marlow Membrane Solution

Marlow membrane solution (i.e., stretching-dominated deformation): The Marlow hyperelastic model can fit any uniaxial stress-strain curve to the desired accuracy [39], including that of the SBS (Polystyrene-Block-Polybutadiene-Block-Polystyrene-SBS) flexible membrane used in implantable microsystems and shown in Figure 1.5 due to its soft modulus, and water/oxygen/hydrogen permeability properties [15,16]. For the Marlow hyperelastic model, the volume is still given by Eq. 1.13, but the pressure becomes

$$f(V) = \frac{2h}{R_0}\frac{\sin^3\phi}{\phi^2}\sigma_{11}(\phi) \tag{1.14.1}$$

where the function σ_{11} is a principal stress, and it depends on the uniaxial stress-strain curve of the polymer. The derivation of the principal stress for the Marlow hyperelastic model is shown as follows. The Marlow strain energy potential for an incompressible solid is given by

$$W = W(\bar{I}_1) \tag{1.14.2}$$

where the first invariant $\bar{I}_1 = \lambda_1^2 + \lambda_2^2 + \lambda_3^2$, and λ_1, λ_2 and λ_3 are principal stretches that satisfy $\lambda_1\lambda_2\lambda_3 = 1$ for an incompressible solid. The true stress (or Cauchy stress) is given by

$$\boldsymbol{\sigma} = 2\frac{dW}{d\bar{I}_1}\boldsymbol{B} + \boldsymbol{p} \tag{1.14.3}$$

where $\boldsymbol{p}$ is the hydrostatic pressure, and the Cauchy-Green deformation tensor $\boldsymbol{B}$ is given by

$$\boldsymbol{B} = \begin{pmatrix} \lambda_1^2 & 0 & 0 \\ 0 & \lambda_2^2 & 0 \\ 0 & 0 & \lambda_3^2 \end{pmatrix} \tag{1.14.4}$$

in the principal stretch directions. The principal stresses can be written in terms of the principal stretches as

$$\sigma_{11} - \sigma_{33} = 2\frac{dW}{d\bar{I}_1}(\lambda_1^2 - \lambda_3^2) \tag{1.14.5}$$

$$\sigma_{22} - \sigma_{33} = 2\frac{dW}{d\bar{I}_1}(\lambda_2^2 - \lambda_3^2) \tag{1.14.6}$$

It is important to point out that $\frac{dW}{d\bar{I}_1}$ is usually determined from the uniaxial stress-strain curve in experiments. These uniaxial tension data, as shown in Figure 1.5, are usually given via the relation between the nominal (engineering) stress σ_n and engineering strain ε, i.e., $\sigma_n(\varepsilon)$. For uniaxial tension, $\sigma_{22} = \sigma_{33} = 0$, the nominal stress σ_n is related to the true stress σ_{11} by $\sigma_n = \frac{\sigma_{11}}{\lambda}$; where the principal stretches are $\lambda_1 = \lambda$ and $\lambda_2 = \lambda_3 = \frac{1}{\sqrt{\lambda}}$ due to incompressibility. The first invariant then becomes

$$\bar{I}_1 = \lambda^2 + \frac{2}{\lambda} = (1+\varepsilon)^2 + \frac{2}{1+\varepsilon} \tag{1.14.7}$$

Then Eq. 1.14.5 becomes

$$\lambda\sigma_n(\varepsilon) = 2\frac{dW}{d\bar{I}_1}\left(\lambda^2 - \frac{1}{\lambda}\right) \tag{1.14.8}$$

where $\frac{dW}{d\bar{I}_1}$ is a function of the first invariant $\bar{I}_1$. The above equation can be rearranged to express $\frac{dW}{d\bar{I}_1}$ in terms of the strain ε as

$$\frac{dW}{d\bar{I}_1} = \frac{(1+\varepsilon)^2}{2[(1+\varepsilon)^3 - 1]}\sigma_n(\varepsilon) \tag{1.14.9}$$

Eq. 1.14.8 and Eq. 1.14.9 become the parametric equations for $\frac{dW}{d\bar{I}_1}$ as a function of the first invariant $\bar{I}_1$. For the flexible membrane under pressure, it experiences equi-biaxial stretching (not uniaxial tension) such $\frac{dW}{d\bar{I}_1}$ for equi-biaxial stretching must be determined. The principal stress $\sigma_{33} = 0$ and the principal stretches now become $\lambda_1 = \lambda_2 = \lambda$ and $\lambda_3 = \frac{1}{\lambda^2}$. The first invariant then becomes $\bar{I}_1 = 2\lambda^2 + \frac{1}{\lambda^4}$ and the Cauchy stresses become

$$\sigma_{11} = \sigma_{22} = 2\frac{dW}{d\bar{I}_1}\Big|_{\bar{I}_1 = 2\lambda^2 + \frac{1}{\lambda^4}} \left(\lambda^2 - \frac{1}{\lambda^4}\right) \tag{1.14.10}$$

where $\frac{dW}{d\bar{I}_1}$ is a function of $\bar{I}_1 = 2\lambda^2 + \frac{1}{\lambda^4}$. For $f(V)$ in Eq. 1.14.1, we need to determine σ_{11} in terms of ϕ. The first invariant $\bar{I}_1 = 2\lambda^2 + \frac{1}{\lambda^4}$ is written in terms of ϕ as

$$\bar{I}_1(\phi) = 2\left(\frac{\phi}{\sin\phi}\right)^2 + \left(\frac{\sin\phi}{\phi}\right)^4 \tag{1.14.11}$$

It is important to note that for uniaxial tension ($\bar{I}_1 = \lambda^2 + \frac{2}{\lambda}$) and equi-biaxial tension ($\bar{I}_1 = 2\lambda^2 + \frac{1}{\lambda^4}$) only their first invariants $\bar{I}_1$ are equivalent. Therefore, Step 1: We can set the equibiaxial tension $\bar{I}_1$ (in Eq. 1.14.11, given in terms of ϕ) equal to the uniaxial tension $\bar{I}_1$ (in Eq. 1.14.7, given in terms of ε), i.e.,

$$2\left(\frac{\phi}{\sin\phi}\right)^2 + \left(\frac{\sin\phi}{\phi}\right)^4 = \bar{I}_1(\phi) = \bar{I}_1(\varepsilon) = (1+\varepsilon)^2 + \frac{2}{1+\varepsilon} \tag{1.14.12}$$

which is solved numerically to give ε in terms of ϕ. Step 2: For this ε and experimental stress-strain curve $\sigma_n(\varepsilon)$ in Figure 1.5, determine the value of $\frac{dW}{d\bar{I}_1}$ from Eq. 1.14.12.

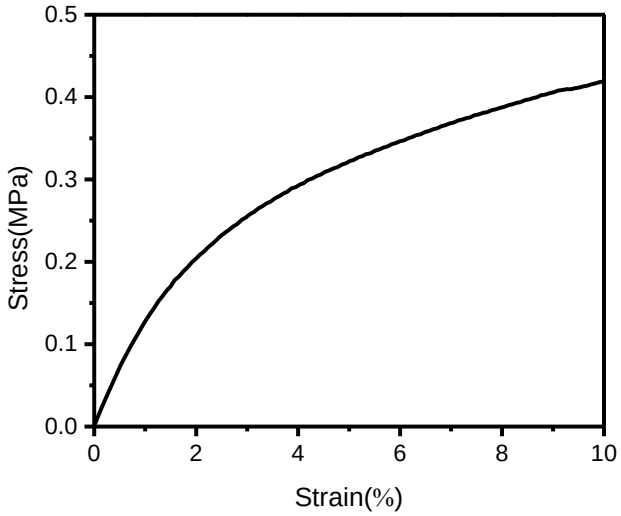

Figure 1.5. Nominal stress-strain behavior of Polystyrene-Block-Polybutadiene-Block-Polystyrene (SBS) (E ~ 13 MPa) obtained from uniaxial test

Then, Step 3: Substitute this $\frac{dW}{d\bar{I}_1}$ into Eq. 1.14.10 to give

$$\sigma_{11}(\phi) = 2\frac{dW}{d\bar{I}_1}\left[\left(\frac{\phi}{\sin\phi}\right)^2 - \left(\frac{\sin\phi}{\phi}\right)^4\right] \tag{1.14.13}$$

The force equilibrium equation then gives the pressure in Eq. 1.14.1, in which $\sigma_{11}(\phi)$ is obtained from Eq. 1.14.13 and the parametric equation for the volume of the spherical cap in Eq. 1.13 still holds. Figure 1.6D shows that, for SBS, the membrane solution in Eqs. 1.13 and 1.14.1 agrees reasonably well with the FEA results to predict the biaxial deformation of the flexible membrane.

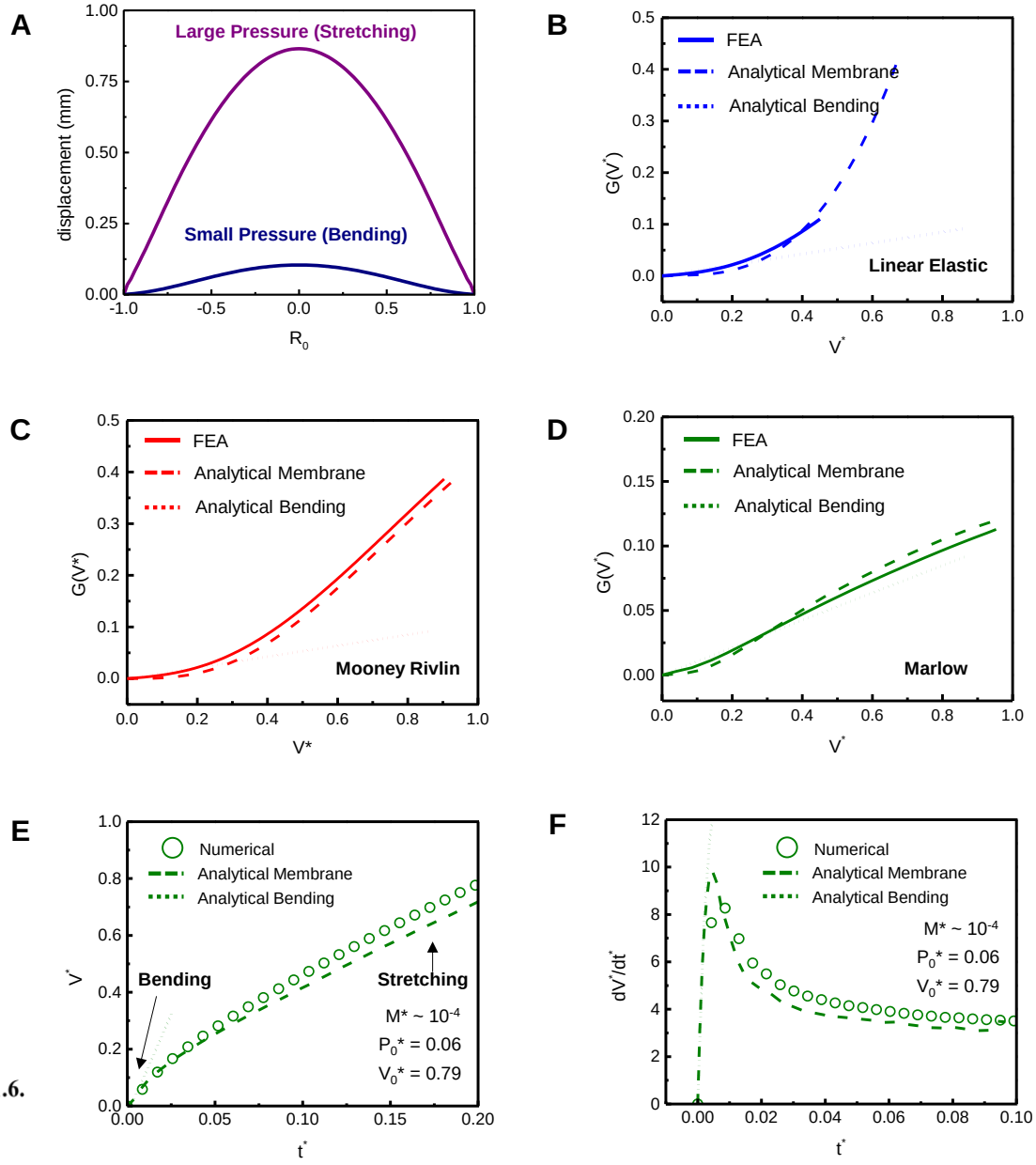

Figure 1.6.

Flexible membrane deformation mechanics. (A) FEA results of membrane displacement (bending dominated and stretching dominated) as a function of the membrane radius. (B) Non-dimensional function $G(V^*)$ as a function of V^* between FEA (solid line), membrane solution (dashed line), and bending solution (dot line) for a linear elastic material, (C) Mooney Rivlin hyper elastic Material, and (D) Marlow hyper elastic Material. (E) Non-dimensional volume and (F) Non-dimensional flowrate as a function of non-dimensional time for the Marlow hyper elastic material in (D) with different $G(V^*)$ solutions for the baseline non-dimensional parameters.

The analytic formula of $f(V)$ given above in Eq. 1.13, combined with Eq. 1.7 or Eq. 1.9 for drug delivery time (Eq. 1.8 for the upper bound of maximum flowrate), are very useful to estimate the drug delivery time and the maximum flowrate analytically (i.e., it requires neither FEA for $f(V)$ nor numerical solution of ODE). Figure 1.6E shows the analytical results of the non-dimensional volume delivery over non-dimensional time for SBS used in experiments [15,16] and in Figure 1.6D. The bending solution in Eq. 1.10 and the parametric membrane solution in Eq. 1.12 and Eq. 1.13 are used as input for $f(V)$ in the analytical model in Eq. 1.7.1, and they agree very well with the full numerical results (FEA+ODE) for small and large volumes, respectively. This provides a simple but accurate way to estimate the drug delivery time. Similarly, Figure 1.6F shows the flowrate over time from the membrane solution based on the Marlow model agrees reasonably well with the full numerical results, therefore its analytic expression can be used to estimate the flowrate in drug delivery. The analytical model (with the analytic expression of $f(V)$ without FEA) shows very good agreement with the upper bound solution for the maximum flowrate for small $M^*$and is clearly between the lower- and upper- bound estimate for the critical delivery time. It is important to note that the agreement between the numerical and membrane solution is dependent on the microfluidic resistance M^*, and this agreement becomes worse for large M^*.

ABAQUS, a commercial FEA software, was used to model the flexible membrane deformation and calculate the function $f(V)$ which captures both bending and stretching effects in the flexible membrane. The circular flexible membrane, fixed at the circumference, is subjected to a pressure P at the bottom surface that deforms the membrane into a spherical cap shaped determined by the stiff drug reservoir shown in Figure 1.1. The contact between the flexible

membrane and the drug reservoir is considered in the simulation. The flexible membrane (Polystyrene-Block-Polybutadiene-Block-Polystyrene-SBS) and drug reservoir (Cyclic Olefin Polymer - COP) were modeled by hexahedron elements (C3D8R). The number of elements in the model was ~1×10^5, and the minimal element size was 1/6 of the thickness of the flexible membrane (150 μm). Mesh convergence of the simulation was ensured for all cases. For the linear elastic model, the membrane elastic modulus (E) and Poisson's ratio (ν) of are E_{SBS}=13 MPa and v_{SBS} =0.49 for copper; in the Mooney Rivlin hyper elastic model the membrane coefficients are C_{10} = 1.744 MPa, C_{01} = 0.4362 MPa, and D_1 = 0.00923 MPa^{-1}; in the Marlow hyper elastic model uniaxial test data was the input source to define the nominal stress-strain curve of the SBS flexible membrane. In all cases, the elastic modulus (E) and Poisson's ratio (v) of COP are E_{COP}=2.5 GPa and v_{COP} =0.37

1.4.

Bending Dominated Deformation

For small pressure, the flexible membrane is linear elastic, and can be modeled as a clamped thin plate with bending stiffness $D = \frac{Eh^3}{12(1-v^2)}$ [40] where E is the Young's modulus, v is the Poisson ratio ($v = 0.5$ for incompressible solid) and the deflection w at any point r along the radius is given by

$$w(r) = \frac{R_0^4}{64D}\left(P - P_{drug}\right)\left(1 - \frac{r^2}{R_0^2}\right)^2 \tag{1.15}$$

This gives the maximum deflection of the flexible membrane $H = \frac{R_0^4}{64D}\left(P - P_{drug}\right)$ when $r = 0$, and the volume V under the deflection of the membrane

$$V = \int_0^{R_0} 2\pi w r dr = \frac{\pi R_0^6}{192D}\left(P - P_{drug}\right) \tag{1.16}$$

or equivalently

$$f(V) = \frac{16Eh^3}{\pi R_0^6(1-v^2)}V \tag{1.17}$$

It gives

$$f(V) + Vf'(V) = \frac{32Eh^3}{\pi R_0^6(1-v^2)}V \tag{1.18}$$

which is used to calculate the volume temporal profile Then the non-dimensional function for the pressure becomes $G(V^*) = \frac{16h^2}{\pi R_0^2(1-v^2)}V^*$, which depends on the ratio $\frac{h}{R_0}$. Figure 1.7 shows this bending-dominated $G(V^*)$ and that obtained from finite element analysis agree well for small deformation (i.e., $H \ll h$) for both SBS (Figure 1.5A) and SIS (Figure 1.5B) copolymers, and $h = 0.15\ mm$ and $R_0 = 5\ mm$. As the pressure-volume increases, the bending effect in the membrane becomes negligible, leading to the discrepancy between the FEA and bending-dominated $G(V^*)$.

Stretching Dominated Deformation

For large pressure, the deformation is stretching dominated, and the bending effect becomes negligible. Equilibrium of forces requires the pressure difference $P - P_{drug}$ on two sides of the membrane be balanced by the stress traction at the clamped edge as

1.5.

$$\pi R_0^2 \left(P - P_{drug}\right) = 2\pi\sigma h' R_0 \sin\phi \tag{1.19}$$

where σ is the true stress at the edge of the membrane under equibiaxial stretching, $h' = \frac{h}{\lambda_{equi}^2}$ gives the membrane thickness in the deformed configuration due to material incompressibility, and the angle ϕ tracks the deformation of the membrane from flat into the shape of a spherical cap shown in Figure 1.6A. The stretch λ_{equi} is related to the polar angle ϕ as

$$\lambda_{equi} = \frac{\phi}{\sin\phi} \tag{1.20}$$

Eqs. 1.19 and 1.20 yield an analytic but parametric equation for the pressure as

$$f(V) = \frac{2h}{R_0}\frac{\sin^3\phi}{\phi^2}\sigma(\phi) \tag{1.21}$$

where the equibiaxial stress at the edge of the membrane, $\sigma(\phi)$, depends on not only the angle ϕ but also the Young's modulus and other (hyper)elastic properties of the membrane. The volume of the spherical cap in Figure 1.1C is given by

$$V = \frac{1}{6}\pi H(3R_0^2 + H^2) \tag{1.22}$$

where the height H is related to ϕ as

$$H = (1 - \cos\phi)\frac{R_0}{\sin\phi} \tag{1.23}$$

Substituting Eq. 1.23 into Eq 1.22 a parametric equation for the volume is obtained as

$$V = \frac{\pi R_0^3}{6}\frac{1 - \cos\phi}{\sin\phi}\left[3 + \left(\frac{1 - \cos\phi}{\sin\phi}\right)^2\right] \tag{1.24}$$

Together, Eq. 1.21 and Eq. 1.24 are the analytic but parametric equations for the function $f(V)$. They give, using $f'(V) = \frac{df(V)}{d\phi}\left(\frac{dV}{d\phi}\right)^{-1}$, the following expression

$$f(V) + Vf'(V) \tag{1.25}$$

$$= \frac{2h}{3R_0}\frac{\sin^3\phi}{\phi^2}\left\{\sin\phi(2+\cos\phi)\left[\sigma'_{11}(\phi) - 2\frac{\sigma_{11}(\phi)}{\phi}\right]\right.$$

$$\left. + 3(1+\cos\phi)^2\sigma_{11}(\phi)\right\}$$

needed in to calculate the drug delivery time. Figure 1.7 shows this stretching-dominated $G(V^*)$ and that obtained from FEA agree well for large deformation (i.e., $H \gg h$) for both SBS (Figure 1.7A) and SIS (Figure 1.7B) copolymers.

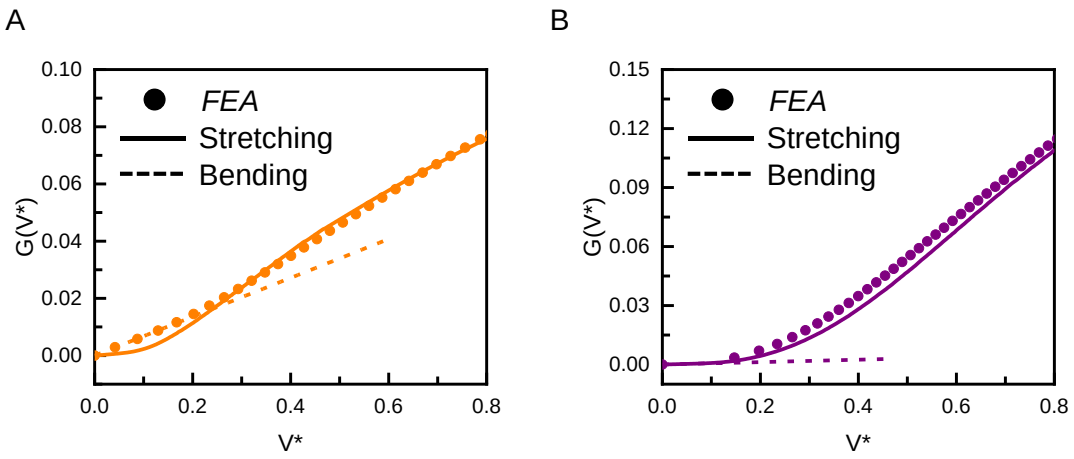

Figure 1.7: Function $G(V^*)$ for the (A) SBS and (B) SIS copolymers obtained from FEA (circles), and analytical solutions for bending-dominated (dashed lines) and stretching-dominated deformation (solid line).

1.6. Drug Delivery Time for Bending Dominated Deformation

Bending dominated deformation requires that the maximum deflection be much smaller than the membrane thickness, i.e. $H \ll h$, which, together with Eq. 1.10, requires the drug volume to satisfy

$$V \ll \frac{\pi h R_0^2}{3} \tag{1.26}$$

The drug delivery time the becomes

$$t = \frac{4F}{3RTi}\left(\frac{64}{3\pi}\frac{Eh^3}{R_0^6}V^2 + VP_0\right) + \frac{32\mu L}{a^4}\frac{V}{\frac{128}{3\pi}\frac{Eh^3}{R_0^6}V + P_0} \tag{1.27}$$

for $V \ll \frac{\pi h R_0^2}{3}$

Drug Delivery Time for Stretching Dominated Deformation

Stretching dominated deformation requires that the maximum deflection be much larger than the membrane thickness, i.e. $H \gg h$, which, together with Eq. 1.21, requires the drug volume to satisfy

1.7.

$$V \gg \frac{\pi h}{6}(3R_0^2 + h^2) \tag{1.28}$$

The drug delivery time becomes

$$t = \frac{4F}{3RTi}[Vf(V) + V(\phi)P_0] + \frac{32\mu L}{a^4}\frac{V(\phi)}{\frac{(1+\cos\phi)^2}{\pi R_0^3}\frac{d[Vf(V)]}{d\phi} + P_0} \tag{1.29}$$

for $V \gg \frac{\pi h}{6}(3R_0^2 + h^2)$, where $V(\phi)$ is given in Eq. 1.24. And with Eq. 1.29 give the parametric equations of the drug delivery time versus the drug volume for stretching dominated deformation.

Drug Delivery Time in General

For drug volume between the two cases discussed above, i.e.

1.8.

$$\sim\frac{\pi h R_0^2}{3} \ll V \ll \sim\frac{\pi h}{6}(3R_0^2 + h^2) \tag{1.30}$$

deformation is neither bending- nor stretching-dominated such that the function $f(V)$ is obtained numerically by FEA. For V in Eq. 1.30, then Eq. 1.7 is evaluated numerically to give the drug delivery time in terms of the drug volume.

1.9. Order of Erro in the Analytical Solution

The magnitude of M^* at which the analytical and numerical solutions agree well can be determined analytically. The error $O(M^{*2})$ is on the order of $\frac{M^{*2}}{P_0^{*3}}V^*$. The leading term $V^*[G(V^*) + P_0^*]$ is on the order of $P_0^*V^*$ as $G(V^*)\sim V^* \ll P_0^*$ at small V^*. The analytical solution becomes accurate (i.e., close to the numerical solution of Eq. 1.7) when the error $\frac{M^{*2}}{P_0^{*3}}V^* \ll P_0^*V^*$, which yields the following condition

$$M^* \ll {P_0^*}^2 \tag{1.31}$$

Only when the above condition is met the analytical solution in Eq. 1.29 gives accurately the time of drug delivery. This explains the results in Figure 1.8, which gives ${P_0^*}^2 = 0.0506$ (for ${P_0}^* = 0.225$) such that "small" microfluidic resistance $M^* = 0.0170$ satisfies $M^* \ll {P_0^*}^2$ in Eq.

31, and "large" microfluidic resistance $M^* = 0.100$ does not, yielding good and not-so-good agreements, respectively, between the analytical and numerical solutions. This is further illustrated in Figure 1.8 for a larger $P_0^* = 0.45$, which gives $P_0^{*2} = 0.203$ such that the same $M^* = 0.100$ satisfies Eq. 1.31 approximately. The difference between the analytical and numerical solutions for $P_0^* = 0.45$ is smaller than that for $P_0^* = 0.225$.

Eq. 1.31 can be equivalently written (dimensionally) as a limit to the electric current

$$i \ll \frac{a^4}{\mu L}\frac{F}{RT}P_0^2 \tag{1.32}$$

to ensure that the analytical solution in Eq. 1.29 is accurate. Eq. 1.31 is independent of the flexible membrane material and geometrical parameters. Therefore, only the fluidic, electrochemical, and environmental pressure terms can be adjusted to satisfy the condition in Eq. 1.29.

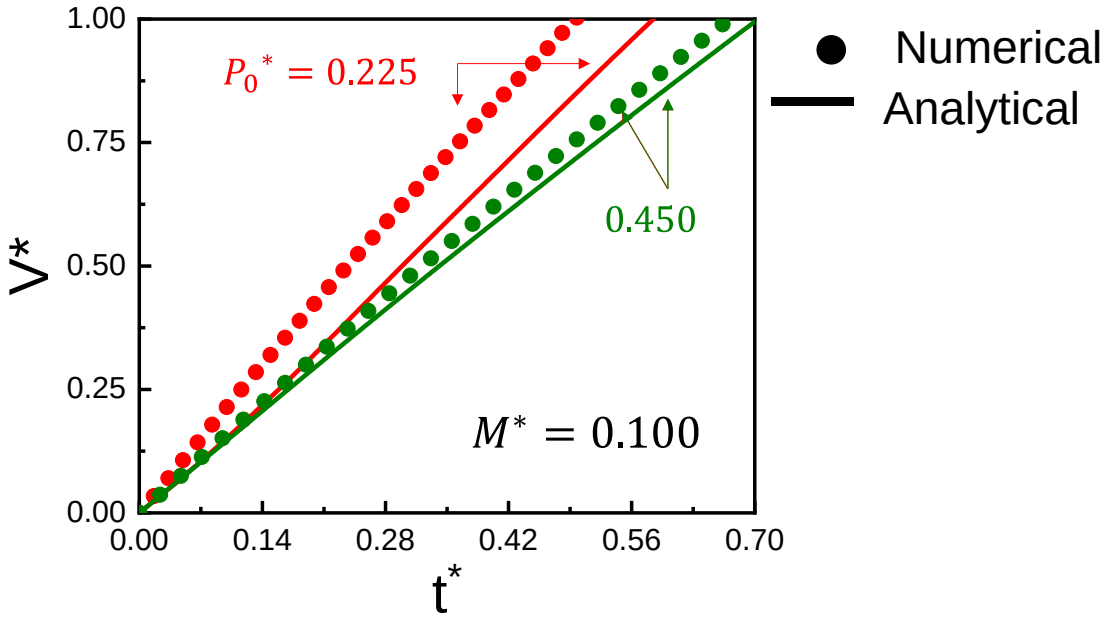

Figure 1.8. Non-dimensional volume temporal profiles from the numerical solution and from the analytical model with stretching-dominated deformation for a SBS membrane and the normalized environmental pressure $P_0^* = 0.225$ and 0.450. The normalized microfluidic resistance is $M^* = 0.100$.

The influence of the stress-strain behavior in the drug delivery process, captured via $G(V^*)$ in Figure 1.7, is shown in Figure 1.9 for the two representative polymers SBS and SIS. For fixed $P_0^* = 0.225$ and $M^* = 0.0170$, the curves are the same straight line up to $t^* = 0.15$. After this time, the curves separate due to different stress-strain behavior shown in Figure 1.5.

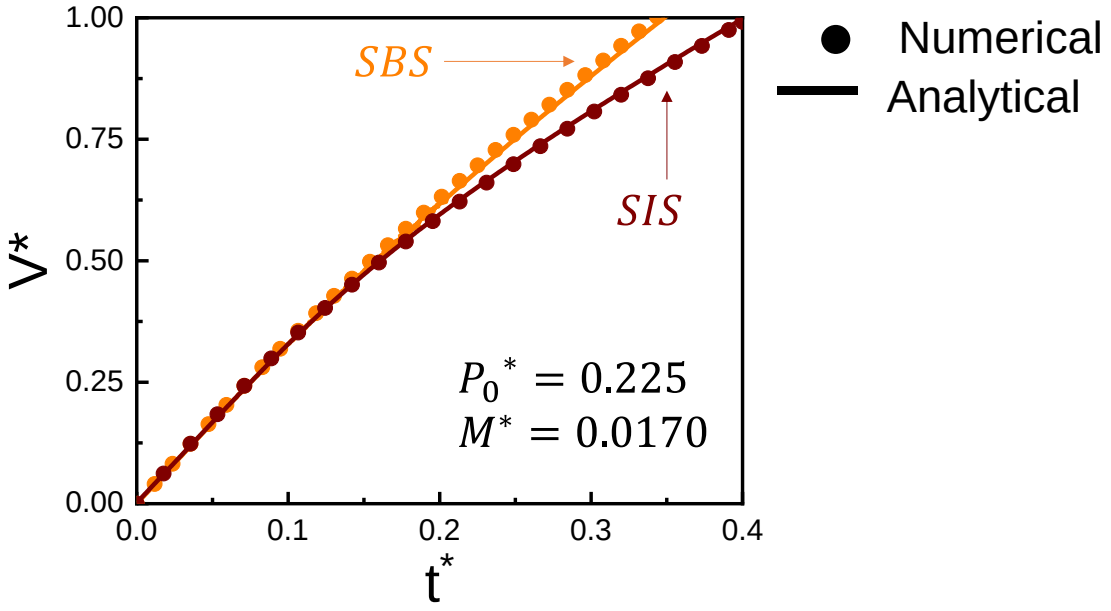

Figure 1.9. The volume temporal profiles for SBS and SIS copolymers with the non-dimensional parameters $P_0^* = 0.225$ and $M^* = 0.0170$.

1.10.

Effect of the Parameters in the Drug Delivery Time

Modifying the parameters to program the delivery will affect the different subsystems as follows:

Electrochemical reservoir. The temperature T of the electrolyte is taken as the room temperature, though it may increase by a few degrees when the device is implanted in the human or animal body, increasing M^* therefore the drug delivery time slightly. The current i has the opposite effect, i.e., the drug delivery time decreases as the current increases. Eqs. 1.29 and 1.27 suggest that the drug delivery time is linear (but not linearly proportional) to $(Ti)^{-1}$.

Flexible membrane. Increase of membrane stiffness Eh or decrease of membrane radius R_0 will delay drug delivery, i.e., leading to increase of drug delivery time. Therefore, a softer, thinner, and larger membrane is preferred for faster delivery applications.

Microfluidics. The value of P_0 depends on the target location (i.e., internal organ pressure) and it is difficult to manually change. Despite this, increasing P_0 therefore P_0^* delays drug delivery for a fixed volume as shown in Fig. 1.8. The drug delivery time increases with the viscosity μ and microchannel length L, and the cross-section size a has the opposite effect. Eqs. 1.29 and 1.27 suggest that the drug delivery time is linear (but not linearly proportional) to $\mu L/a^4$.

Effect of the Membrane Radius for Expedite Delivery

1.11 For a target drug volume V, the delivery time decreases but approaches an asymptote as the radius of flexible membrane R_0 increases and $f(V)$ becomes negligible as

$$t = \frac{4F}{3iRT} P_0 V + \frac{32\mu L}{a^4} \frac{V}{P_0} \tag{1.33}$$

Therefore, for a fixed drug volume V, increasing R_0 can significantly decrease the delivery time before approaching the asymptote. However, the overall device size must be carefully considered when designing these bioelectronic systems as a large R_0 can lead to bulky devices that pose bio-integration challenges in device securing or implantation strategies for epidermal or implantable applications, respectively. Figure 1.10 demonstrates that for a device with a drug volume $V = 125$ µl , $h = 0.15$ mm and $R_0 = 5 - 10$ mm, the total delivery time for $R_0 = 5$ mm is approximately $t = 260$ seconds. When $R_0 = 10$ mm, the delivery time is substantially reduced (by ~74%) to $t = 68$ seconds, beyond this point further increasing the radius results in almost negligible improvement as it approaches the asymptote value given in Eq. 1.33.

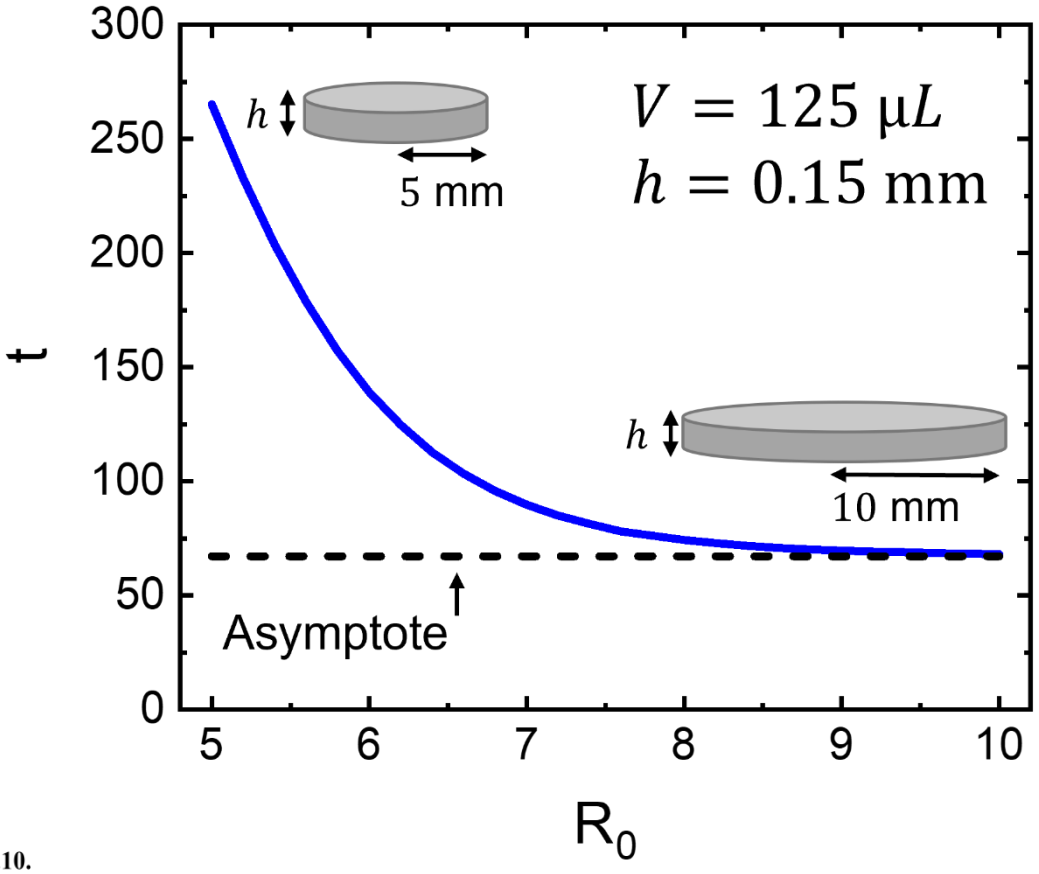

Figure 1.10.

Optimization of the membrane radius for fast delivery. For a representative fixed drug volume $V = 125\mu L$ used for delivery in large animal experiments, increasing R_0 from 5 mm to 10 mm results in the largest decrease in delivery time. Further increasing the radius yields negligible results. The R_0 changes while all the other parameters in the delivery are fixed. The initial gas volume V_0 is taken as zero to speed up the delivery and the initial current i is fixed to 10 mA.

1.12.

Analytical Model for the Flowrate – Slow Variable

In general, the microfluidic resistance M^* is small, as compared to the other two non-dimensional parameters P_0^* and V_0^*, but not zero ($M^* \ll 1$) such that the perturbation method [41] can be used to solve the governing equation in Eq. 1.5 analytically [42] or the drug delivery time as

$$t^* = P_0^* V^* + G(V^*)(V^* + V_0^*) + M^* \left[\frac{V^* + V_0^*}{P_0^* + G(V^*) + G'(V^*)(V^* + V_0^*)} - \frac{V_0^*}{P_0^* + G'(0)V_0^*} \right] \tag{1.34}$$

which is written explicitly for the total non-dimensional delivery time t^* that it takes to deliver a non-dimensional volume of drug V^*. The first two terms on the right side of Eq. 1.34 can be regarded as the time required for the flexible membrane to deform and overcome the external environmental pressure and the last term is as the time for the drug to travel through the microfluidic channels where both times occur simultaneously, i.e., as the flexible membrane deforms it pumps the drug through the microchannels. Let $V^* = V_{slow}^*(t^*)$ denote the solution of the above equation, where the subscript "slow" is used to denote a function of the regular (slow) time t^* (as opposed to the fast time introduced in the next section). The flowrate of the "slow" variable solution is obtained by taking its derivative with respect to time in Eq. 1.34 as

$$\frac{dV_{slow}^*}{dt^*} = \left\{ P_0^* + G(V^*) + G'(V^*)(V^* + V_0^*) + M^* \frac{P_0^* - G'(V^*)(V^* + V_0^*) - G''(V^*)(V^* + V_0^*)^2 + G(V^*)}{[P_0^* + G(V^*) + G'(V^*)(V^* + V_0^*)]^2} \right\}^{-1} \tag{1.35}$$

It is important to note that Eq. 1.35 gives a non-zero initial flowrate that is equal to

$$\left.\frac{dV^*_{slow}}{dt^*}\right|_{t^*=0} = \left\{P^*_0 + G'(0)V^*_0 + M^*\frac{P^*_0 - G'(0)V^*_0 - G''(0)V^{*2}_0}{[P^*_0 + G'(0)V^*_0]^2}\right\}^{-1} \quad (1.36)$$

which does not satisfy the zero-flowrate initial condition $\left.\frac{dV^*}{dt^*}\right|_{t^*=0} = 0$.

Analytical Model for the Flowrate – Fast Variable

1.13 The "slow" variable solution $V^* = V^*_{slow}(t^*)$ presented in the previous section works well when M^* is small except at the initial delivery time because it does not satisfy the zero-flowrate initial condition. Since M^* appears as the highest order derivative in the "slow" variable solution for the flowrate in Eq. 1.35 and is small, the singular perturbation method can be used to introduce a "fast" variable solution of the form $M^*V^*_{fast}(\eta)$ where the $\eta = \frac{t^*}{M^*}$ is a "fast" changing variable and the presence of M^* ensures a small effect on the volume temporal profile but a large effect initially in the flowrate to satisfy the zero-flowrate initial condition.

The total drug delivery time in Eq. 1.34 then becomes $V^* = V^*_{slow}(t^*) + M^*V^*_{fast}(\eta)$, where t^* is the "slow" variable and $\eta = \frac{t^*}{M^*}$ is a "fast" changing variable that is relevant near the initial time of the delivery process to ensure a zero initial flowrate. Therefore, for a finite η and a very small M^*, the value of ηM^* is approximately zero such that $V^*_{slow}(t^* = 0) = 0$, $G(0) = 0$, and $\left.\frac{dV^*_{slow}}{dt^*}\right|_{t^*=0}$ is a constant value given from Eq. 1.36 and these assumptions can be used to derive V^*_{fast} as

$$V_{fast}^{*} = -\frac{V_0^{*}}{P_0^{*} + G'(0)V_0^{*}} \frac{dV_{slow}^{*}}{dt^{*}}\Big|_{t^{*}=0} \langle 1 - e^{\left\{-\left[\frac{P_0^{*}}{V_0^{*}}+G'(0)\right]\frac{t^{*}}{M^{*}}\right\}} \rangle \tag{1.37}$$

The flowrate term of the "fast" variable solution is obtained from Eq. 1.37 by taking a derivative as

$$\frac{dV_{fast}^{*}}{d\eta^{*}} = -\frac{dV_{slow}^{*}}{dt^{*}}\Big|_{t^{*}=0} e^{\left\{-\left[\frac{P_0^{*}}{V_0^{*}}+G'(0)\right]\eta\right\}} \tag{1.38}$$

The complete expression for the flowrate is $\frac{dV^{*}}{dt^{*}} = \frac{dV_{slow}^{*}}{dt^{*}} + \frac{dV_{fast}^{*}}{d\eta}$. For time $t^{*} = 0$, Eq. 1.38 becomes $\frac{dV_{fast}^{*}}{d\eta^{*}}\Big|_{\eta=0} = -\frac{dV_{slow}^{*}}{dt^{*}}\Big|_{t^{*}=0}$ to satisfy the initial condition of zero initial flowrate.

The results in Figure 1.11 show the flowrate temporal profile for a representative bioelectronic device with a SIS flexible membrane previously used for combined drug and light delivery in the mouse brain [15] with the parameters listed in Table 1 and shows the numerical, semi-analytical, and analytical solutions of the flowrate and its maximum value. Figure 1.11A and 1.11B both show the numerical solution and "semi-analytical slow + fast" solution, and they begin with an initial zero flowrate and increase until reaching a peak value labeled as the maximum flowrate and then gradually decrease as the drug delivery process continues. The main difference between the "semi-analytical slow" and "semi-analytical slow + fast" solutions in Figure 1.11A is at the beginning of the delivery process (i.e., $t = 0$) showing that the "semi-analytical slow" solution does not satisfy the zero initial flowrate, but the "semi-analytical slow + fast" solution does due to the introduction of the "fast" variable $\eta = \frac{t^{*}}{M^{*}}$ which dominates at the beginning of the delivery process. Both semi-analytical solutions in Figure 1.11A closely match the numerical

solution after the initial time because the function $f(V)$ is obtained from FEA based on the Marlow hyperelastic model and it considers both the bending and stretching effects of the deformation. Thus, just like in the previous volume temporal profile models [42-44] modeling the flowrate temporal profile requires excellent agreement between the FEA and analytical function $f(V)$.

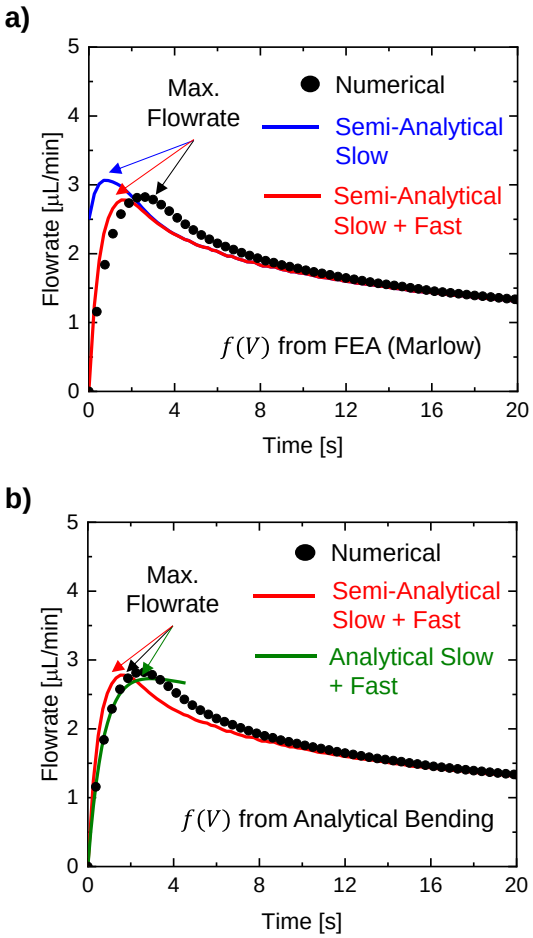

Figure 1.11.

Flowrate temporal profile during drug delivery. (A) representative example of the flowrate temporal profile obtained from the numerical, semi-analytical slow, and semi-analytical slow + fast solutions for a bioelectronic device when the function $f(V)$ is obtained from finite element analysis (FEA) using the Marlow hyperelastic. The maximum flowrate is labeled as the peak value of the flowrate temporal profile. (B) representative example of the flowrate temporal profile showing the analytical slow + fast solution where the function $f(V)$ is obtained from bending-dominated deformation. The dimensions of the flexible membrane are thickness h = 150 μm and radius R_0 = 1.20 mm. The electrical current is 0.5 mA and the cross section of the microchannels is 50 μm The three non-dimensional values are M^* = 0.0009, P_0^* = 0.1013, and V_0^*= 0.9162.

However, since the maximum flowrate always occurs at the beginning of the drug delivery process when the bending effects in the flexible membrane are prevalent, the FEA function $f(V)$ can be replaced by the linear $f(V)$ function given in Eq. 1.17 for bending-dominated deformation

to model the drug delivery process up to the point where the maximum flowrate is reached. For this bioelectronic device geometry specifically (i.e., thickness h = 150 μm, and radius R_0 = 1.2 mm), the bending effects in the membrane cannot be neglected when controlling the maximum flowrate. Figure 1.11B shows that the "analytical slow + fast" using the in $f(V)$ given in Eq. 1.17 satisfies the zero initial flowrate condition due to the presence of the "fast" variable and has excellent agreement with the numerical solution up to the point of the maximum flowrate which is the key quantity of focus in this analysis. It is important to note that the bending-dominated deformation $f(V)$ can only be used up to the time point when the maximum flowrate is reached while the deformation remains small, otherwise, a stretching-dominated $f(V)$ or the FEA solution $f(V)$ is necessary. The reason why the bending-dominated solution $f(V)$ is relevant in this particular case is twofold: 1) the maximum flowrate always occurs near the beginning of the drug delivery process when the deformation is small and therefore bending-dominated and 2) the flexible membrane bending effects depend on the non-dimensional ratio $\frac{h}{R_0} = 0.125$ which is almost five times higher than bioelectronic devices handling larger drug volumes (e.g., 100 – 1000 μL) that focus on achieving faster drug delivery $\frac{h}{R_0} = 0.03$ where a larger membrane radius ensures stretching-dominated deformation [43] and the control is on the drug delivery time and volume instead of the flowrate and its maximum value. However, for compact bioelectronics with drug delivery capabilities for use in small animals, the key quantity to control is the magnitude of the maximum flowrate to avoid damaging surrounding fragile tissues resulting from excessively high flowrates, not the volume or temporal profile as shown in our previous work [42-44] where the focus was to obtain the total delivery time and volume.

Analytical Model for the Maximum Flowrate

The flowrate temporal profiles in Figure 1.12A show that the maximum flowrate occurs near the beginning of the drug delivery process. Currently, the "analytical slow + fast" solution for the flowrate is divided into the "slow" and "fast" terms given by $\frac{dV^*}{dt^*} = \frac{dV^*_{slow}}{dt^*} + \frac{dV^*_{fast}}{d\eta}$ and the exact time when the maximum flowrate occurs can be obtained from $\frac{d^2V^*}{dt^{*2}} = \frac{d^2V^*_{slow}}{dt^{*2}} + \frac{1}{M^*}\frac{d^2V^*_{fast}}{d\eta^2} = 0$, which, however, is difficult to yield an explicit formula for the exact time when the maximum flowrate occurs. When time is small, such as in the beginning of the delivery process (i.e., $t^* = 0$), the term $\frac{d^2V^*_{slow}}{dt^{*2}}$ can be approximated by the constant $\left.\frac{d^2V^*_{slow}}{dt^{*2}}\right|_{t^*=0}$ because in the "slow" variable solution the maximum flowrate always occurs near $t^* = 0$ but η in the "fast" variable solution is not zero and must be determined. Then, the approximate time when the maximum flowrate occurs can be rewritten as

$$\frac{d^2V^*}{dt^{*2}} = \left.\frac{d^2V^*_{slow}}{dt^{*2}}\right|_{t^*=0} + \frac{1}{M^*}\frac{d^2V^*_{fast}}{d\eta^2} = 0 \tag{1.39}$$

Where the first term in the right-hand side of Eq. 39 is a constant and the second term is only a function of η. This gives an explicit formula for η at which the maximum flowrate occurs, and its substitution into the flowrate expression $\frac{dV^*}{dt^*} = \left.\frac{dV^*_{slow}}{dt^*}\right|_{t^*=0} + \frac{dV^*_{fast}}{d\eta}$ gives an explicit formula for the maximum flowrate as

1.14.

$$\max\left(\frac{dV^*}{dt^*}\right) = [P_0^* + G'(0)V_0^*]^{-1}\left[1 - M^*\frac{1}{[P_0^* + G'(0)V_0^*]^2}\right] \tag{1.40}$$

Since the bending effects are relevant at the beginning of the drug delivery process when the maximum flowrate occurs the expression for $G'(0)$ can be derived from Eq. 1.17 as $G'(0) = \frac{64}{3\pi}\frac{h^2}{R_0^2}$. The explicit non-dimensional expression for the maximum flowrate becomes

$$\max\left(\frac{dV^*}{dt^*}\right) = \left[P_0^* + \frac{64}{3\pi}\frac{h^2}{R_0^2}V_0^*\right]^{-1}\left[1 - M^*\frac{1}{\left[P_0^* + \frac{64}{3\pi}\frac{h^2}{R_0^2}V_0^*\right]^2}\right] \tag{1.41}$$

that depends on the ratio $\frac{h}{R_0}$ (due to the bending effects) and the three non-dimensional parameters P_0^*, V_0^*, and M^* described in the beginning of the chapter. Typically, in these bioelectronic devices with the representative parameters listed in Table 1, the electrical current can be modulated to control (increase or decrease) the maximum flowrate as shown in Figure 1.12A where the electrical current is changed from 0.10 mA to 1.00 mA which in turn increases the maximum flowrate from 0.60 μl/min to 5.20 μl/min. The corresponding non-dimensional parameters for this example are calculated and shown in Figure 1.10A for comparison where M^* increases from 0.0002 to 0.0018 when the electrical current changes and the other two non-dimensional parameters P_0^*, and V_0^* are fixed since they do not depend on the electrical current.

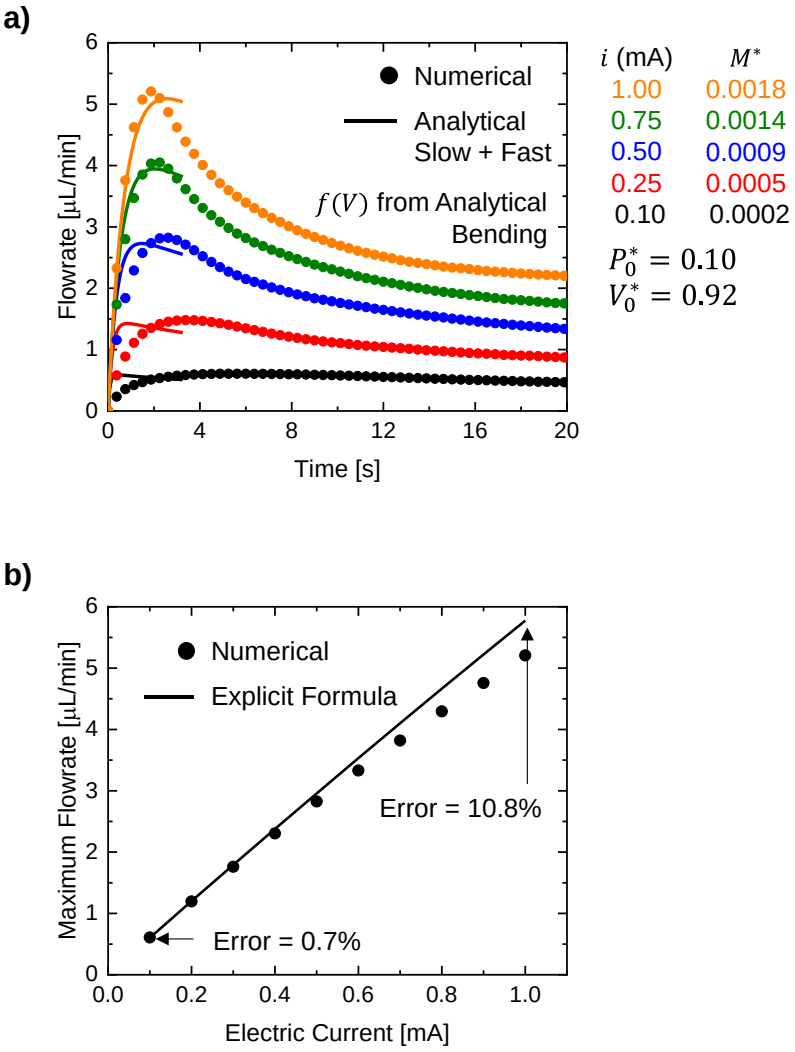

Figure 1.12.

Maximum Flowrate. (A) drug delivery temporal flowrate showing the maximum (peak) flowrate value when the electrical current changes from 0.10 mA to 1.00 mA. (B) maximum flowrate as a function of the electrical current. The dimensions of the flexible membrane are thickness h = 150 µm and radius R_0 = 1.20 mm. The cross section of the microchannels is 50 µm The two non-dimensional values are P_0^* = 0.1013, and V_0^*= 0.9162.

The "analytical slow + fast" solution in Figure 1.12A shows excellent agreement up to the time when the maximum flowrate is reached, after, the agreement deteriorates for larger current values (e.g., 0.75 and 1.00 mA) due to 1) the magnitude of M^* increases and 2) the differences between the function $f(V)$ obtained from FEA and bending-dominated deformation in Eq. 1.17.

Most notably, the magnitude of the maximum flowrate shows excellent agreement between the numerical and "analytical slow + fast", which is the key quantity to control during the drug delivery process to avoid damaging fragile surrounding tissues. Figure 1.12B shows the excellent agreement of the value for the maximum flowrate obtained from the explicit analytical formula in Eq. 1.41 with the numerical values computed from the peaks in the flowrate temporal profile. When the electrical current is less than 0.50 mA, the agreement between the numerical and explicit formula is excellent. As the electrical current increases to 1.00 mA, the explicit formula overpredicts the maximum flowrate by ~10.8%, which is still a reasonable agreement, which validates the explicit analytical expression in Eq. 1.41 for the maximum flowrate.

1.15. Parametric Study of the Maximum Flowrate

The maximum flowrate in Eq. 1.40, like the scaling law in Eq. 1.5, depends on the three non-dimensional parameters P_0^*, V_0^*, and M^*. Therefore, understanding how the maximum flowrate scales with each of the three non-dimensional parameter is important to design and optimize the bioelectronic device geometry and ensure safe and successful drug delivery. To explore the influence of M^*, the cross-sectional area of the microfluidic channel a is reduced from 50 μm to 18 μm which in turn increases M^* to 0.027 while the other two non-dimensional parameters are fixed to $P_0^* = 0.10$, and $V_0^* = 0.92$. This cross-section reduction is relevant when targeting smaller areas (or cells) within the tissues to ensure that the drug is being delivered only in a specific region. Figure 1.13A shows that the maximum non-dimensional flowrate decreases approximately non-linearly with M^*, this non-linearity is clearly captured from the flowrate temporal profile peaks in the "analytical slow + fast" model as shown by the excellent agreement with the numerical solution.

The explicit formula in Eq. 1.41 has a linear dependence on M^* as shown in Figure 1.13A and provides an excellent agreement when M^* is small (key assumption when using the perturbation method) and a reasonably well analytical approximation to the non-dimensional maximum flowrate when M^* increases over the relevant range of microchannel cross-sections.

To study the influence of V_0^*, which is relevant in the refill ability aspect of the bioelectronic device, the other two non-dimensional parameters were fixed to $P_0^* = 0.1000$, and $M^* = 0.0011$. Figure 1.13B shows that both the "analytical slow + fast" and the explicit formula agree extremely well with the numerical solution in the range $V_0^* = 0 - 1.3$, which corresponds to the electrolyte reservoir being completely full $V_0^* = 0$ and partially full (i.e., 50%) that introduces the presence of an initial gas volume $V_0^* = 1.3$. Here, the explicit formula, slightly over predicts within ~6% the magnitude of the non-dimensional maximum flowrate.

To understand the influence of P_0^*, the other two non-dimensional parameters are fixed to $V_0^* = 0.9200$, and $M^* = 0.0011$. Significantly changing the value of P_0^* is difficult as it depends on the initial environmental pressure of the target organ which might vary only by a few kilopascals in humans. Figure 1.13C shows that the "analytical slow + fast" and the explicit formula agree very well with the numerical solution.

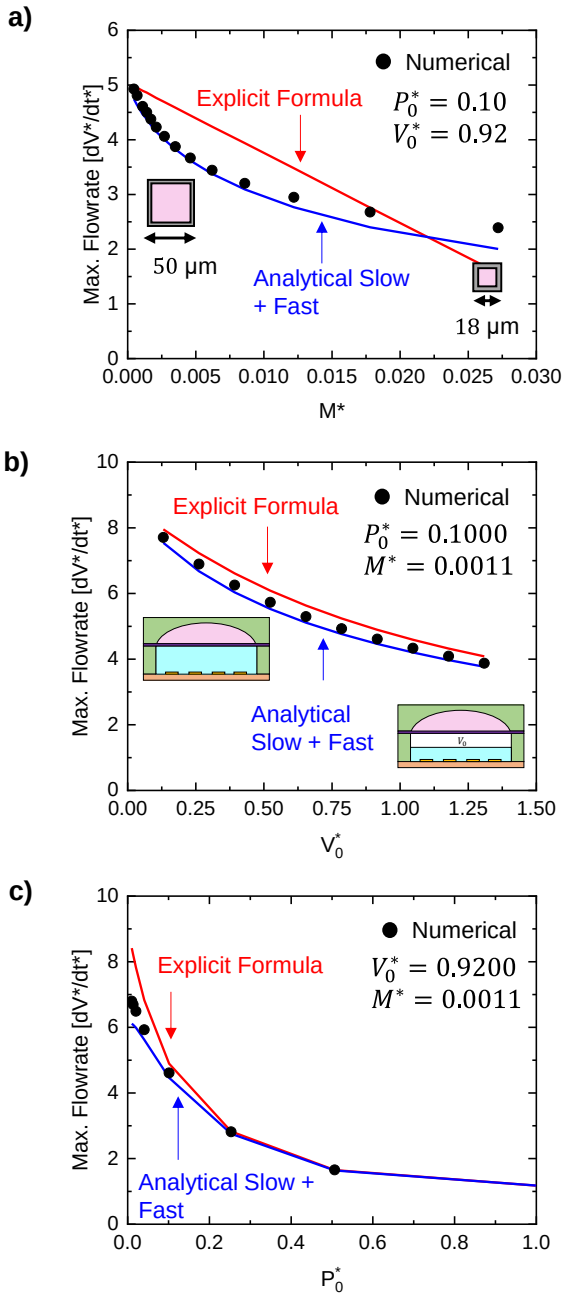

Figure 1.13.

Parametric Study of the Maximum Flowrate. Changes in the maximum flowrate when (A) the microchannel cross-section is reduced from 50 μm to 18 μm which increases the non-dimensional parameter M^*, (B) the electrolyte chamber goes from full to partially full (50%) which introduces an initial gas volume via the non-dimensional parameter V_0^*, and (C) the initial environmental pressure in the tissue/organ changes which affects the non-dimensional parameter P_0^*. The dimensions of the flexible membrane are thickness h = 150 μm and radius R_0 = 1.20 mm.

The introduction of a "fast" variable analytical model and the explicit formula for the maximum flowrate in provide a theoretical framework to control the maximum flowrate by changing any of the three non-dimensional parameters P_0^*, V_0^*, and M^*. Future flexible bioelectronic systems with drug delivery capabilities can be designed by explicitly considering the influence of geometric dimensions, electronics, flexible membrane mechanics, and microfluidic geometries. For example, wireless drug delivery devices in neuroscience experiments aim to be small and lightweight such as to not influence the behavior of the small animal during experiments. This design goal of achieving a small and functional device can be achieved by carefully studying the unique combinations of the non-dimensional parameters to yield the optimal configuration for the bioelectronic device.

After the bioelectronic device is fabricated, only the initial gas volume and electric current can be modified. The initial gas volume can be changed during the refilling process between experiments and the electric current can be modified by operating at different duty cycles. Restrictions in size and geometric dimensions affect the device radius and available electric current and these effects can be modeled using the non-dimensional parameters to identify if the bioelectronic device is able to reach the desired maximum flowrate range during delivery before fabricating the device. Further, the influence of the flexible membrane mechanics can be explicitly considered to use a block copolymer with Young's modulus that deform quickly with the applied pressure (i.e., soft) and helps achieve the desired maximum flowrate. Similarly, the influence of the microfluidic channel geometry and dimensions can be considered explicitly such as to not impose excessive fluid resistance that can delay the delivery or cause a blockage inside the device while still targeting drug delivery in specific locations.

For example, Figure 1.13A shows that changing the cross-section of the microchannel from 50 μm (delivery area 2500 μm^2) to 18 μm (delivery area 324 μm^2) will decrease the maximum flowrate during delivery which can be important to consider especially when interested in drug delivery to cells with dimensions in the tens of μm or less. The separation of the flowrate solution into a "slow" variable (which is relevant to determine the total delivery time) and a "fast" variable (which is relevant to satisfy the zero-flowrate initial condition at the beginning of the drug delivery process) allow to prioritize which dimensional parameters (and consequently non-dimensional parameters) to change depending on the quantity to control, e.g., delivery time or flowrate and its maxima and most importantly how to change them to increase or decrease the maximum flowrate based on the linear dependence on M^* and inverse linear dependence on P_0^* and V_0^* shown in Eq. 1.41 which can be used to control the maximum flowrate when changing the microchannel cross-section to target smaller region in the organs, initial volume of gas during refill and reuse process, and the physiological pressure of the target region organ as shown in Figure 1.13. For example, the proposed analytical model can be used to design the bioelectronic device to comply with the maximum flowrate applications in neuroscience and tailor specific experiments, target locations, drug delivery timeframe, and animal size.

The physics of the maximum flowrate are presented as: the first term in Eq. 1.41 is the maximum flowrate achieved while the flexible membrane is overcoming the external pressure to deform and the second term (which is a negative term of the non-dimensional parameter M^*) is the delayed effect caused by the drug traveling through the microchannels. The relevance of the "slow + fast" variable analytical model in the context of time sensitive experiments in freely moving animals is 1) provides control over the rates of drug delivery which are important in many

behavioral neuroscience studies and the total time to deliver the drug and 2) the "fast" variable model allows to determine the time required to reach the maximum flowrate to enable safe wireless pharmacology experiments. The benefits of employing the "analytical slow + fast" variable over the numerical model and FEA to design this emerging class of bioelectronic devices is 1) the iterative design and optimization process can be done in minutes to properly tune the maximum flowrate by studying only the unique combinations of the non-dimensional parameters, subject to practical limits in the fabrication process, rather than each individual dimensional parameter (e.g., electric current, device and microchannel geometries) and help to study only optimized geometries that need to be characterized experimentally using micro particle tracking velocimetry, a confocal microscope technique used to examine flow rate characteristics in microfluidic devices with drug delivery capabilities.

Noting that the "slow + fast" variable analysis presented here is for a bioelectronic device where the bending effects in the polymer flexible membrane are not negligible since the maximum flowrate occurs at the beginning of the delivery process, a similar analysis can be performed for bioelectronic devices mainly experiencing large deformation (i.e., stretching-dominated deformation) to determine the total drug delivery time, flowrate, and its maximum value. Although further experimental testing is required to scale these bioelectronics from small animals to medium and large animals for targeted drug delivery studies, the proposed "slow + fast" variable analytical model for the flowrate and its maxima provides a scalable understanding to control the flowrate via P_0^*, V_0^*, and M^* during the drug delivery process.

Summary

This chapter presents an analytical model to accurately describe the drug delivery process, with a focus on electrochemical microsystems with flexible membranes based on the time and flowrate.

1.16.

Analytical modeling, performed in a manner that includes the effects of microfluidic and flexible membrane resistance ignored in previous models, quantitatively reproduces the numerical results and experimental measurements. The results show that the simple analytical model can be used to determine the drug delivery time and maximum flowrate in large and small microsystems. These conclusions and the detailed analysis are important for the emerging applications of microsystems, with electrochemical actuation, in drug delivery studies.

CHAPTER 2

Engineering a Wireless Bioresorbable Pacemaker for Temporary Cardiac Pacing

Temporary cardiac pacemakers provide critical functions in pacing through periods of need during post-surgical recovery. The percutaneous leads and externalized hardware associated with these systems represent, however, risks of infection and constraints on patient mobility. Furthermore, the pacing leads can become enveloped in fibrotic tissue at the electrode-myocardium interface, thereby increasing the potential for myocardial damage and perforation during lead removal. Here, we report a bioresorbable, leadless, and fully implantable cardiac pacemaker for post-operative control of cardiac rate and rhythm during a stable operating timeframe, followed by complete dissolution and clearance via natural biological processes. A combined set of *in vitro*, *ex vivo*, and *in vivo* studies across mouse, rat, rabbit, canine, and human cardiac models demonstrates that these devices provide an effective, battery-free means for pacing the hearts of various sizes with tailored geometries and timescales for operation and bio resorption. These features enable programmable cardiac pacing in a manner that overcomes all the key disadvantages of traditional temporary pacing devices. As such, this novel technology may serve as the basis for the next generation of post-operative temporary pacing technology.

Background

Implantable cardiac pacemakers are the cornerstones of therapy for bradyarrhythmias. As a complement to traditional pacemakers designed as permanent implants, temporary systems provide essential demand-based atrial and/or ventricular pacing for patients where bradyarrhythmias are expected to be short lived, such as on the order of days or weeks1. Such devices either act as a bridge to permanent pacing therapy [45] or are implemented temporarily following cardiac surgery [46] when postsurgical bradycardia is frequently encountered. Temporary pacing systems consist of an external generator with one or two transcutaneous pacing leads that are placed, depending on the clinical context, either epicardially or transvenously. This hardware, however, carries substantial risk of complications. First, bacteria can form biofilms on foreign materials/devices such as pacing leads [47–50], and transcutaneous access can serve as a focus for infections [51–54]. Second, because the device is not fully implanted, the externalized power supply and control system can be inadvertently dislodged when caring for or mobilizing the patient. Third, removal of temporary transcutaneous devices following completion of therapy can cause laceration and perforation of the myocardium since the pacing leads can become enveloped in fibrotic tissue at the electrode–myocardium interface [55–57]. These circumstances create a unique need for an alternative temporary pacemaker technology that can deliver the necessary electrotherapy while addressing the associated physiological complications.

Design and Operation of Bioresornable Cardiac Pacemaker

The schematic illustration in Figure 2.1A shows a thin, flexible, bioresorbable, leadless cardiac pacemaker on the surface of a heart. As part of the surgical implantation process, an integrated

contact pad that contains two dissolvable metallic electrodes (i.e. bipolar channels) is attached to the myocardium. As shown in Figure 2.1.A (middle), the wireless power harvesting part of the system includes a loop antenna with a bilayer, dual-coil configuration (tungsten-coated magnesium (W/Mg); ~700 nm / ~50 μm thick), a film of a poly(lactide-co-glycolide) (PLGA) 65:35 (lactide:glycolide) as a dielectric interlayer (~50 μm thick), and a radiofrequency (RF) PIN diode based on a doped monocrystalline silicon nanomembrane (Si NM; ~320 nm thick). A strip of double layered electrode (W/Mg; ~700 nm / ~50 μm thick) with an opening at the end serves as an electrical extension and connector to deliver electrical stimuli from this receiver (Rx) antenna to the myocardium. This W/Mg electrode design and the layout of the PIN diode enables non-invasive monitoring of the processes of bioresorption using coherence tomography and a capacitor-free rectifier with high efficiency, respectively. These two features represent key, enabling advances that support the cardiac pacing application reported here, absent from analogous peripheral nerve stimulators reported previously [58]. The exposed pair of electrodes (2.0 × 1.4 mm^2) includes adjacent holes (700 μm diameter) as points for suturing to the heart with bioresorbable suture (Ethicon, MV-J451-V). A composite paste of Candelilla wax and tungsten (W) micro-particles provides electrical interconnection [59]. Two layers of PLGA 65:35 define a top and bottom encapsulation (100 μm thickness) structure around the entire system to isolate the active materials from the surrounding biofluids during the period of implantation. The geometry of the entire system is small, thin (~0.05 cc; width: ~16 mm; length: > 15 mm; thickness: ~250 μm) and lightweight (~0.3 g).

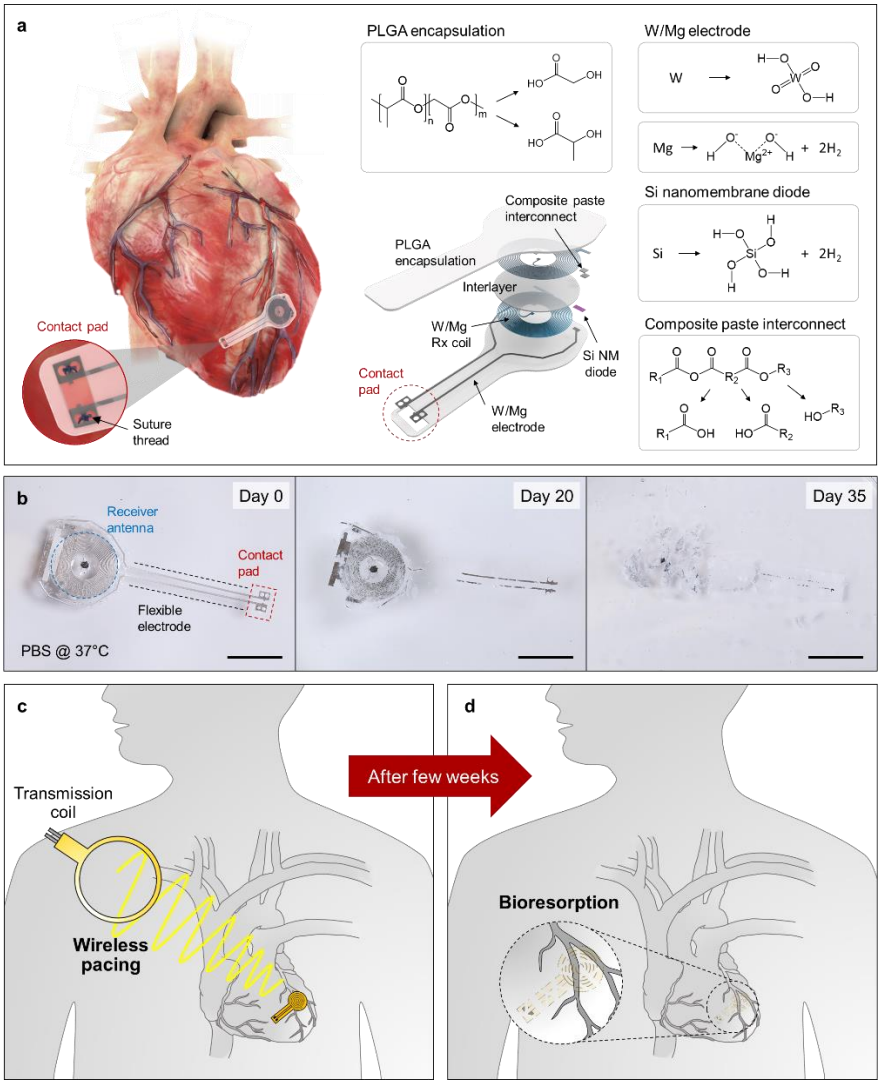

Figure 2.1.

Materials, design, and proposed utilization of a bioresorbable, implantable, leadless, battery-free cardiac pacemaker. (A) Schematic illustration of the device mounted on the myocardial tissue. The electronic component consists of three functional parts: a wireless receiver, a radiofrequency PIN diode, and a dielectric interlayer. All components of the device naturally bio resorb via hydrolysis and metabolic action in the body. (B) Images of dissolution of a device associated with immersion in PBS (pH = 7.4) at physiological temperature (37°C). Scale bar, 10 mm. (C) Schematic illustration of the wireless and battery-free operation of an implanted device via inductive coupling between an external transmission coil (Tx) and the receiver (Rx) coil on the device. (D) Bio resorption thereby eliminates the device after a period of therapy, to bypass needs for device removal.

The key defining characteristic of this system is that all the constituent materials are bioresorbable as shown in Figure 2.1B. The designs support stable function over a relevant timeframe but eventual, complete disappearance by natural chemical/biochemical processes into the surrounding biofluids and eventually from the body itself. Specifically, the materials resorb via hydrolysis and metabolic action [60]. For example, PLGA dissolves by hydrolysis into its monomers, glycolic and lactic acid [61]. The Mg, Si NM and W disappear into non-toxic products, according to ($Mg + 2H_2O \rightarrow Mg(OH)_2 + H_2$), ($Si + 4H_2O \rightarrow Si(OH)_4 + 2H_2$), and ($2W + 2H_2O + 3O_2 \rightarrow 2H_2WO_4$), respectively [62-64]. The Candelilla wax, which contains long-chain poly- and mono-unsaturated esters, fatty acids, anhydrides, short-chain hydrocarbons, and resins, undergoes hydrolysis and resorbs into the body [65]. Figure 2.1.B shows photographs of a typical device at various time points following immersion in a phosphate-buffered saline (PBS, pH 7.4) solution at physiological temperature (37°C). The constituent materials largely dissolve within five weeks, and remaining residues completely disappear after seven weeks to bypass the need for device removal as shown by the wireless operation in Figure 2.1C and device bio resorption in Figure 2.1D.

2.3.

Wireless Power Transfer to the Device

The power transfer for device operation depends on the mutual inductance between the Rx and Tx coils. This relationship is represented by $M = k\sqrt{L_{Tx}L_{Rx}}$, where the individual coil inductances are L_{Rx} and L_{Tx}. The coupling coefficient *k* defines the linkage of the magnetic flux, and the value mainly depends on the distance and relative angle between the coils [66-67]. Proper design choices ensure operation for average skin-to-heart distances in adult patients (parasternal 32.1 ± 7.9 mm;

apical 31.3 ± 11.3 mm; subcostal 70.8 ± 22.3 mm) [68]. Figure 2.2 shows the magnetic field strength distribution for the coupling between a planar spiral Rx coil (25 mm diameter) and a 3D spiral Tx coil (64 mm diameter; 4 turns; Power = 1 W). From Faraday's law of induction, the time rate of change of the magnetic flux through the Rx coil scales with its enclosed area to induce an output voltage. Thus, Rx coils with diameters smaller than 25 mm fail to meet the thresholds output voltage that is required for pacing the canine heart at 20 mm. The magnetic field strength increases with the square root of the transmitting power. The use of increased powers (2-12 W) and optimized (i.e. larger area and high coupling coefficient) Rx and Tx coil geometries increases the working distance to more than 200 mm, required for pacing patients with larger anatomical distances between the surface of the skin and the heart. *In vivo* pacing tests in a canine model validate the long-range wireless energy transfer capability of the bioresorbable pacing system. Here, the maximum pacing distance (i.e., distance between skin and Tx coil) is 17 cm, excluding the distance between Rx coil and the skin. Continuous pacing experiments in a fully equipped operation room for cardiac surgeries also confirm the absences of interference effects with standard electronic equipment, either due to or originating from the wireless, bioresorbable pacing system. The near field (~ 13.56 MHz) wireless energy transfer mechanisms lead to negligible changes in pacing signals during the continuous operation with skin-to-Tx coil distances of 10 cm. Overall, these *in vivo* tests suggest that the wireless power transfer system employed in the canine model can achieve the power transfer necessary for operation of bioresorbable pacemakers in human adult patients.

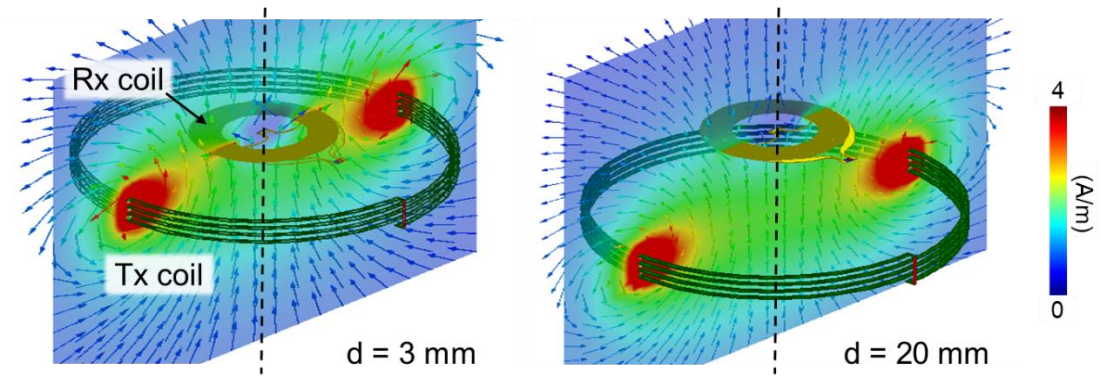

Figure 2.2. Long-range electromagnetic characteristics of bioresorbable, leadless cardiac pacemakers. Simulated results of the electromagnetic field distribution near the coupled Rx and Tx coils for a separation distance of (left) 3 mm and (right) 20 mm (transmitting power = 1 W).

2.4. Device Design Optimization for Long-Range Wireless Operation

The coil-to-coil distance is a critical factor that affects the power transfer efficiency in a wireless induction scheme [50, 68]. For example, for a fixed input voltage (i.e. transmitting voltage) of 10 V_{pp} at the Tx coil, the output voltage at the Rx coil decreases from 16 V to 0.2 V with distance from 1 mm to 8 mm, respectively. Figure 2.3 summarizes the electromagnetic characteristics of the bioresorbable device for wireless and battery-free operation. Alternating currents (sine wave) generated by a function generator provide a source of monophasic RF power to a transmission (Tx) antenna (that is, primary coil) placed near the power harvester component of the device. The Rx coil (that is, secondary coil) transforms the received waveform to an approximately direct current output via the RF diode and delivers it to the interface with the myocardium as shown in Figure 2.3A where cathodic direct current pulse through the electrode pads. An applied electrical stimulus above a threshold value initiates cardiac excitation because of depolarization of the transmembrane potential (that is, the difference in voltage between the inside and outside of the cell). This type of

inductive scheme is common for wireless power transfer in implanted medical devices [69, 70] because the magnetic coupling that occurs in this megahertz frequency regime (~13.5 MHz) avoids absorption by biofluids or biological tissues [69] as shown in Figure 2.3B, 2.3C and 2.3F. Figure 2.3D and 2.3E illustrates the RF power (~7 peak-to-peak voltage (Vpp) at a 1-mm coupling distance) applied to the Tx antenna and the resultant monophasic output (13.2 V) at the contact pad. As the distance between the coils increases from 3 mm to 20 mm, the coupling coefficient decreases, which consequently lowers the strength of the magnetic field in the receiver coil to result in a reduced output voltage as shown in Figure 2.3F.

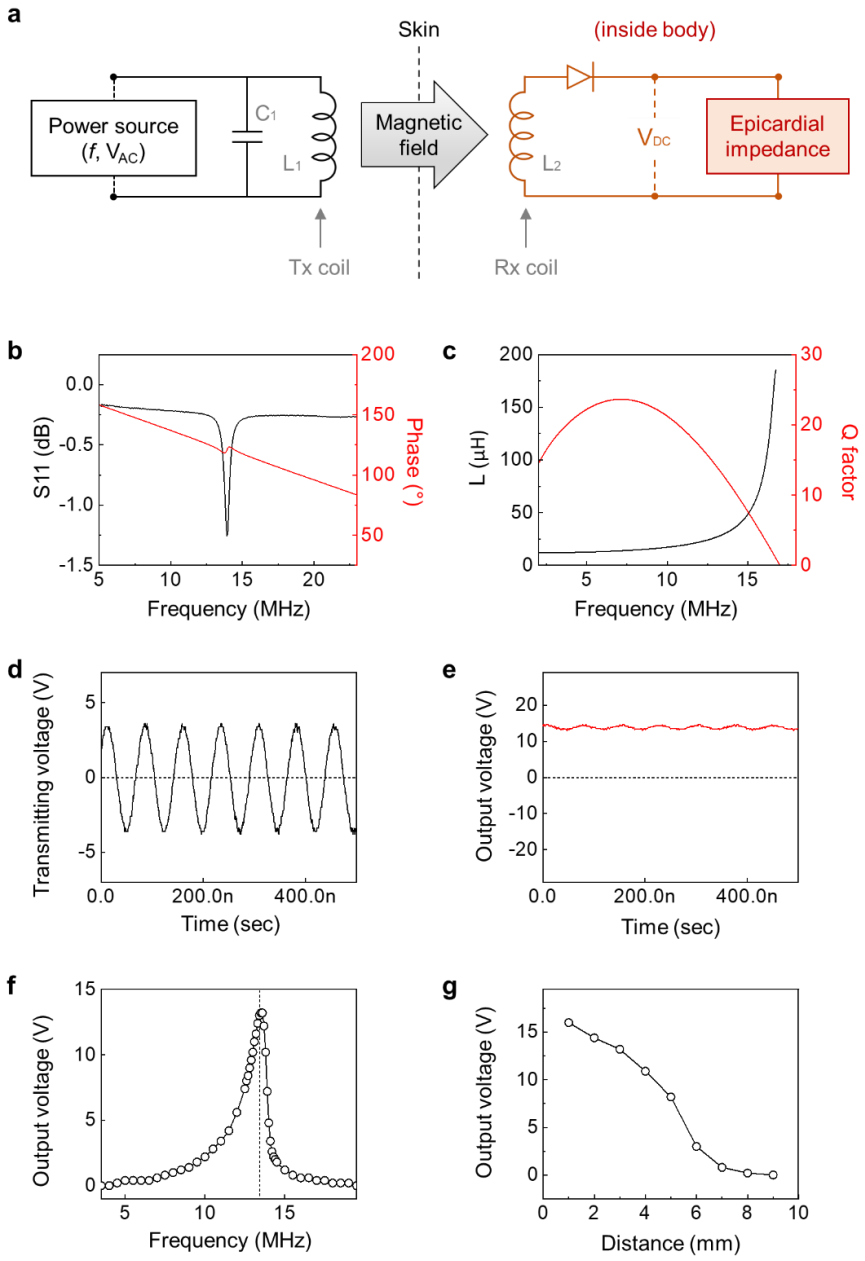

Figure 2.3.

Electrical performance characteristics of the wireless power transfer system. (A) Schematic illustration of the circuit diagram for the transmission of RF power at ~13.5 MHz. (B) Measured RF behavior of the stimulator (black, S_{11}; red, phase). (C) Simulation results for inductance (L) and Q factor as a function of frequency. (D) An alternating current (sine wave) applied to the Tx coil. (E) Example direct current output of ~13.2 V wirelessly generated via the Rx coil of the bioresorbable device. (F) Output voltage as a function of transmitting frequency. (G) Output voltage as a function of the distance between the Tx and Rx coils (transmitting voltage = 10 Vpp; transmitting frequency = ~13.5 MHz).

Figure 2.4A and Figure 2.4B shows the simulated scattering parameters (S_{11}) and Q factors of the wireless power harvesting units with four different sizes of Rx coils: 25 (blue), 18 (red), 12 (black), and 8 mm (green). Figure 2.4C shows that the largest coil (25 mm) generates much higher output voltage (~14.8 V) than the smallest (8 mm) coils (~2.12 V) at the same input voltage of 10 V_{pp} and load resistance of 5 kΩ, as expected with scaling with the area defined by the coil. The results in Figure 2.4D show that increasing the size of the Rx coil increases energy transfer efficiency. The design of the Tx coil is also important for enhancing wireless power transfer and shown by the in vitro testing set up in Figure 2.5. The energy transfer capabilities of the bioresorbable pacemaker system with various Tx coils: (i) Tx coil I (solenoid type; 3 turns; 12 mm diameter); (ii) Tx coil II (solenoid type; 4 turns; 100 mm diameter); Tx coil III (square; 1 turn; 260 × 280 mm^2) was studied to identify the optimal Tx-Rx match at large distances as shown in Figure 2.5B. Slices of pork with thicknesses between 20 and 120 mm, including skin, fat, bone, and lean meat, served as a mock compound inserted between the Tx coil and the device in Figure 2.5C and 2.5D. From experiments, the Tx coil I can deliver a power of 13.5 mW (input power = 12 W; resonance frequency = 13.56 MHz; load resistance = 5 kΩ) at up to 6 cm. In contrast, Tx coil III can deliver much higher power (32.8 mW) at much larger distances (up to 20 cm) in otherwise similar testing conditions. These results in Figure 2.5E, 2.5F, and 2.5G indicate that this system can support long-range operation in cardiac pacing. Considering that the distance between the implanted Rx coil and the surface of the skin around 3 cm, the maximum distance between Rx and Tx coils can be 20 cm. Taken together, these results show in Figure 2.4 and Figure 2.5 that the Rx to Tx coil distance and design of the Tx coil impact the parameters for optimal power transfer. In consideration of the translation of these results for patients, these parameters can be selected to

tailor to clinical case needs for optimal power transfer at the minimum transmitting voltages.

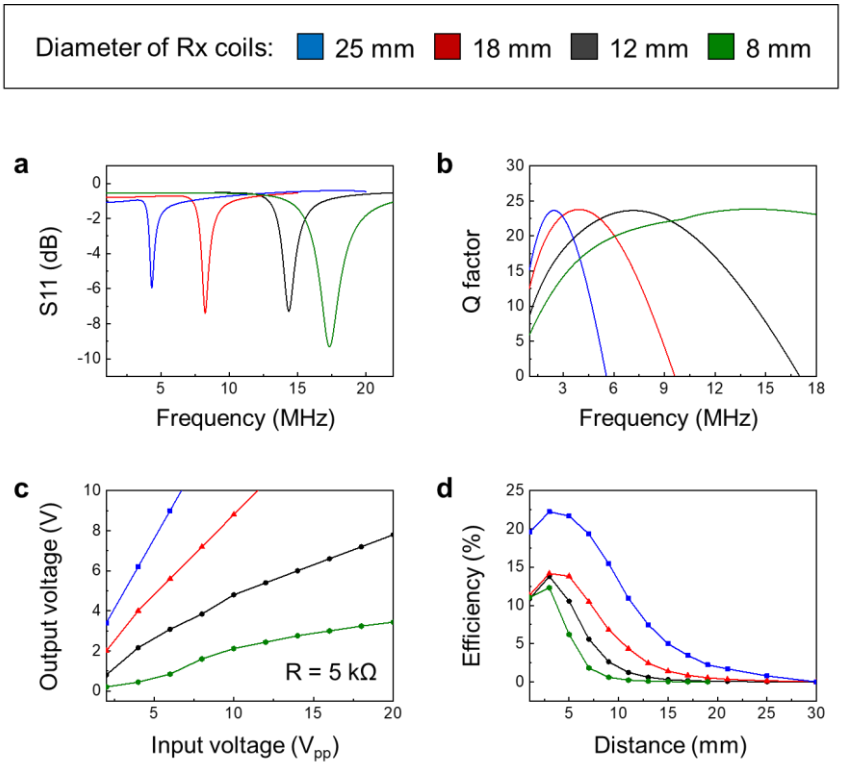

Figure 2.4.

Electromagnetic characteristics of bioresorbable, leadless cardiac pacemakers with various sizes of wireless power harvesting units. The sizes of the Rx coils are 25 (blue), 18 (red), 12 (black), and 8 mm (green). (A) Simulated scattering parameters (S_{11}) of the wireless power harvesting units with different sizes of receiver coils. The resonance frequency of each coil is 4.24, 8.03, 13.91, 17.33 MHz, respectively. (B) Simulated Q factors of the wireless power harvesting units, respectively. (C) Experimental results for the output voltage as a function of input voltage at a coil-to-coil distance of ~1 mm and load resistance of 5 kΩ. (D) Simulated power transfer efficiency as a function of changes in coil-to-coil distance.

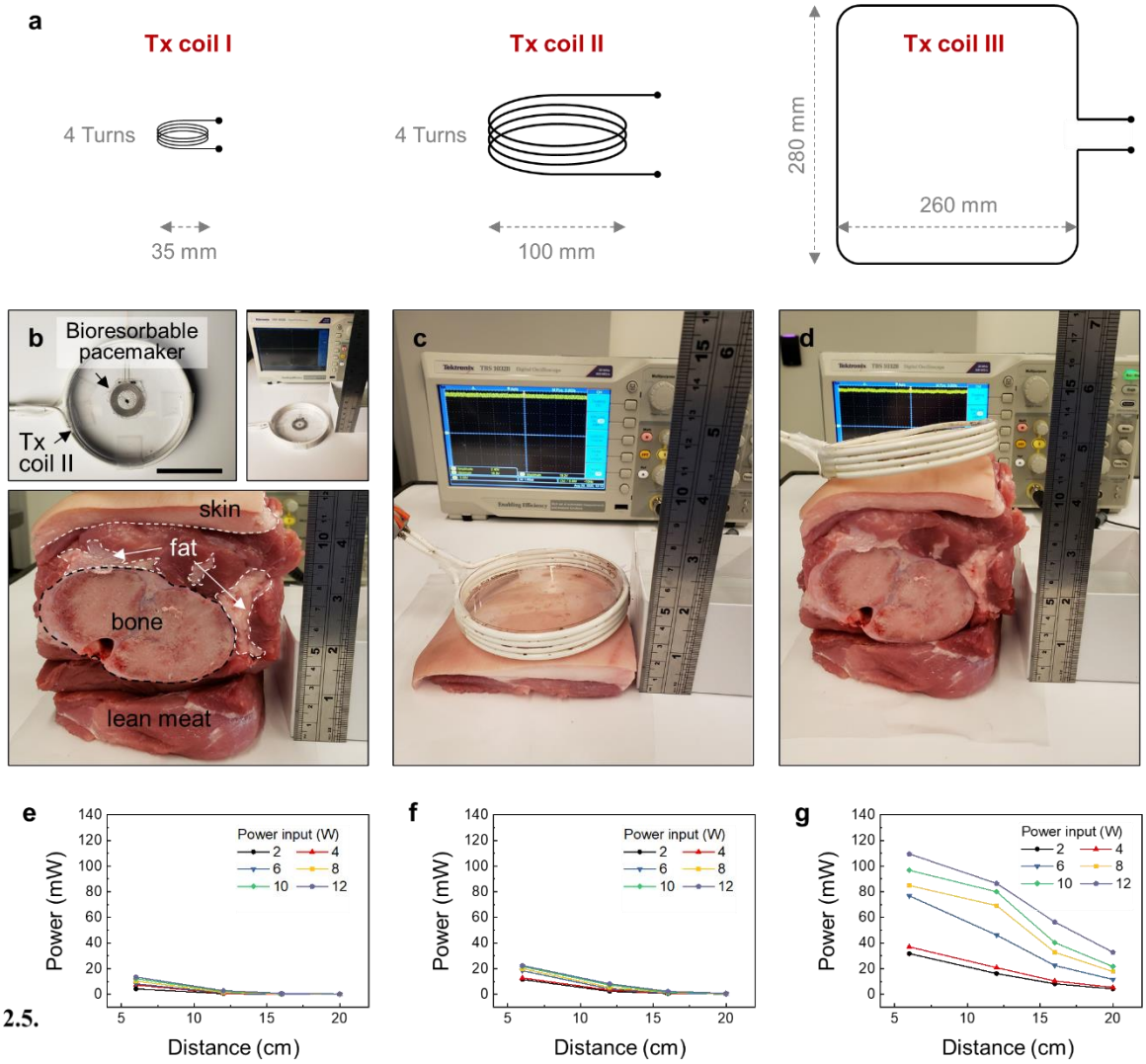

Figure 2.5.

Long-range wireless operation in vitro test of a bioresorbable cardiac pacemaker system. (A) Schematic illustrations of three different designs of Tx coil: (i) Tx coil I (solenoid type; 4 turns; 35 mm diameter); (ii) Tx coil II (solenoid type; 4 turns; 100mm diameter); Tx coil III (square; 1 turn; 260 × 280 mm2). (B) Photograph of bioresorbable pacemaker (diameter of Rx coil = 25 mm) and Tx coil II. Scale bar, 50 mm. (C) Wireless energy transfer through slices of pork with thicknesses of 20 mm. (D) Wireless energy transfer through slices of pork with thicknesses of 120 mm. Changes in output power of the bioresorbable pacemaker as a function of coil-to-coil distance (input frequency = 13.56 MHz; Input power = 2-12 W; load resistance = 5000 Ω): (E) Tx coil I; (F) Tx coil II; (G) Tx coil III.

2.5. Electric Field Distribution in the Heart Tissue

Finite element analysis was implemented on the commercial software COMSOL 5.2a by using the electrical current module (AC/DC Module User's Guide) to determine the electric field distribution in the heart tissue for voltages applied to magnesium electrodes with thicknesses of 50 μm. The partial differential equation for the current is

$$\nabla \cdot \boldsymbol{J} = Q_j \tag{2.1}$$

where Q_j is the current source and $\boldsymbol{J}$ is the current defined as $\boldsymbol{J} = \sigma \boldsymbol{E}$. The electric field is given by $\boldsymbol{E} = -\nabla V$, where σ is the electric conductivity and V is the electric potential in the electrode pads. The effective volume, i.e., volume with an electric field > 100 mV/mm shown in Figure 2.6, was determined from a triple integral (volume integration) over the heart tissue in the parametric study for electrode spacing (0.1–5 mm) and applied voltage (0.5–2.5V). The simulations reveal electric field distributions near the electrode–myocardium interface following electrical stimulation (electrode spacing, 2 mm; applied voltage, 0.75 V) in three-dimensional (3D) in Figure 2.6A and two-dimensional (x, z axes) space in Figure 2.6B. The results show that this bipolar electrode design induces a strong electric field in cardiac tissue and that different transmitting voltages and interelectrode distances influence the range—and therefore strength—of the electric field delivered by the pacemaker in Figure 2.6C. The electrode pads and heart tissue were modeled using 4-node tetrahedral elements. Convergence tests of the mesh size were performed to ensure accuracy. The total number of elements in the models was approximately ~400,000. The material properties used in the simulation for magnesium were ε_{Mg} = 1, σ_{Mg} = 2.25 × 10^7 S/m, and for the heart tissue ε_{heart} = 8 × 10^6, σ_{heart} = 0.1 S/m [71-73].

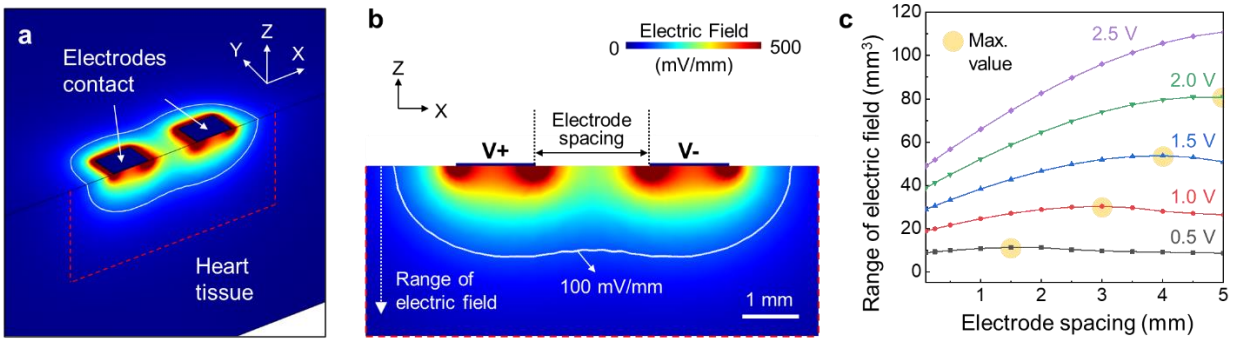

Figure 2.6. Computational results for distributions of the electric field within the cardiac tissue and relationships to design parameters associated with the contact electrodes in (A) three-dimensional (3D) and (B) two-dimensional (2D; x, z-axis) space, respectively. (C) Simulated range of electric field at electric field of 100 mV/mm as a function of electrode spacing with different input voltage (black, 0.5 V; red, 1.0 V; blue, 1.5 V; green, 2.0 V; violet, 2.5 V).

2.6. Simulation of the Mechanical Characteristics of the Device

Commercial FEA software (ABAQUS, Analysis User's Manual 2016) was used to study the mechanical behaviors of the flexible Mg electrodes after deformations of physiological relevance, i.e., those associated with the surface of the heart. The electrode can experience up to ~20% compression before the strain in the metal layer reaches the yield strain (0.6%) and initiates plastic deformation as shown in Figure 2.7. The PLGA was modeled by hexahedron elements (C3D8R) while the thin Mg layer (50 μm thick) was modeled by shell elements (S4R). The minimal element size was 1/8th of the width of the Mg wires (300 μm), which ensured the convergence of the mesh, and the accuracy of the simulation results. The elastic modulus (E) and Poisson's ratio (ν) used in the analysis were E_{Mg} = 45 GPa, ν_{Mo} = 0.35, E_{PLGA} = 16 MPa, ν_{PLGA} = 0.5. Optimized mechanical layouts ensure conformal contact against the curved surface of the heart for effective and reliable pacing. The simulation reveals distributions of principal strain for compression-induced buckling

perpendicular to the length of the interconnects, as shown in Figure 2.7A. Based on the layouts and the mechanical moduli, the maximum strains in the Mg electrodes and PLGA encapsulation are <0.6% for a compression of 20%, corresponding to the linear elastic regime for each of these materials. Images of the device during twisting (180°) and bending (bend radius, 4 mm) highlight additional features of the flexible mechanics as shown in Figure 2.7B. Wireless electrical measurements before and after twisting, compressing (that is, buckling) and bending show negligible differences in output voltage, consistent with expectations based both on FEA and analytical modeling results in Figure 2.7C. For different device layouts, (i.e., stretchable interconnects) the mechanical analysis reveals the elastic limits for stretching, twisting, and bending type deformations as shown in Figure 2.8 where the FEA reveals that the maximum strains in the electrodes are less than 0.6% for stretching (26%), twisting (612°), and bending (60%) to accommodate deformations for both continuous operation in the surface of the hearth and surgical insertion.

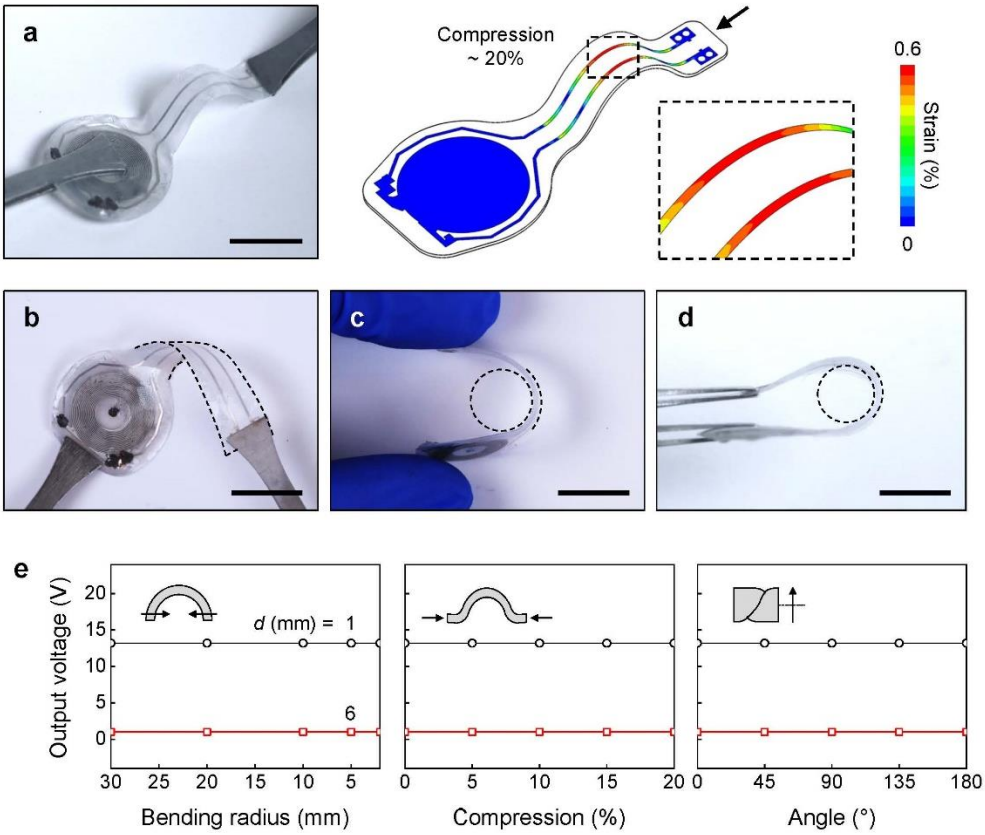

Figure 2.7.

Modeling and experimental studies of mechanical reliability of the bioresorbable, leadless cardiac pacemaker. (A) Photograph (left) and FEA (right) results for devices during compressive buckling (20%). (B) Photograph of twisted by 180°, (C) and (D) bent (bend radius = 4 mm) devices. (E) Output voltage of a device as a function of bending radius (left), compression (middle), and twist angle (right) at different distances between the Rx and Tx coils (black, 1 mm; red 6 mm). (n = 3 independent samples). Scale bar, 10 mm.

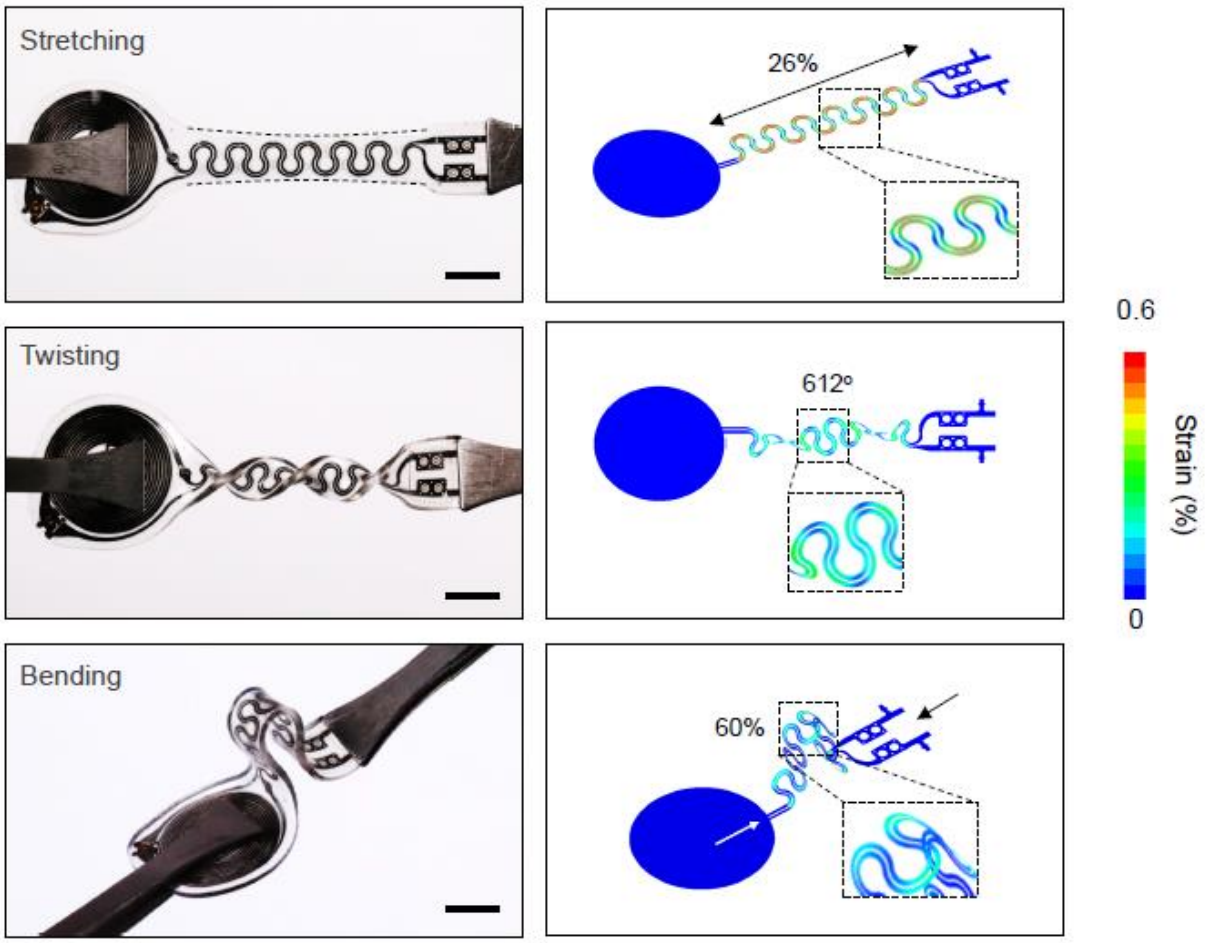

Figu

Modeling and experimental studies of mechanical reliability for stretching, twisting, bending mechanical deformations. Finite element analysis (FEA) reveals the distributions of principal strain for compression-induced buckling perpendicular to the lengths of the interconnects. (Left) Photographs of a bioresorbable module with b-DCPU-encapsulated serpentine electrodes during uniaxial stretching, twisting, and bending. Scale bar indicates 10 mm. (Right) Corresponding three-dimensional FEA results. FEA reveals that the maximum strains in the Mo electrodes and encapsulation are less than 0.6% for stretching (26%), twisting (612°), and bending (60%).

Simulation of the Electromagnetic Characteristics of the Device

2.7. The commercial software package ANSYS HFSS (ANSYS) was used to perform electromagnetic (EM) finite element analysis to 1) determine the inductance, Q factor, and scattering parameters $S_{11,}$ and S_{21} of bioresorbable, implantable double layer Rx coils with outer diameters of 8 mm, 12 mm, 18 mm, and 25 mm and its corresponding matching Tx coil of the same diameter and 2) quantify the influence of Rx and Tx coil size on the power transfer efficiency and output voltage. The receiver coils with 8 mm, 12 mm, 18mm, and 25 mm outer diameter are tuned to operate at a resonant frequency *f* of 17.3 MHz, 13.91 MHz, 8.03 MHz, and 4.24 MHz respectively, where the Q factor is maximum as shown in Figure 2.4. Lumped ports were used to obtain the scattering parameters S_{nm} and port impedances Z_{nm} of both the Rx and Tx coils. An adaptive mesh (tetrahedron elements) and a spherical radiation boundary (radius 1000 mm) were adopted to ensure computational accuracy. The inductance (L) and Q factor (Q) were obtained for all coils as $L_n = Im\{Z_{nn}\}/(2\pi f)$ and $Q_n = |Im\{Z_{nn}\}/Re\{Z_{nn}\}|$, where $Re\{Z_{nn}\}$, $Im\{Z_{nn}\}$, and f represent the real and imaginary parts of Z_{nm}, and the working frequency, respectively. The power transfer efficiency η is related to the magnitude of the scattering parameter S_{21} as [74]

$$\eta = |S_{21}|^2 \text{ x } 100\% \tag{2.2}$$

and the output voltage V can be calculated as

$$V = \frac{S_{21}\, V_s}{2} \sqrt{\frac{R_L}{R_S}} \tag{2.3}$$

where V_s and R_S are the input voltage and resistance at the source and R_L is the resistance of the load in the Rx coil. The relationship between power transfer efficiency and working distance was calculated for a separation of 1-30 mm between the Rx and Tx coil in all four scenarios; similarly, the relationship between output voltage/power and working distance was obtained in Figure 2.4. The dielectric constant (ε), and electrical conductivity (σ) used in the model are ε_{Mg} = 1, σ_{Mg} = 2.25 × 10^7 S/m, for the Mg coil trances in the Rx coils; ε_{Cu} = 1, σ_{Cu} = 5.8 × 10^7 S/m, δ_{Cu} = 0 for the Cu traces in the Tx coils. Lastly, the specific absorption rate (SAR), a measure of RF energy absorption in the body, was calculated for a mouse, with a 25 mm diameter Rx implant, in a plastic cage with a double loop Cu wire (AWG 12) Tx antenna operating at 13.56 MHz, as shown in Figure 2.9A. For long-term pacing in small animals, a double loop Tx coil (AWG 12) generated a uniform magnetic field inside a 26 cm, 47 cm, 21 cm (W, L, H) where a simplified mouse mesh ellipsoid body with major (half) axes 8, 14, and 52 mm included the implantable the bioresorbable module and the SAR was calculated on the mouse body. Longer-term studies in this in vivo rat model highlight the efficacy of the stretchable design of the bioresorbable module and its steroid eluting system at the tissue-electrode interface. In these experiments, a cage-based RF powering system with Tx loop coil provides wireless operation within a region of interest in Figure 2.9. The simplified mouse mesh ellipsoid body with major (half) axes 8, 14, and 52 mm as shown in Figure 2.9B was used to demonstrate that the SAR is well below the safety guidelines of RF exposure

[68]. The dielectric constant (ε), electrical conductivity (σ) and density (ρ) used in the mouse model are ε_{Mouse} = 40, σ_{Mouse} = 0.5 S/m, $\rho_{Mouse} = 1000$ kg/m^3.

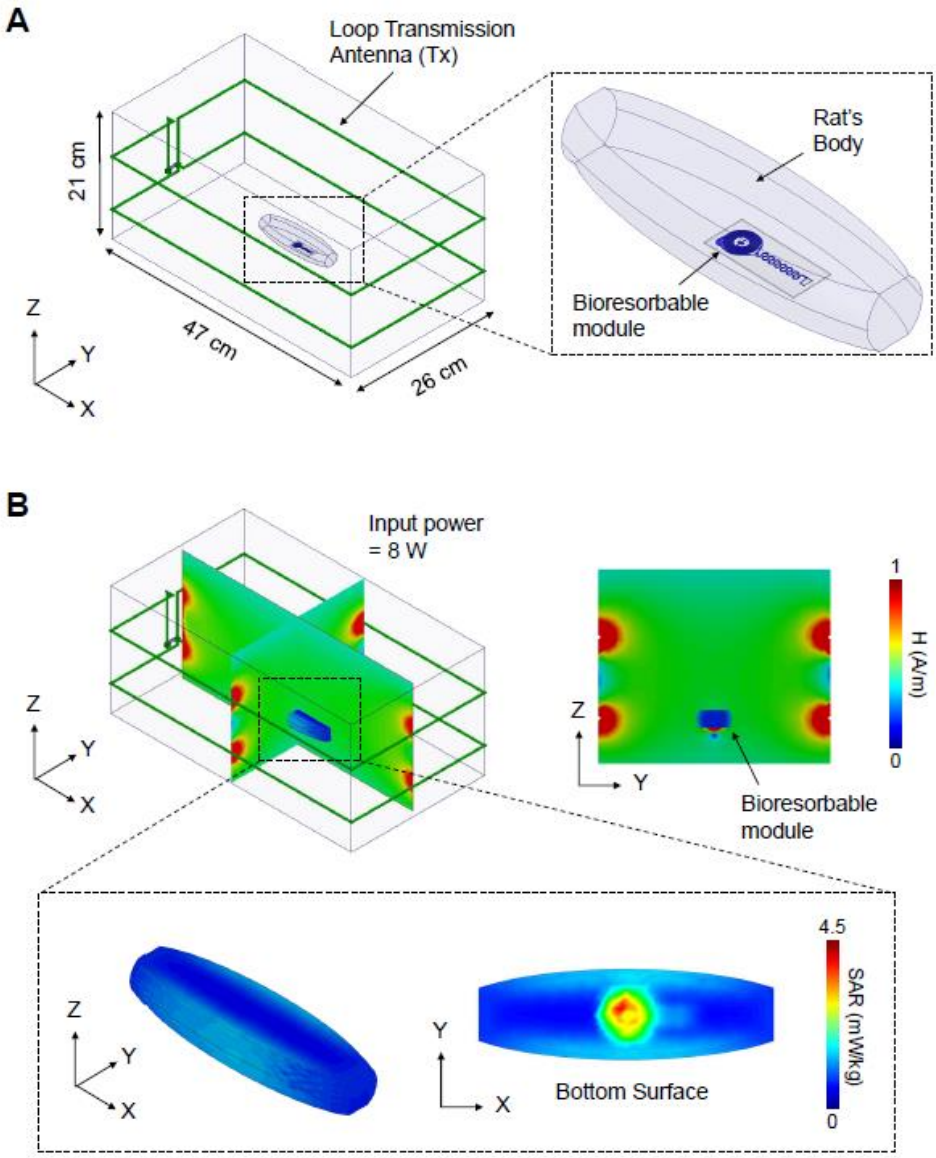

Figure 2.9.

Results of simulation of the distribution of the electromagnetic field. (A) Magnetic field distribution inside the cage at a cross sectional plane that intersects a simple model of a mouse. (B) Simulated specific absorption rate (SAR; a measure of the rate at which RF energy is absorbed by the body) as a function of position across a mesh model of a mouse body. (top) 3D and (bottom) 2D (x,y-axis) view of the mouse model.

The wireless power transfer was modeled in air and on the heart to account for dielectric effects. For the tissue model, the 25 mm coil was placed at the interface of skin/heart tissues of

dimensions 9 cm, 13 cm, and 8.5 cm (W,L,H) to approximate the size of a human adult heart as shown in Figure 2.10 and the average SAR was calculated as $SAR = \frac{\sigma|E|^2}{2\rho}$, where σ is the conductivity of the tissue, E is the root mean square of induced electric field and ρ is tissue density. For continuous pacing, an external coil with dimensions 15 cm × 20 cm with an input power of 1W was placed directly above the skin layer. Electromagnetic characteristics for inductive coupling between Rx coil in the bioresorbable module and Tx coil in the skin-interfaced cardiac modules are demonstrated in Figure 2.10A. The results of these computational works verify that operation of the transient closed-loop system and their wireless power transmission falls within guidelines outlined by the FCC (47 CFR Part 1.1310 and 15) and the FDA in Figure 2.10B. For all cases, an adaptive mesh (tetrahedron elements) and a spherical radiation boundary (radius 1000 mm) were adopted to ensure computational accuracy. The HFSS material library properties were used for the Mo and Cu conductors in the bioresorbable module, skin-interfaced module, cage coil, and external tethered coil. For biological tissues, the dielectric constant (ε), electrical conductivity (σ) and density (ρ) are: ε_{Skin} = 295, σ_{Skin} = 0.23 S/m, and $\rho_{Skin} = 1020$ kg/m^3 for the skin layer; ε_{Heart} = 246, σ_{Heart} = 0.53 S/m, and $\rho_{Heart} = 1055$ kg/m^3 for the heart tissue.

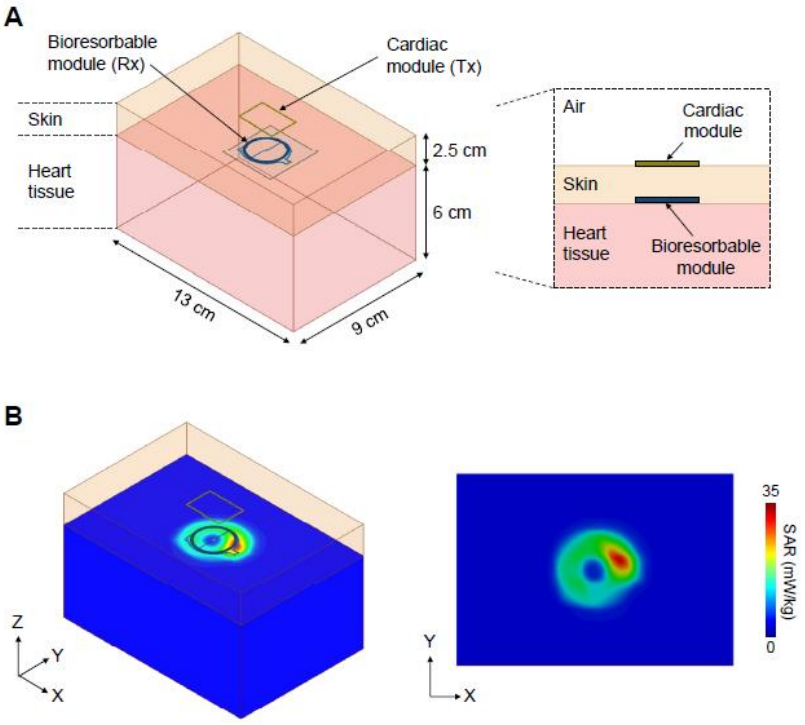

Figure 2.10. Electromagnetic characteristics of the transient closed-loop system in an in vivo human heart model. (A) Dimensions for electromagnetic simulation. The Rx coil (25 mm diameter) of the bioresorbable module is placed in a subcutaneous pocket, and the Tx coil of the skin-interfaced module is positioned on the skin aligned to the Rx coil. (B) Simulated specific absorption rate (SAR; a measure of the rate at which RF energy is absorbed by the body) at an input power (Tx coil) of 1 W.

2.8.

Summary and Outlook

The transient platform reported in this chapter presents a class of wireless technology that allows closed-loop modulation of heart rate over a timeframe that matches post-operative needs through coordinated operation of a networked collection of temporary, skin-interfaced modules and a bioresorbable electronic implant in communication with a control platform. Data captured from various locations of the body yields detailed information of patient status, across various aspects

of cardiopulmonary health. The results define autonomous rate-adaptive pacing parameters to match metabolic demand via wireless powering of the bioresorbable module; they also support feedback on device and physiological status via a programmable multi-haptic interface. In the simplest case, the system automatically recognizes bradycardia by algorithmic detection and then conditionally delivers appropriate cardiac pacing and haptic alerts to the patient. Information across all of the modules can be exploited for advanced versions of this basic scheme. Operation is possible over extended periods to match clinical needs, enabled by advanced mechanical designs and drug eluting configurations of the battery-free, bioresorbable pacemaker platform reported here. Replacement of the cardiac module can occur in a manner that does not disrupt continuous pacing. The skin-interfaced devices can be easily peeled away for removal after patient recovery, due to their soft, flexible construction.

CHAPTER 3

Mechanics of Vibrotactile Sensors for Applications in Skin-Interfaced Haptic Systems

3.1. Background

Vibration-based tactile displays offer various effective forms of information transfer through the skin [75]. Actuators for such purposes span those that rely on electromagnetic, electrostatic, piezoelectric, and pneumatic components and on shape memory alloys [75, 76]. Electromagnetic actuators are particularly attractive [77-80] due to their versatility in operating modality, simplicity in construction and convenience in use. Eccentric rotating mass (ERM) actuators and linear electromagnetic actuators are the two most common options. Devices of the former type use a direct current (DC) motor with an off-center mass adhered to the output shaft, all encased in a metal housing. Activation leads to large angular motions induced by centrifugal forces that result from the rotation of the mass. On the skin, the result is a three-dimensional dynamic motion that resembles that of a Euler's disk [77, 81], with vibrations that occur both in and out of the plane of the skin [82]. Although the forces generated by an ERM actuator can be significant, a disadvantage is that the torque and speed are coupled, such that the vibration amplitude and frequency cannot be controlled independently [81].

By comparison to ERM actuators, linear electromagnetic actuators offer a simple operating mechanism, based on voice coils and magnets suspended on springs. Similar to loudspeakers, harmonic motions of the magnet/spring follow from electromagnetic forces generated by passage of alternating current through the coil. Resulting vibrations occur linearly in a direction normal to the surface of the skin. Such actuators are available in two types, linear resonant actuators (LRAs) and vibrotactile linear actuators (e.g. tactors). For the former, the entire housing of the actuator interacts with the skin, as with an ERM device. The housing for the latter serves as a surrounding frame that restricts interaction with the skin through a comparatively small contactor. These

different designs and interactions with the skin lead to distinct dynamics [81, 83]. Unlike ERM actuators, LRAs and tactors operate on AC current, with independent control over both amplitude and frequency within a certain resonance bandwidth [76].

Tactile perception follows from the activity of low-threshold mechanoreceptors (LTMRs) that convert mechanical stimuli into action potentials in peripheral nerves [84]. Comprehensive mechanical analyses of the coupling between these LTMRs and skin-interfaced vibrotactile actuators can serve as design guidelines at the component and system levels in haptic devices. In this and other contexts, the methods for mounting the actuators onto the skin are critically important. For linear electromagnetic actuators, a surrounding frame can alter the inertial reference and contact area [81, 85-87]. Some investigations emphasize quantitative characterization of motions of the skin induced by vibrotactile actuators associated with tactile perception using accelerometers [88, 89]. Means by which stresses generated by the actuators propagate through the depths of various layers of skin remain unclear [84].

This work explores three-dimensional, spatio-temporal distributions of strain induced in skin phantoms both on their surfaces and into their depths by ERM actuators, LRAs and tactors using three-dimensional digital image correlation (3D-DIC) techniques and finite element analysis (FEA) methods. Investigations across different contact areas and at various depths relevant to the locations of mechanoreceptors with extensive perception tests provide insights into neurophysiological and psychophysical aspects

3.2.

Vibrotactile Sensors Experimental and Modeling Set Up

Figure 3.1A shows photographs of commonly used vibrotactile actuators for haptic devices,

including the ERM (Precision Microdrives^{TM} model No. 910-108.002 with the weight of 1.29 g and outer diameter of 10 mm), LRA (Precision Microdrives^{TM} model No. C10-100 with the weight of 1.37 g and outer diameter of 10 mm) and tactor (ATAC Tactor; weight=34.72 g; outer diameter = 30 mm) all designed with the same diameter of contact with the skin, $L_0 = 1$ cm. Figure 3.1B show photographs of additional components that allow various diameters of contact, L, with the skin and skin phantoms. Figure 3.1C presents a schematic illustration of mechanoreceptors and their distribution through the layers of the skin. Controlled studies use phantom skin structures that offer (i) moduli and bilayer structures that resemble human skin and (ii) optical transparency with embedded speckle patterns at two different depths. Figure 3.1D illustrate such a phantom made using pieces of polydimethylsiloxane (PDMS) formed with different thicknesses ($h_0 = 18$ mm; $h_2 = 2$ mm) and moduli ($E_1 = 419 \pm 0.9$ kPa; $E_2 = 68 \pm 1.3$ kPa). The depths of the speckle patterns correspond to $h_1 = 200$ μm and $h_2 = 2$ mm, as the approximate boundaries from the epidermis to dermis and dermis to hypodermis, respectively [90].

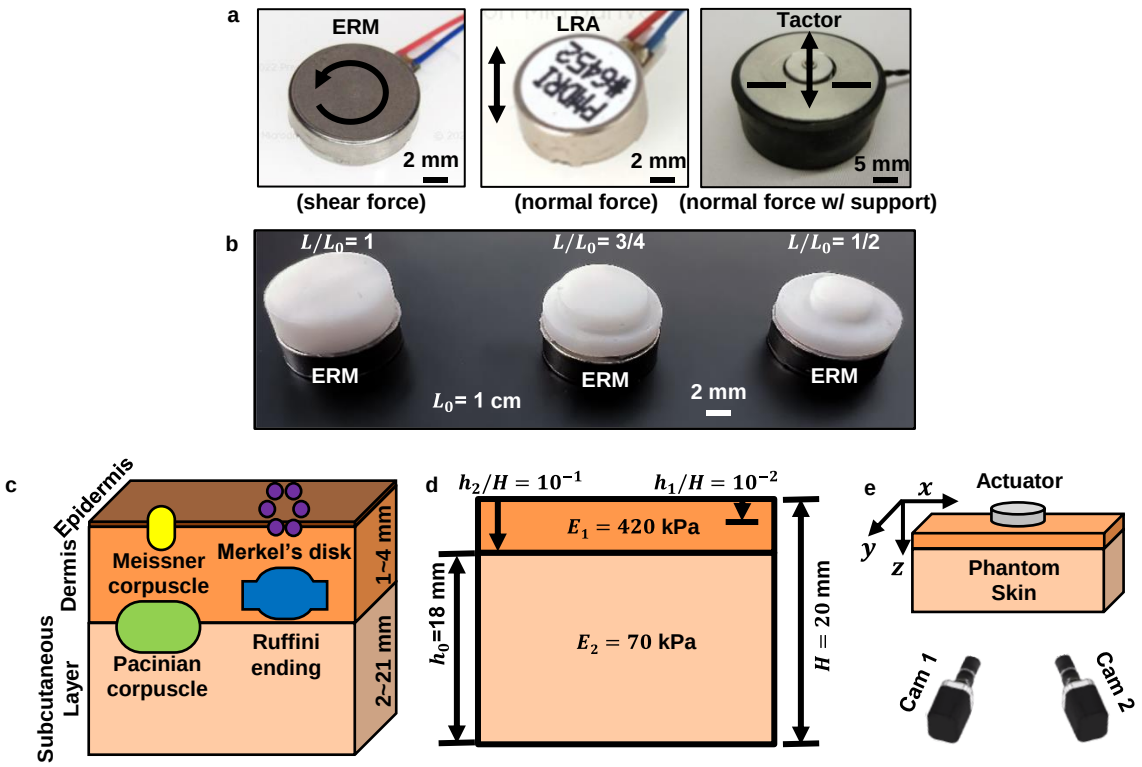

Figure 3.1. Vibrotactile sensors and experimental setup. (A) photographs of ERM, LRA and Tactor with shared contact diameters L_0 = 1 cm. (B) 3D printed parts for various contact diameters on top of ERMs. Schematic illustrations of (C) mechanoreceptors as well as skin layers, (D) a bilayer skin phantom used in FEA model, (E) 3D-DIC experiment setup.

A 3D model with dimensions of 100 mm × 100 mm × 20 mm (L × W × H) consisted of top and bottom layers with thicknesses of 2 mm and 18 mm, respectively, to match the experimental setup shown in Figure 3.1E. The displacement (U) and rotational (R) degrees of freedom were fixed for the element nodes at the skin edges. The element sizes were tested to ensure convergence and accuracy. The total number of elements (C3D8R) was ~125,000. A total time of 1×10-1 s was simulated for both devices with increments of 2.5×10-4 s. The instantaneous displacements and strain magnitude contours in Figure 3.2 show that the maximum in-plane displacements occur

directly underneath the ERM. The out-of-plane displacements show both positive and negative values at the edges. The magnitudes of the displacements gradually decrease with depth. Figure 3.3 shows results of similar simulations for the tactor. Unlike the ERM actuator, in this case the maximum in-plane displacements and strains occur at depths beneath the surface. The displacements contour in the in-plane directions shift from positive to negative with depth, due to the change in modulus of the PDMS materials used in the bilayer phantom. For tactor actuator, the maximum out-of-plane displacement occurs at the surface, but the maximum strain occurs at the interface between the top and bottom layers of the phantom, again due to the change in modulus. The elastic modulus (E), Poisson's ratio (υ), and density (ρ) used in the simulation are E_{skin} = 50 – 5000 kPa, υ_{skin} = 0.49, and ρ_{skin} = 1116 kg m^{-3} for the skin layers and E_{sensor} = 113 GPa and υ_{sensor} = 0.34, and ρ_{sensor} = 8005 kg m^{-3} for the vibrotactile sensors.

3.3. Mechanics of ERM Actuators

The coupled dynamics that exist between an ERM actuator and the skin lead to complex, large-amplitude motions and corresponding sensory perceptions that are stronger than those associated with LRA and other voice-coil-type actuators, excluding the tactor [77]. Numerical studies of the mechanisms for interfacing with viscoelastic materials as a function of depths relevant to the locations of mechanoreceptors are essential to decipher the key parameters that govern tactile sensations. The FEA models consist of an ERM actuator operated at the amplitude with three different contact areas, $L/L_0 = 1/2,\ 3/4$ and 1 at two depths, $h/H = 10^{-2}$ and 10^{-1}. Figure 3.2A and show the instantaneous displacements near the surface, h_1/H, during a representative instant of the ERM actuator operation. The dominant displacements lie along the x and y axes.

Significant out-of-plane displacements, Δz, also occur, with opposite directions at the opposing edges of the ERM actuator. The out-of-plane displacements are elongated along the binormal direction of the ERM actuator displacement vector. Displacements occur mainly in the vicinity of the actuator, particularly for the out-of-plane direction. Figure 3.2B show displacements evaluated at h_2/H. The in-plane displacements, Δx and Δy appear inverted relative to those at h_1/H, with two peaks near the edges of the contact area. At a representative instant, values for Δy include both positive and negative displacements in each quadrant, consistent with the Poisson effect. These results reveal that the in-plane displacements propagate into the depth as shown by the contour displacements and a representative schematic of the ERM operation in Figure 3.2C. As L/L_0 decreases, the rotational motion promotes a large amplitude in the oscillation of the actuator due to a similar degree of force applied to a small area. As L/L_0 decreases, the amplitude decreases and frequency increases, thereby affecting the dependence of the acceleration profiles on L/L_0. The shear wave velocity, c, evaluated for the case with $L/L_0 = 0$ at h_1/H is 8.25±0.5 m/s. The analytic equation for the shear velocity is $c = \sqrt{E/2(1+v)\rho}$, where $v = 0.5$ is Poisson's ratio and $\rho = 965$ kg/m^3 is the density of the artificial skin [91]. With a Young's modulus between E_2 and E_1, the value of c varies between 4.9 and 12 m/s, consistent with the experimental result. Profiles of Δx along the center line tangent to the displacement vector of the ERM actuator provide further indication that in-plane deformations transmit diagonally along the depth as shown by the left and center panels for h_1/H and h_2/H.

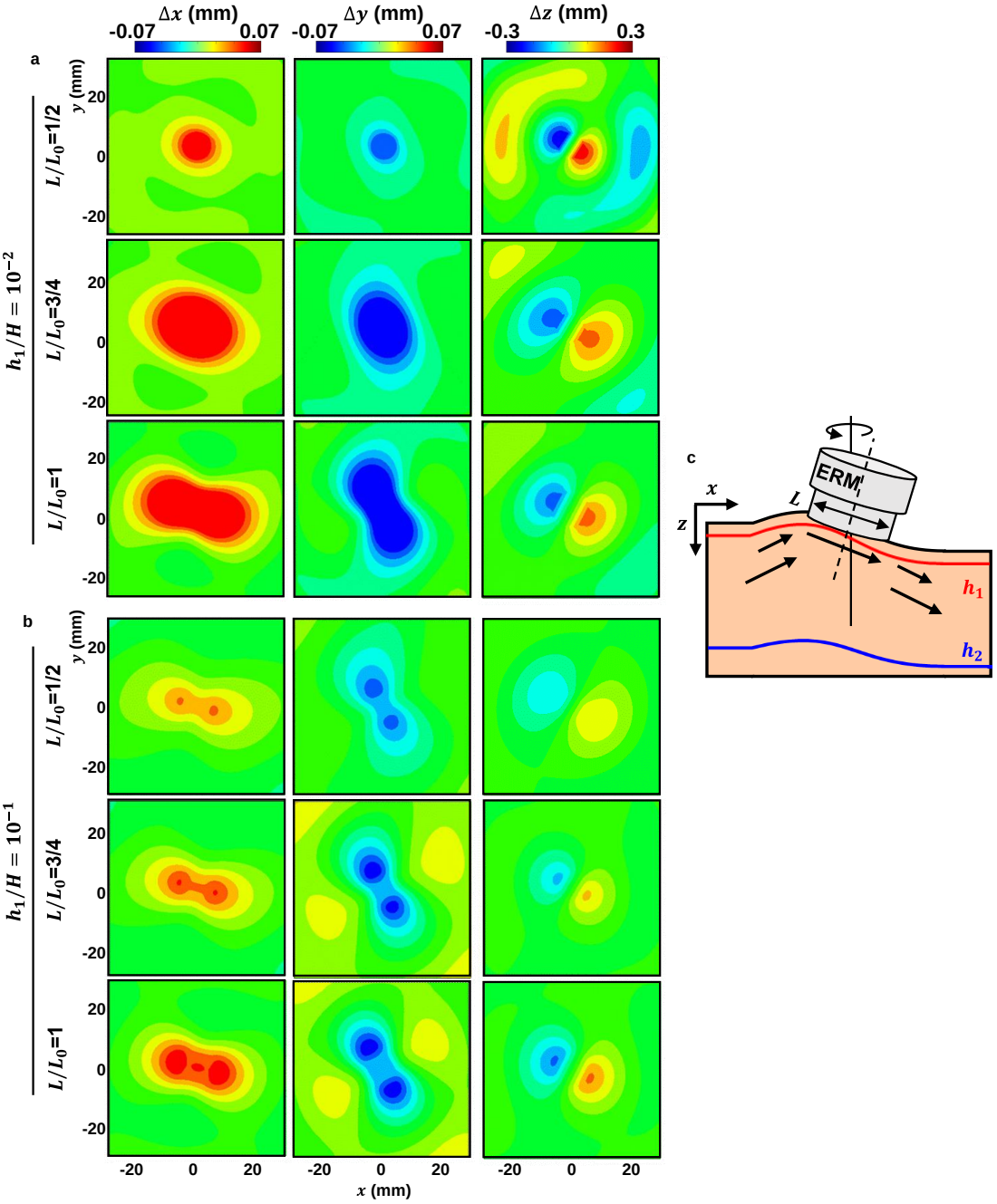

Figure 3.2.

Mechanics of ERM via FEA. Instantaneous displacement fields with L/L_0=1, 3/4, 1/2 at (A) 200 µm depth, $h_1/H = 10^{-2}$ and (B) 2 mm depth, $h_1/H = 10^{-1}$. (C) free-body diagram of an ERM actuator on the phantom skin.

3.4. Mechanics of Tactor Actuators

The support structure of the tactor, which surrounds the vibrating unit, responds to the reaction force induced by operation of the actuator. As a result, the tactor transmits vibrational motions straight down into the depth of the skin as shown in Figure 3.3. To allow fair comparisons to the results from the ERM actuators, the measurements involve (i) operation at a resonant frequency of 125 Hz, (ii) attachment of the vibrating unit to the skin phantom with double sided tape, (iii) fixation of the outer edge of the support structure (thickness of 5 mm) to the skin phantom to minimize inconsistencies associated with boundary conditions. As expected, the displacements occur mainly in the out of plane direction, along the z axis, with associated in plane displacements in opposite directions along the x and y axes, as shown in Figure 3.3A. The overall amplitudes are like those induced by the ERM actuator. The directions and magnitudes of the paired in-plane displacements change sign and increase, while those out of plane decrease, with depth, h_2 regardless of L/L_0 as shown in Figure 3.2B. Results of change in the direction of in-plane displacements indicate the presence of a body wave along the depth of the tissue. Unlike the case of an ERM actuator, the in-plane displacements increase at the interface of h_2 due to the transition of materials modulus at the location. The value of L/L_0 strongly influences the out of plane displacement, Δz, at the center of the actuator with respect to time. Specifically, Δz varies inversely with L/L_0, but the frequency is independent to L/L_0, as expected. The acceleration induced by the tactor is much greater, almost double, than that of the ERM actuator, for these commercial components. Profiles of Δz along the centerline further clarify the nature of the motions as the skin surface and deeper tissues as shown by the right panels in Figures 3.3A and Figure 3.3B.

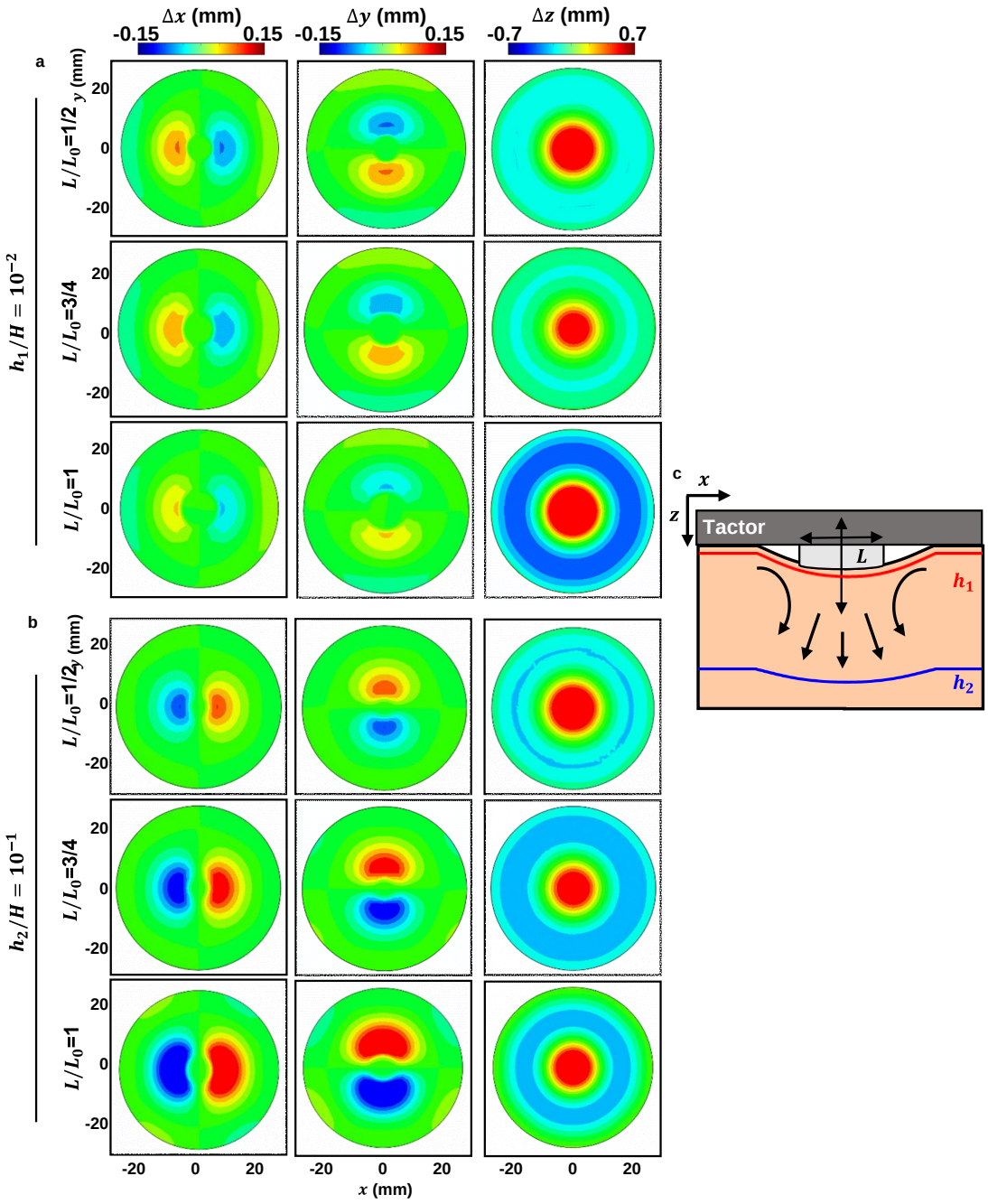

Figure 3.3.

Mechanics of Tactor via FEA. Instantaneous displacement fields with L/ L_0=1, 3/4, 1/2 at (A) 200 µm depth, $h_1/H = 10^{-2}$ and (B) 2 mm depth, $h_1/H = 10^{-1}$. (C) free-body diagram of an ERM actuator on the phantom skin.

Strain Characteristics

Strain directly connects to perception because mechanoreceptors act effectively as strain gauge sensors. The strain profiles for each actuator at different depths reveal distinctive characteristics.

3.5.

Strain fields induced by an ERM actuator exhibit high magnitudes around the border of the actuator near the surface of the skin. Those induced by the tactor reach maximum values at depths into the skin, following a parabolic profile as shown in Figure 3.4. As mentioned previously, the color range for the plots of the strain field of the tactor is twice that for the ERM, as with the range for displacements, due to their peak-to-zero and peak-to-peak oscillations, respectively.

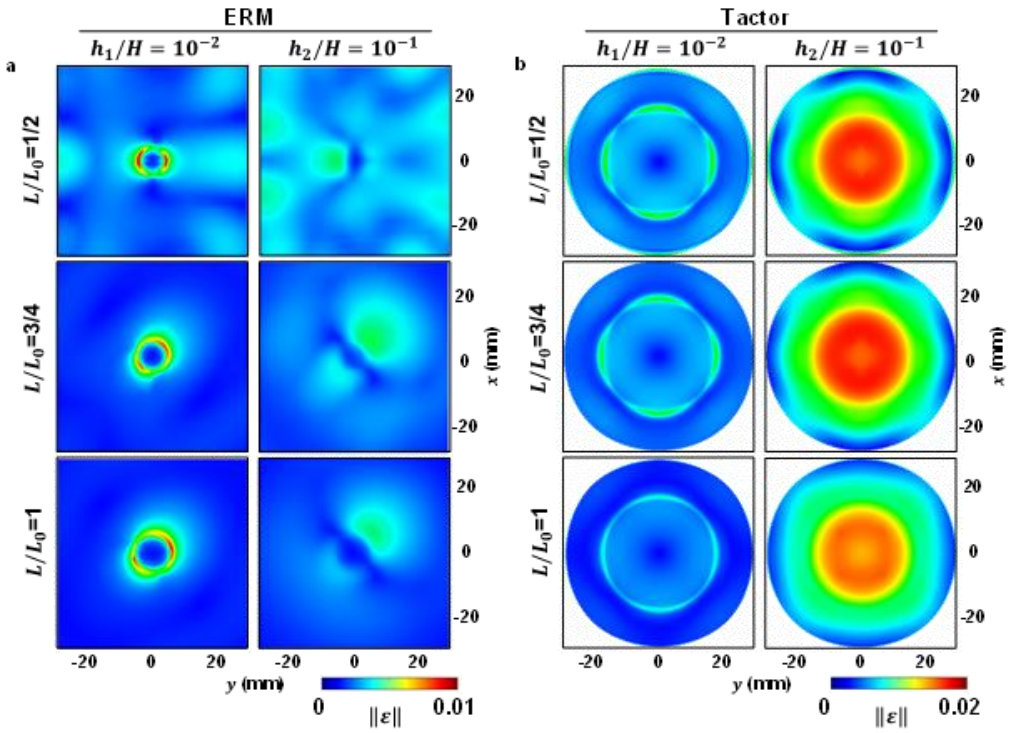

Figure 3.4. Distributions of strains induced in a skin phantom by operation of (A) ERM actuator and (B) tactor on its surface, evaluated by finite element analysis for various L/L_0 and h.

Near the surface, h_1, the peak strain by an ERM actuator exceeds that from the tactor. By contrast, the peak strain induced by the tactor occurs at depth, h_2, and exceeds the peak strain by

an ERM actuator at h_1 as shown by the column comparison in Figure 3.4A and Figure 3.4B. The magnitudes of the strains exhibit an inverse relationship to contact area, like the case of the displacements. The strain for the ERM near h_1 with $L/L_0 = 1/2$ in a temporal domain exhibits the largest amplitude with respect to h and L/L_0, like the characteristics of strain magnitude in the spatial domain. On the other hand, the frequency of oscillating strain changes over L/L_0 due to its actuation mechanism. This coupling between amplitude and frequency of vibration further affects corresponding values for strain rate. The amplitudes of strains induced by the tactor at h_2 are larger than those of the ERM actuator regardless of h and L, operating at a fixed frequency, as expected, and shown in Figure 3.4B.

3.6. Finite Element Modeling

These various effects can be captured using FEA. The focus is on instantaneous displacement and strain profiles for various L/L_0 and depths into the skin h/H, for comparison to 3D-DIC results. Further studies examine the effect of the modulus ratio E_1/E_2. The corresponding instantaneous displacements and strain magnitude contours are computed at time 10^{-1} s and plotted at $h = 10^{-1}$ mm and 10^{-2} mm as shown in Figure 3.5. For the ERM actuator, the simulations use an in-plane rotational force applied to the central axis of the actuator and out-of-plane forces at the opposite ends as shown in Figure 3.5A and Figure 3.5B. For the tactor, a compressive pressure with a fixed sinusoidal frequency acting on the top surface of the actuator creating the displacement and strain distributions shown in Figure 3.5C and Figure 3.5D The computed instantaneous displacements and strain magnitudes reproduce trends observed in the 3D-DIC experiments.

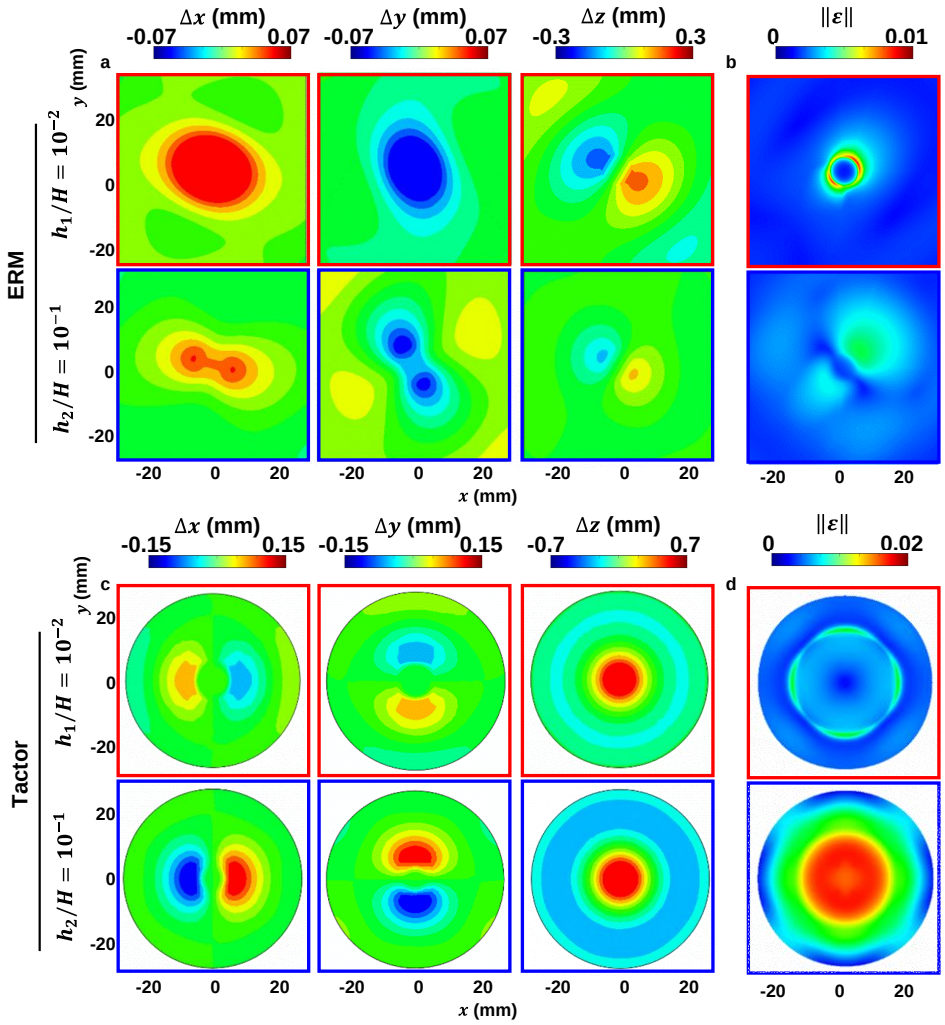

Figure 3.5. Finite Element Analysis of the Mechanics of ERM and Tactor. Instantaneous (A) displacement fields and (B) strain magnitude for a representative device ERM case. Instantaneous (C) displacement fields and (D) strain magnitude for a representative Tactor case. In both cases, the parameters are L/L_0= 3/4 at 200 μm depth (red border), $h_1/H = 10^{-2}$ and 2 mm depth (blue border), $h_1/H = 10^{-1}$.

Additional results reveal the effects of skin modulus in the amplitude and strain distribution, based on simulations that involve the modulus of the top layer from 50 – 500 kPa, corresponding to a ratio E_1/E_2 between 1 – 10, relevant to the range of skin properties [92], as shown in Figure 3.6. The computations yield the displacement amplitudes and strain magnitudes over a linear nodal

path in the x-axis that intersects the actuator, normalized by values at $E_1/E_2 = 1$. Figure 3.6A shows that the normalized in-plane amplitude for the ERM actuator and the normalized out-of-plane amplitude for the tactor both decrease with increasing E_1/E_2. Specifically, relative to $E_1/E_2 = 1$, at $E_1/E_2 = 10$, the amplitudes produced by the ERM actuator and tactor reduce by 62 % and 26%, respectively.

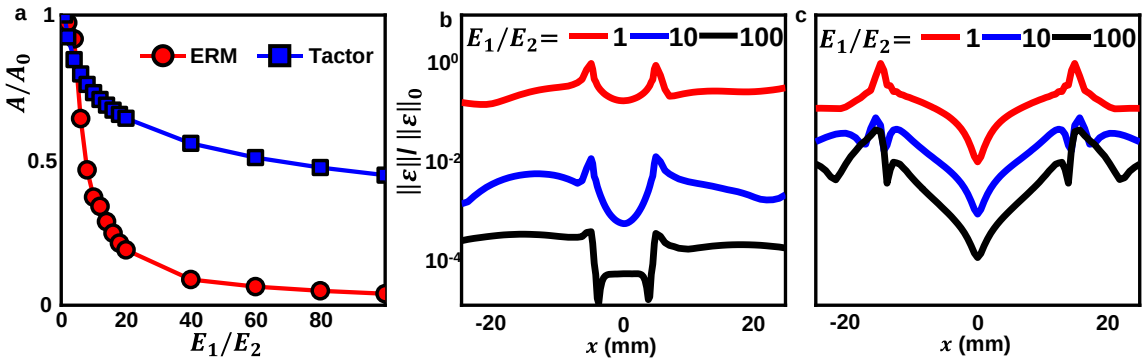

Figure 3.6. Finite Element Analysis of the Mechanics of ERM and Tactor. (A) Normalized amplitude of the ERM and Tactor devices as a function of the skin modulus ratio E_1/E_2. Normalized strain distribution for three cases of skin modulus ratio E_1/E_2= 1, 10, 100 over the path (x, y = 0) for (B) ERM and (C) Tactor.

These different trends are consistent with the surface and depth dominated interactions associated with the ERM actuator and tactor, respectively. Figure 3.6B shows that increasing the modulus ratio by one order of magnitude to $E_1/E_2 = 10$, the amplitudes of motions induced by the ERM actuator decrease by approximately two orders of magnitude and those induced by the tactor decrease by approximately one order of magnitude as shown in Figure 3.6C.

3.7. Summary and Outlook

The presented work investigates mechanical vibrations induced by three commercially available, representative vibrotactile sensors used in recent haptic applications. Mechanical vibrations of a bilayer skin-like material with various contact areas and along the depth, measured by 3D-DIC and validated by the FEA simulation, correlate with extensive perception tests. The results show that the tactor triggers sensations and produces strong perceptions at low power, but with performance that depends strongly on mounting method. On the other hand, the ERM actuator yields a strong sensation, with an efficient mounting strategy and a comparatively small, lightweight form factor. This type of actuator suffers, however, from a coupling between amplitude and frequency and a dependence on its operating environments that follow from corresponding changes in inertia. This work establishes a framework for comparison studies of performance related not only to actuator type but also actuator design features such as those related to coil geometries, magnet properties and overall layouts. A combination of various types of actuators may ultimately be needed for robust, engaging haptic sensations through programmed engagement of different types of mechanoreceptors.

CHAPTER 4

Mechanics of Holey Architectures for Skin-Integrated Devices in Physiological Monitoring Applications

Continuous monitoring of vital signs is an essential aspect of operations in neonatal and pediatric intensive care units (NICUs and PICUs), of particular importance to extremely premature and/or critically ill patients. Current approaches require multiple sensors taped to theskin and connected via hard-wired interfaces to external data acquisition electronics. The adhesives can cause iatrogenic injuries to fragile, underdeveloped skin and the wires can complicate even the most routine tasks in patient care. Recent work demonstrates the utility ofsoft, wireless sensors as an attractive alternative approach to monitoring, with equal or better performance compared to existing standards. This chapter introduces materials strategies and design concepts that significantly improve these platforms through the use of optimized materials, open (i.e. 'holey') layouts and pre-curved designs. These schemes (1) reduce the stresses that can occur at the skin interface, (2) facilitate release of interfacial moisture that can accumulatefrom transepidermal water loss, (3) allow visual inspection of the skin for rashes or other formsof irritation that can develop and, most importantly, (4) enable triggered reduction of adhesion to reduce the probability for injuries that can result from device removal after a period of use. A combination of systematic benchtop testing and computational modeling identifies the essential mechanisms and key considerations. Demonstrations on adult volunteers and on a neonate in an operating NICUs illustrate a broad range of capabilities in continuous, clinical- grade monitoring of

conventional vital signs and unconventional indicators of health status.

4.1. Background

Each year, more than 480,000 infants and children in the United States are admitted to intensive care units (ICUs). Those under one year of age, particularly very low-birth-weight premature infants, suffer from high rates of morbidity and mortality [93-95]. For these fragile patients, real-time monitoring of their vital signs represents an essential aspect of care. Traditional systems for such purposes in the neonatal and pediatric ICUs (NICUs and PICUs) involve multiple electrodes and sensors that attach to various parts of the body using adhesive tapes. Hard wires form interconnections to external electronic processing and storage units. These platforms can provide high quality data but they have significant disadvantages. For neonates and pediatric patients with immature skin, iatrogenic injuries and subsequent scarring can result from the electrodes/sensors and adhesives [96-98]. This hardware also frustrates natural movements, it creates practical difficulties in feeding, changing diapers and bathing, and it limits opportunities for physical bonding with parents through skin-to-skin contact (i.e., kangaroo care, KC) [95].

Soft, wireless electronic devices can overcome these and other drawbacks of traditional monitoring equipment, to enable safe and effective care for vulnerable patients [99-109]. Our group recently reported two such types of technologies and demonstrated their use in NICU and PICU facilities [110, 111]. The most advanced systems operate in a battery-free manner, through devices that have ultrathin, stretchable, ‘skin-like’ characteristics. A time-synchronized pair can capture heart rate (HR), heart rate variability (HRV), respiration rate (RR), blood oxygen saturation (SpO_2), pulse wave velocity and skin temperature at the chest and at a limb, all with clinical- grade levels of accuracy. The thin, low modulus properties and wireless

operation of these devices allow robust bonding to the skin with interfacial adhesives that require bonding strengths that are more than ten times less than those needed with conventional wired sensors, thereby reducing the probability for iatrogenic skin injuries during removal. Additional important features include sparse architectures that provide optical transparency, for visual inspection of the skin interface, and electromagnetic designs that allow use of magnetic resonance imaging and X-ray computed tomography, for various diagnostic purposes. A limitation of this technology is that the mechanical fragility of the devices leads to practical difficulties in multiple cycles of application, removal and sterilization, particularly relevant for use in the home or in lower- and middle-income countries. Also, the near-field communication (NFC) schemes for wireless power delivery and communication require reliable wall-plug power, RF transmission hardware and specialized electronics. Furthermore, the protocols can only support operating ranges and data transfer rates of up to 30 cm and a few hundred Hz, respectively. Related constraints prevent monitoring modalities that extend beyond the current clinical standard of care [110].

This chapter introduces concepts that address these disadvantages using optimized materials in open, or ‘holey’, device architectures and with pre-curved layouts. The holes, with strategic locations and dimensions defined by finite element analysis (FEA), enhance the flexibility and stretchability of the devices in various directions that are important to practical use. Perhaps more significantly, these features also provide multiple points of access for introducing warm water to the skin interface. The consequent swelling of hydrogel adhesives molded with microfluidic channel structures dramatically reduces the bonding strength, in some cases to negligible values, to facilitate device removal [112–114]. Additional aspects of this

design include (1) visual access to the underlying skin, for clinical inspection for irritation or allergic reactions, and (2) mechanisms for enhanced evaporation of water released through natural transepidermal mechanisms or sweating [115, 116]. Precurved shapes tailored to the match the surfaces of desired mounting locations minimize bending forces and corresponding stresses at the skin interface. Systematic studies of devices designed to monitor a full range of conventional and unconventional metrics of physiological health reveal all the key aspects of these advanced materials and design ideas.

4.2. Holey Platforms for Wireless Monitoring in NICU/PICU

Figure 4.1A presents schematic illustrations of a thin, soft wireless device with a holey architecture of the type described above. The electronics consist of a flexible printed circuit board (fPCB; total thickness 173 μm) that includes four layers of copper (Cu) and five layers of polyimide (PI) structured to include thin, narrow serpentine conductive traces (widths between 76 and 375 μm wide; thickness 18 μm) that interconnect a collection of chip-scale integrated components (lateral dimensions between 1 mm^2 and 64 mm^2; thicknesses between 0.5 mm and 1.5 mm). A small, rechargeable lithium-polymer battery (DNK201515; 15 mm X 15 mm; thickness 2 mm) supplies power for operation. As described in detail in subsequent sections through modeling, holes formed through the fPCB and the encapsulation structure reduce the effective modulus and bending rigidity to facilitate gentle application and removal from the skin. A wireless circuit uses an induction coil to charge the battery. A representative block diagram of the operational scheme of the device is shown in Figure 4.1B. The assembly and encapsulation process begins with folding of the fPCB islands at hinge points defined by serpentine

interconnects, to reduce the overall size of the device as shown in Figure 4.1A. The serpentines include four Cu layers, pre-compressed by 30% to enhance their flexibility and stretchability. FEA results indicate that the strain in each Cu layer remains below the fracture limit (~1%) throughout these steps as shown in Figure 4.2. After this assembly process, the serpentine interconnects can stretch along their lengthby up to 85% without inducing fractures in the Cu. The top and bottom layers of the encapsulation structure consist of a low modulus silicone material (5 MPa; Silbione RTV 4420) molded into the desired shapes. A silicone polymer with a different formulation (0.069 MPa; Ecoflex 00-30) injected in between these layers fills the empty spaces in a manner that maintains the softness of the overall platform and minimizes mechanical constraints on motions of the serpentine interconnects induced by bending or stretching. This material also prevents damage of the encapsulation layer by the rigid electronic components and entanglement of the serpentine interconnects. The photograph in Figure 4.1C shows a device with this construction mounted on the curved chest of a realistic neonate model, bonded to the surface with a hydrogel adhesive (KM 40A hydrogel, Katecho Inc.; thickness ~815 μm).

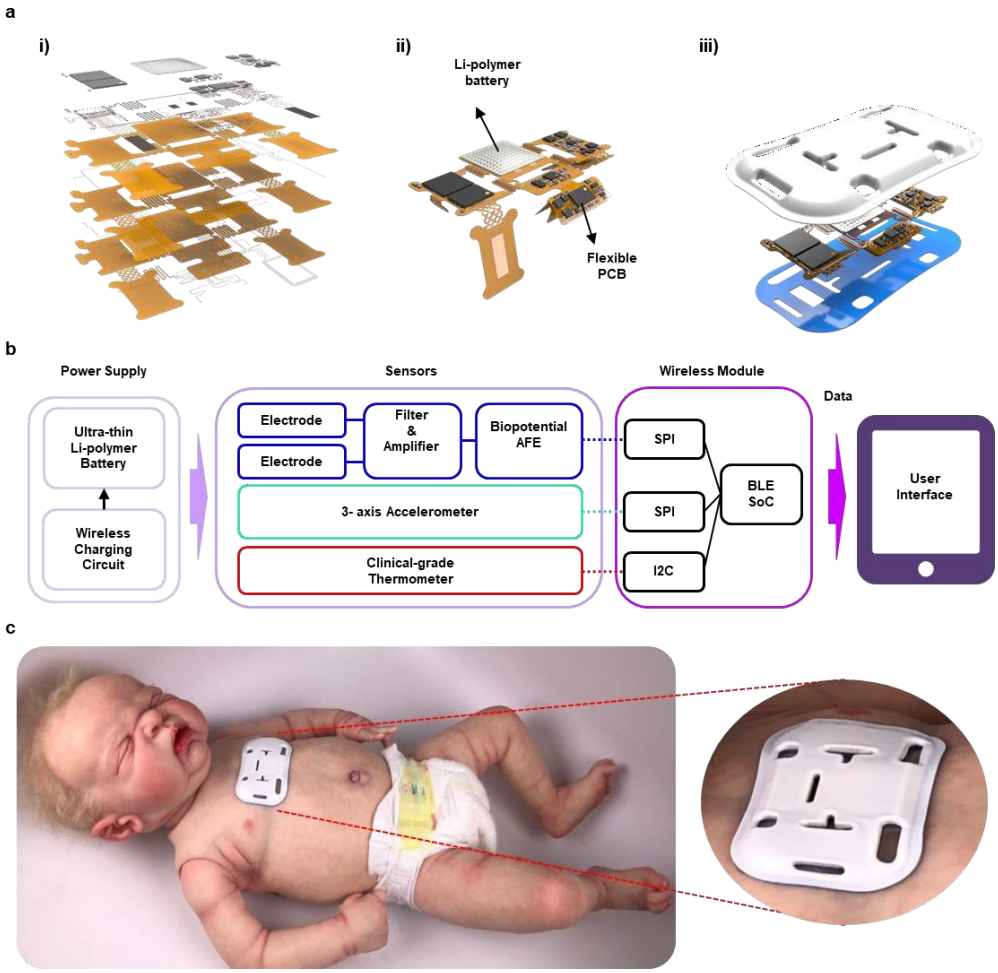

Figure 4.1. Schematic diagrams and images of a soft, holey wireless device for measuring electrocardiograms (ECGs) and skin temperature, and for capturing tri-axis accelerometry data. (A) Exploded view illustration of a device with a rechargeable battery showing the flexible printed circuit board supports circuit components on island structures, with serpentine filamentary interconnects configured for a folding process conducted prior to encapsulation. (B) Block diagram of the operational scheme of the device. (C) Images of a device on the chest of a realistic model of a neonate.

4.3.

Mechanics of Holey Design

Some holes reside near the serpentine interconnects to preserve their high flexibility and

stretchability; others lie inside the center island to facilitate deformations in this part of the device. Holes of various shapes near the border area promote low stiffness and modulus at locations where peeling initiates, to reduce skin irritation during device application and removal. Systematic studies by FEA define various advantages of this layout in effective modulus and bending stiffness, as well as in corresponding degrees of stretchability and bendability. The photographs in Figure 4.2 show the device bent along its long axis to a radius of 22 mm (left) and along the orthogonal direction to a radius of 5.3 mm (middle) and through a twisting angle of 125^{o} (right). The three main islands that support the IC chips and the battery include stiffeners of rigid printed circuit board material (Garolite G-10/FR-4, thickness 381 μm). These elements effectively eliminate bending in these areas, to avoid possible damage to the solder joints between the components and the fPCB. All system level deformations of the device involve motions of the serpentine interconnects, such that strains in the Cu ultimately limit the range ofstretchability and bendability. The maximum principal strains in the Cu layers remain below the yield strain of 0.3% (Figure 4.2B), for the cases examined here. Comparisons to standard (i.e., non-holey) devices with otherwise similar designs reveal that the presence of the holes reduces the strains across all functional materials by 34.4 % (bending), 28.8 % (orthogonal bending), 15.5 % (twisting), 14.1 % (stretching) for these cases (Figure 4.2C). Similar comparisons indicate that the holes decrease the stiffness and modulus by ~30% for parallel/horizontal bending, ~23% for twisting and ~20% for uniaxial stretching (Figure 4.2D). These features also lead to stresses at the interface (normal and shear) with the skin that remain below thresholds for sensory perception for adults (20 kPa) for uniaxial stretching of up to 20%, a value at the high end of the range expected in practical use as shown in Figure 4.3.

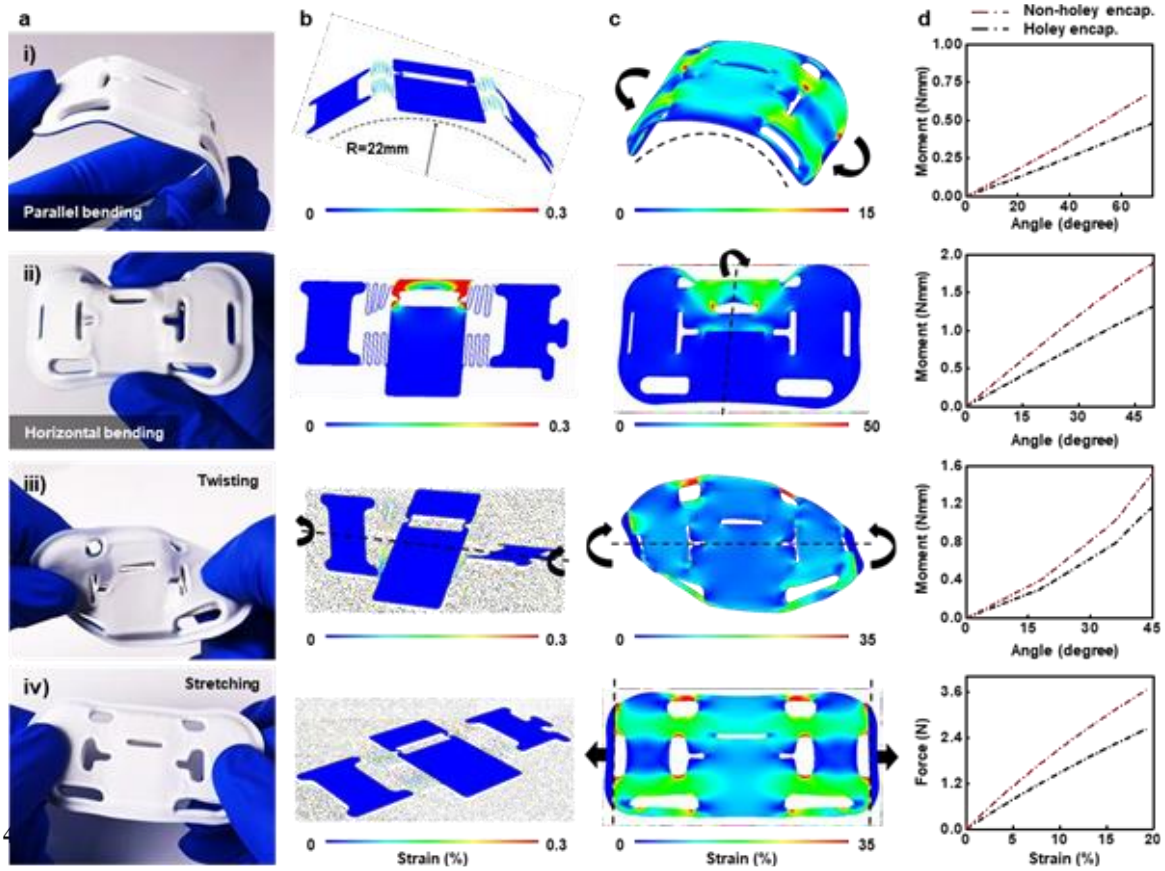

Figure 4 Mechanical characterization results and images of a soft, holey, wireless vital signs monitoring device under various mechanical deformations. (A) Images of a representative device during (i) parallel bending, (ii) horizontal bending, (iii) twisting and (iv) stretching. (B) Simulation results for the deformed geometries and strain distributions in the copper layer of the electronic system. (C) Simulation results for the deformed geometries and strain distributions in entire encapsulated device during corresponding deformations. (D) Comparisons of moment-angle and force-strain responses for holey and non-holey device designs.

The mechanical simulation of the device was performed in ABAQUS, a commercial finite element analysis software, was used to model the mechanical behavior of the serpentine

interconnects used for the electronics and the different encapsulation designs when subjected to different types of deformation (stretching, bending, and twisting). The objectives of the analysis were to 1) assess possibilities for plastic deformation (i.e., $\varepsilon < 0.3\%$) occurs in the copper serpentine interconnects when the device undergoes different types of external loads, 2) guide designs to reduce the magnitude of the strain in the optimized holey encapsulation, and 3) determine whether the interfacial normal and shear stresses imposed by the device onto the skin during deformation remain below the low somatosensory perception of the device on the skin for wearability, and 4) compare the resilience of the flat and pre-curved soft encapsulation designs associated with mounting on the curved surface of the skin. The thin copper (~12 μm thick) and PI (~25 μm thick) layers were modeled by composite shell elements (S4R), the soft encapsulation designs (with and without holes) were modeled by tetrahedron elements (C3D10), and the skin was modeled by hexahedron elements (C3D8R). The element size was tested to ensure convergence and accuracy of the simulation results. The elastic modulus (E) and Poisson's ratio (v) were E_{PI} = 2.5 GPa and v_{PI} = 0.34 for PI; E_{Cu} = 119 GPa and v_{Cu} = 0.34 for copper; $E_{Silbione}$ = 0.8 MPa and $v_{Silbione}$ = 0.5 for Silbione; $E_{Ecoflex}$ = 60 kPa and $v_{Ecoflex}$ = 0.5 for Ecoflex; and E_{Skin} = 130 kPa and v_{Skin}= 0.5 for the skin.

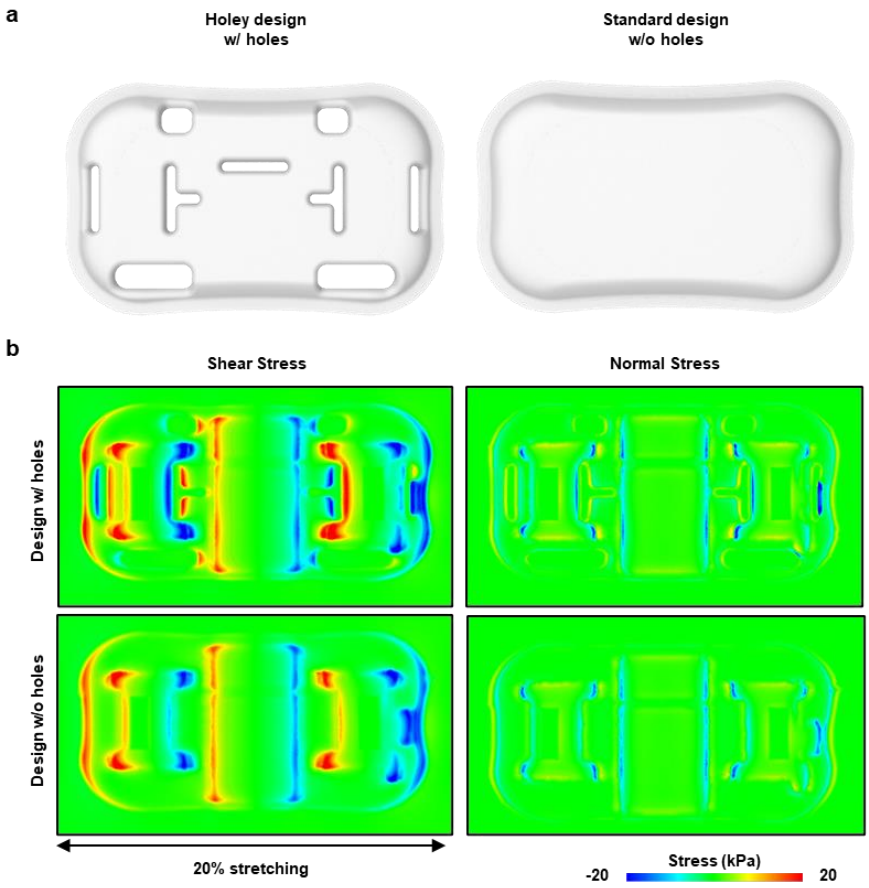

Figure 4.3. Computed results for shear and normal stress at the interface between holey and non-holey device designs and skin. (A) Illustration of the holey and non-holey device designs. (B) Computed shear and normal stresses in the skin are simulated after 20% stretching.

4.4.

Mechanics of Pre-Curved Designs

Devices with pre-defined curvature further improve the mechanics at the skin interface. Applying conventional planar devices onto the surfaces of the body requires bending. The associated bending-induced stresses can promote delamination in certain cases, and they can cause skin irritation in others. Both effects are pronounced for premature neonates due to their small, highly curved anatomical features and their fragile skin [117 , 118]. The mitigation

strategy introduced here exploits encapsulation layers formed in curved geometries approximatelymatched to those of the desired mounting location and size/age of the baby. Figure 4.4A shows devices with planar and curved shapes. The examples here involve bending radii (angle) of 108 mm (30°) and 54 mm (60°) matched to the chest circumference of pediatric patients (11 - 12 ages: approximately 65-70 cm) [119] and newborns (30-35 cm) [120]. When attaching the device to the surfaces of skin with different curvatures (planar, 30^{o} curved, 60^{o} curved), mismatch with the curvature of device results in a resilience associated with elastic forces directed toward returning the bent device to its original shape as shown in Figure 4.4B.

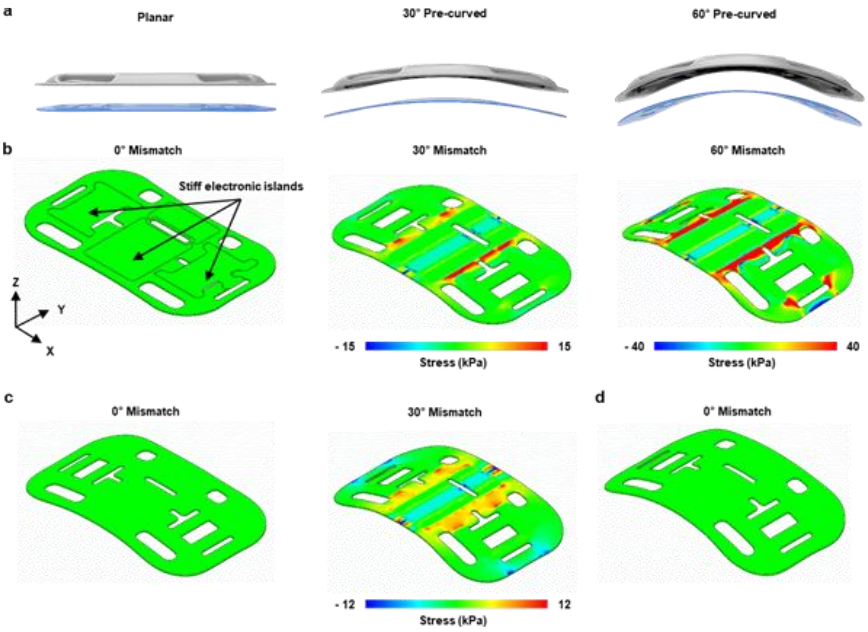

Figure 4.4.

Pre-curved holey ECG devices with different curvatures. (A) Images of (left) planar, (middle) 30° and (right) 60° pre-curved designs. Comparison of computed stresses induced by the resilience from curvature mismatch between the skin and the device (B) The planar device for 0°, 30° and 60° mismatch. (C) The 30° pre-curved device for 30° mismatch. d, The 60° pre-curved device for 0° mismatch.

The stresses caused by this resilience appear most prominently near the islands of the device due to their large stiffnesses compared to those of the encapsulation structures (Figure 4.4B). For the planar device, the maximum stress is -15 kPa (compression) and 15 kPa (tension), -28 kPa (compression) and 38 kPa (tension) for cases of 30^o and 60^o mismatch in curvature, respectively. For the cases of devices with pre-curvatures of 30^o (Figure 4.4C), the maximum stresses are -12 kPa (compression) and 7 kPa (tension) for a curvature mismatch of 30^o. All cases where the curvatures are matched (= 0^o mismatch) exhibit zero stress. Figure 4.5 shows the calculations of stress distributions for such devices mounted on skin with matching curvature and tangentially stretched to 20%. The interfacial stresses are below the somatosensory pressure range (20 kPa) of the skin even whenthe skin is stretched by 15% [121]. The FEA results in Figure 4.5B show that the pre-curved encapsulation approach reduces the stress to the skin. These effects minimize mechanically induced irritation to the skin and promote robust interfaces.

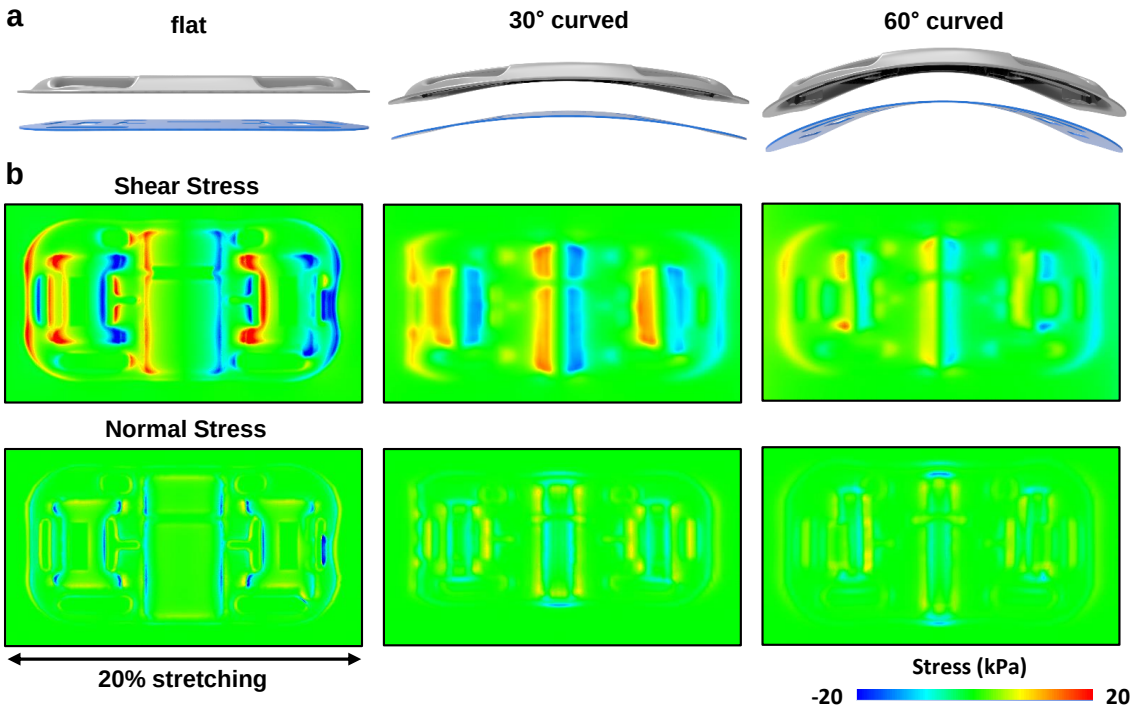

Figure 4.5. Stresses at the device-skin interface of curved holey ECG devices with different curvatures. (A) Images of (left) planar,(middle) 30° and (right) 60° pre-curved designs. (B) comparison of computed shear (top) and normal (bottom) stresses from curvature matching between the skin and the planar device for 0°, 30° and 60° match..

4.5.

Water Diffusion Modeling for Adhesion to the Skin

The process of removing devices from the skin can cause iatrogenic injuries. Thin, soft, and wireless devices significantly reduce the strength of adhesionnecessary to support robust bonding compared to that required for conventional wired sensors [110]. Nevertheless, separate, triggering mechanisms to reduce the adhesion to facilitate release can be valuable. In a strategy introduced here, water applied to the holes and the surrounding perimeter of the device cause swelling of a hydrogel bonding layer, thereby reducing the strength of adhesion dramatically, even to levels that

can be considered negligible [112–114]. Figure 4.6A shows the basic effect, measured as peel force required to remove arectangular hydrogel adhesive (10 X 30 mm^2, thickness ~815 μm) attached to a glass slide, as a function of time of immersion in water at temperatures of 25 ^oC and 35 ^oC [122, 123]. The diffusion coefficient for water through the hydrogel (~1.2 mm^2/min) at 35 ^oC is approximately twice as large as that (~0.6 mm^2/min) at 25 ^oC, thereby resulting in a correspondingly higher swelling rate and a more rapid reduction in peel force [124–126]. Complete loss of adhesion, to within measurement uncertainties, occurs in 7 and 11 minutes at 35 ^oC and 25 ^oC, respectively. The 35 ^oC case, close to the temperature of the skin, is most relevant for applications considered here. Experimental measurements of peeling force for devices adhered to the back of the handof an adult volunteer subject show trends consistent with modeling of the diffusion in the hydrogel geometry in Figure 4.6B and water concentration as a function of time in Figure 4.6C for different design layouts. Initially, all designs (non-holey, holey, and holey with microchannels) have peeling forces in the range of 5-7 N. Even after immersion in water at 35°C for 10 minutes, the peeling force of the non-holeydevice shows the smallest reduction, still larger than 5.0 N, and the peeling force of the holey example is about 2.0 N. At that time, the peeling force of the holey with microchannels decreases by the largest amount, to a value less than 0.6 N. After 20 min, the device with holeydesign and microchannels exhibits zero adhesion, to within experimental uncertainties as shown in Figure 4.6D.

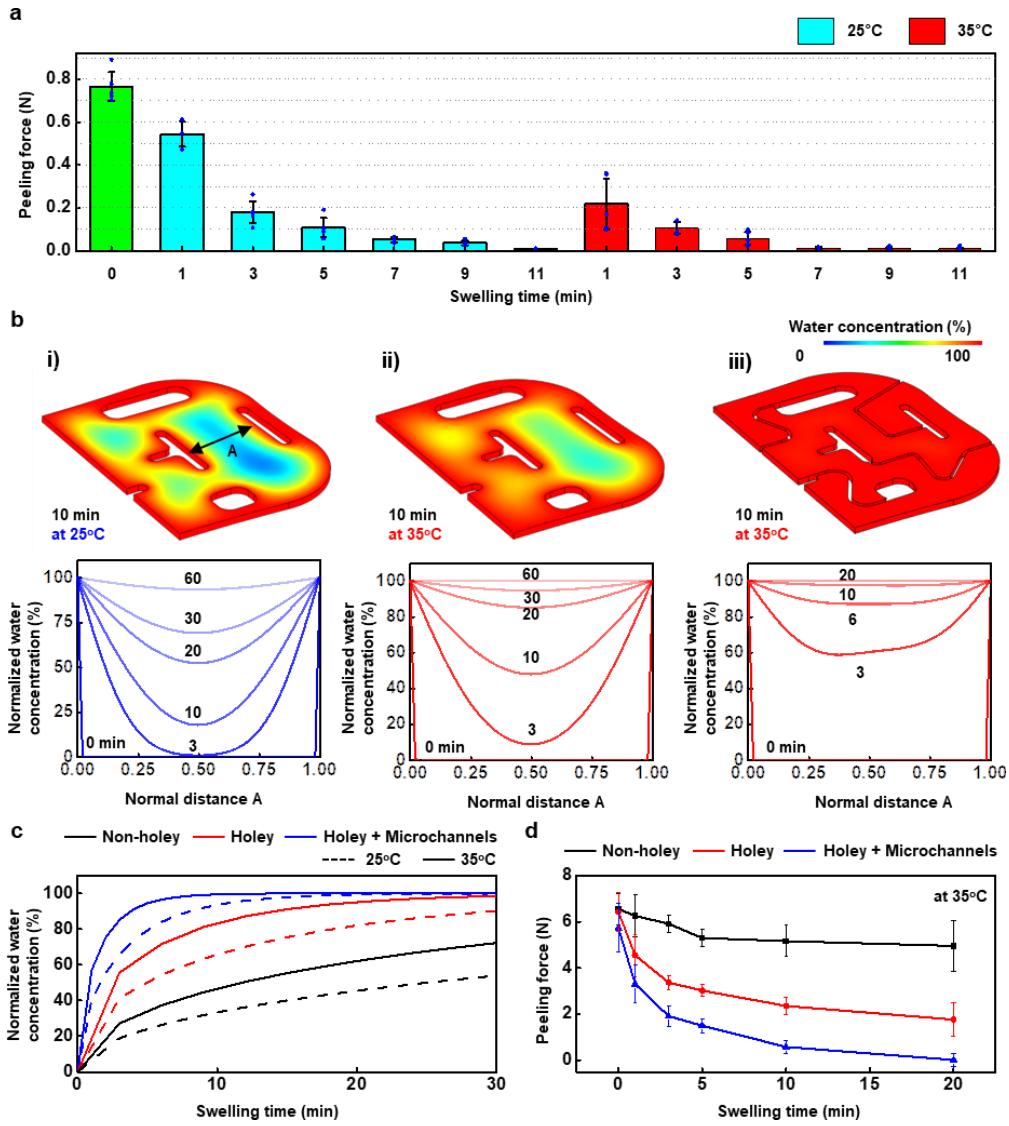

Figure 4.6. Water triggered soft release of the hydrogel adhesive. (A) Peel force of hydrogel adhesive as a function of swelling time and water temperature (25 ^{o}C and 35 ^{o}C). (B) Computed swelling model of the hydrogel adhesive during water diffusion through the holey device and the difference in water concentration of the hydrogel adhesive as a function of swelling time, water temperature, and adhesive design; (i) holey design at 25 ^{o}C, (ii) holey design at 35 ^{o}C and (iii) holey design with microchannels at 35 ^{o}C. (C) Comparison of water concentration averaged across the entire volumes of these different designs, at these two temperatures. (D) Comparison of peeling force as a function of swelling time for hydrogel adhesives with differentdesigns: non-holey, holey, and holey with micro-channels for water at 35^{o}C..

Without holes, this release mechanism is not practical because water can be introduced only around the perimeter of the device. The hydrogel adhesive consists of two separate pieces,

one for each of the ECG electrodes. The widths of each piece are equal to half of that of the entire device. As such, the minimum diffusion distance is equal to one quarter of the width of the device (~13.6 mm) for complete wetting of the hydrogel. The holes represent additional points of access that also simultaneously act as reservoirs, to reduce this distance. For the configuration of holes examined here, this reduction corresponds to a factor of ~2 (~6.7 mm). Given the quadratic dependence of diffusion distance on time [124] shown in Figure 4.7 this reduction translates to a decrease in the time to achieve saturation by a factor of ~4.

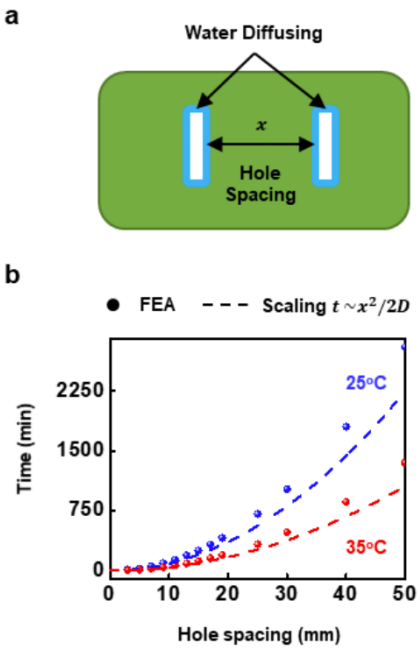

Figure 4.7. Computed diffusion time as a function distance between the holes. (A) Schematic illustration of the hydrogel adhesive with two holes as a starting point for water diffusion. (B) Time when all the water reaches the hydrogel adhesive, as a function of the hole spacing, using measured diffusion coefficients (5.56 x10^{-7} m^2/min at 25 °C and 1.18 x 10^{-6} m^2/min at 35 °C).

To reduce further the minimum diffusion distance and saturation time, the holes can serve as the origins for features that facilitate lateral transport. Here, water introduced into the holes flows

throughmicrochannels (width: 500 μm, thickness: thickness 812.8 μm) cut into the hydrogel itself as shown by the 2D schematic in Figure 4.8A and the 3D view in Figure 4.8B. These features further reduce the minimum diffusion distance (to ~3 mm), corresponding to a reduction of saturation time by another factor of more than four (~4.4 times) and by nearly twenty times compared to that of a conventional design, without holes or microchannels. Figure 4.8C, shows simulation results that use measured diffusion coefficients of hydrogel adhesive for water at 25 ^{o}C and 35 ^{o}C to compare these various cases (non-holey, holey, and holey with microchannels). The hydrogel adhesive has an initial water content of 23%, as a baseline for calculating the normalized water concentration due to diffusion.

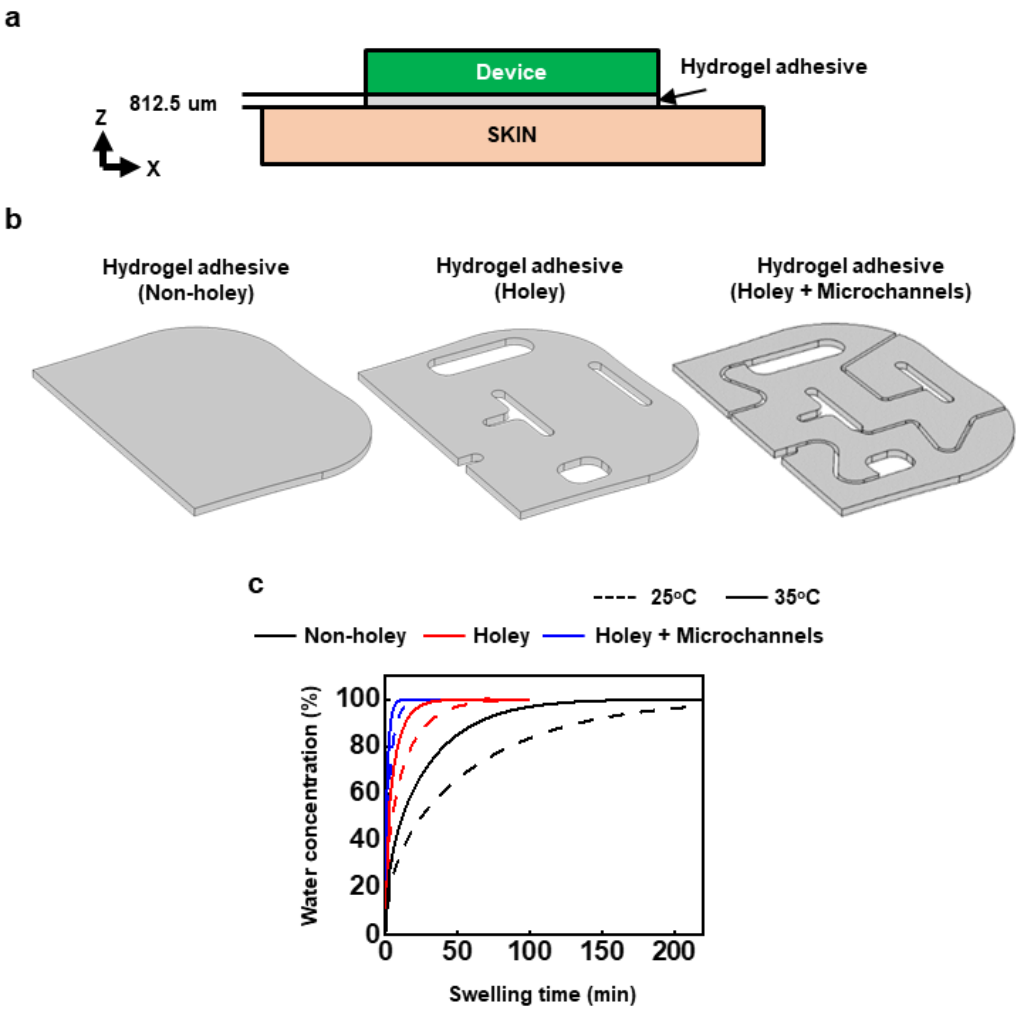

Figure 4.8. Modeling results of diffusion for different hydrogel adhesive designs at 25 °C and 35 °C. (A) Schematic illustration of the device attached on the skin using the hydrogel adhesive. (B) Three hydrogel adhesive designs such as non-holey, holey, and holey with microchannels. (C) Normalized water concentration as a function of time for hydrogel swelling at 25 °C and 35 °C for three hydrogel adhesive designs.

FEA results capture the diffusion of water over the swelling time for each design of the hydrogel adhesive, as changes in the normalized water concentration with distance (line marked A in Figure 4.6B) and through the entire volume as shown by the panels in Figure 4.6B. In the holey design, the center point of this line reaches a normalized water concentration of ~20% and 50% at

10 min for temperatures of 25°C and 35 °C, respectively. For the holey design with microchannels, the concentration reaches 90% at 10 min for 35 °C. Figure 4.8C shows the calculated saturation times for these three designs at 25 and 35 °C. The holey design with microchannels at 35 °C exhibits a saturation time that is ~27.5 times (8 min) smaller than that (220 min) of the non- holey case at 25 °C. Water diffusion simulation in the hydrogel: COMSOL, a commercial Multiphysics FEA software, was used to model the water concentration as a function of time in the non-holey, holey, and holey + microchannels hydrogel adhesive layouts at 25 °C and 35 °C shown in Figure 4.6, Figure 4.7, and Figure 4.8. The objective of the analysis was to determine the total diffusion time and optimize the holey + microchannel configuration for faster diffusion. The time-dependent diffusion is modeled according to

$$\frac{\partial c}{\partial t} + \nabla \cdot (-D\nabla c) = 0 \tag{4.1}$$

where, D is the diffusion coefficient (m^2/min), c is the water concentration (mol/m^3), and t is time (min). [124] The hydrogel (~812.5 μm thick) was modeled using tetrahedral elements and the total number of elements in the model is ~ 340,000. The diffusion model used in the simulation are determined from experiments as $D = 5.56 \times 10^{-7}$ m^2/min at 25 °C and $D = 1.18 \times 10^{-6}$ m^2/min at 35 °C.

4.6. Summary

This chapter introduces materials and design concepts for thin, soft wireless devices that can continuously monitor key vital signs, such as HR, RR and temperature, and body motion/movements, with a focus on patients in the NICU and PICU. Key features include holey architectures, pre-curved layouts, and structured hydrogel adhesives. The locations, dimensions and shapes of the holes improve the bending and stretching mechanics, to reduce irritation at the skin interface during device application, use and removal. Pre-curved shapes that match those of the targeted region of the anatomy further decrease the stresses on the surface of the skin, to values close to zero. In addition to these mechanical and geometrical advantages, the holey designs enable i) soft release of devices from the skin triggered by introduction of warm water through the holes and into microchannels molded on thin, hydrogel skin adhesives, ii) reduced accumulation of interfacial moisture from transepidermal water loss via enhanced rates of permeation through the holes, iii) visual inspection of the skin condition in the regions of the holes, without the need to remove the devices. The outcomes of this work have the potential to enhance the quality of care for the neonates in all contexts, from the most advanced hospital settings to rural or remote health clinics in resource-constrained areas.

CHAPTER 5

Conclusions

This dissertation focuses on the design and optimization of bioelectronics platforms for skin-integrated and implantable bioelectronic devices. The primary goal is to model and design programmable and mechanically compliant platforms that can wirelessly pace the heart, administer drugs, induce vibrotactile sensations, and monitor physiological signals.

Chapter 1 presents an analytical model that accurately describes the drug delivery process in microsystems with electrochemical actuation by considering the effects of microfluidic and flexible membrane resistance, which were ignored in previous models. Comparison between numerical, analytical, and experimental results demonstrate that the simple analytical model, derived from perturbation analysis and membrane theory, can be used to determine the drug delivery time and maximum flowrate in large and small microsystems used in for emerging applications in drug delivery studies.

Chapter 2 introduces a transient pacemaker platform that allows closed-loop modulation of heart rate over a timeframe that matches post-operative needs. The design of the temporary pacemaker combines mechanics and materials strategies to ensure a reliable mechanical and electromagnetic performance while ensuring a safe exposure to electromagnetic energy and avoid disruption of additional imagining studies (e.g., MRI).

Chapter 3 investigates the mechanical vibrations induced by three commercially available vibrotactile sensors used in recent haptic applications. Through a combination of numerical

modeling and digital image correlation experiments, the vibrotactile performance was systematically studied as a function of not only to actuator type but also to actuator design features such as those related to coil geometries, magnet properties, and overall layouts. For future applications, a combination of various types of actuators may ultimately be needed for robust, engaging haptic sensations through programmed engagement of different types of mechanoreceptors.

Chapter 4 introduces materials and design concepts for thin, soft wireless devices that can continuously monitor key vital signs and body motion/movements. These devices are designed for patients in the NICU and PICU where the interfacial stresses are minimized, and the mechanical performance is enhanced by design choices for holey architectures, pre-curved layouts, and structured hydrogel adhesives.

Lastly, this dissertation presents a comprehensive investigation into the design and optimization of bioelectronics platforms for skin-integrated and implantable bioelectronic devices. The results provide valuable insights into the development of novel bioelectronics technologies for medical applications. Future work will build on these findings to further advance the field of bioelectronics and engineer patient specific technologies.

REFERENCES

1. Ballington, D. A. & Anderson, R. J. *Pharmacy Practice for Technicians*. *Pharmacy Practice for Technicians* (Paradigm Publishing, 2007).
2. Tiwari, G. *et al.* Drug delivery systems: An updated review. *International Journal of Pharmaceutical Investigation* **2**, 2 (2012).
3. Park, K. Controlled drug delivery systems: Past forward and future back. *Journal of Controlled Release* **190**, 3–8 (2014).
4. Cobo, A., Sheybani, R. & Meng, E. MEMS: Enabled Drug Delivery Systems. *Advanced Healthcare Materials* **4**, 969–982 (2015).
5. Meng, E. & Hoang, T. MEMS-enabled implantable drug infusion pumps for laboratory animal research, preclinical, and clinical applications. *Advanced Drug Delivery Reviews* **64**, 1628–1638 (2012).
6. Grayson, A. C. R., Shawgo, R. S., Li, Y. & Cima, M. J. Electronic MEMS for triggered delivery. *Advanced Drug Delivery Reviews* **56**, 173–184 (2004).
7. Cameron, C. G. & Freund, M. S. Electrolytic actuators: Alternative, high-performance, material-based devices. *Proceedings of the National Academy of Sciences of the United States of America* **99**, 7827–7831 (2002).
8. Nguyen, N. T., Huang, X. & Chuan, T. K. MEMS-micropumps: A review. *Journal of Fluids Engineering, Transactions of the ASME* **124**, 384–392 (2002).
9. Amirouche, F., Zhou, Y. & Johnson, T. Current micropump technologies and their biomedical applications. *Microsystem Technologies* **15**, 647–666 (2009).

10. Laser, D. J. & Santiago, J. G. A review of micropumps. *Journal of Micromechanics and Microengineering* **14**, (2004).

11. Gensler, H., Sheybani, R., Li, P. Y., Mann, R. lo & Meng, E. An implantable MEMS micropump system for drug delivery in small animals. *Biomedical Microdevices* **14**, 483–496 (2012).

12. Cobo, A. M., Tu, H. M., Sheybani, R. & Meng, E. Characterization of a wireless implantable infusion micropump for small animal research under simulated in vivo conditions. *IEEE 2014 Biomedical Circuits and Systems Conference, BioCAS 2014 - Proceedings* 348–351 (2014) doi:10.1109/BioCAS.2014.6981734.

13. Trull, F. L. & Rich, B. A. More Regulation of Rodents. *Science* **284**, 1463 (1999).

14. Young, D. B., Jackson, T. E., Pearce, D. H. & Guyton, A. C. A Portable Infusion Pump for Use on Large Laboratory Animals. *IEEE Transactions on Biomedical Engineering* **BME-24**, 543–545 (1977).

15. Zhang, Y. *et al.* Battery-free, lightweight, injectable microsystem for in vivo wireless pharmacology and optogenetics. *Proceedings of the National Academy of Sciences of the United States of America* **116**, 21427–21437 (2019).

16. Zhang, Y. *et al.* Battery-free, fully implantable optofluidic cuff system for wireless optogenetic and pharmacological neuromodulation of peripheral nerves. *Science Advances* **5**, 1–12 (2019).

17. Spieth, S. *et al.* An intra-cerebral drug delivery system for freely moving animals. *Biomedical Microdevices* **14**, 799–809 (2012).

18. Jeong, J. W. *et al.* Wireless Optofluidic Systems for Programmable In Vivo Pharmacology and Optogenetics. *Cell* **162**, 662–674 (2015).

19. Staples, M. Microchips and controlled-release drug reservoirs. *Wiley Interdisciplinary Reviews: Nanomedicine and Nanobiotechnology* **2**, 400–417 (2010).

20. Tng, D. J. H., Hu, R., Song, P., Roy, I. & Yong, K. T. Approaches and challenges of engineering implantable microelectromechanical systems (MEMS) drug delivery systems for in vitro and in vivo applications. *Micromachines* **3**, 615–631 (2012).

21. Li, P. Y. *et al.* An electrochemical intraocular drug delivery device. *Sensors and Actuators, A: Physical* **143**, 41–48 (2008).

22. Pang, C., Tai, Y. C., Burdick, J. W. & Andersen, R. A. Electrolysis-based diaphragm actuators. *Nanotechnology* **17**, 64–68 (2006).

23. Neagu, C., Jansen, H., Gardeniers, H. & Elwenspoek, M. Electrolysis of water: An actuation principle for MEMS with a big opportunity. *Mechatronics* **10**, 571–581 (2000).

24. Neagu, C. R., Gardeniers, J. G. E., Elwenspoek, M. & Kelly, J. J. An electrochemical microactuator: Principle and first results. *Journal of Microelectromechanical Systems* **5**, 2–9 (1996).

25. Stanczyk, T., Ilic, B., Hesketh, P. J. & Boyd IV, J. G. Microfabricated electrochemical actuator for large displacements. *Journal of Microelectromechanical Systems* **9**, 314–320 (2000).

26. Böhm, S., Olthuis, W. & Bergveld, P. An Integrated Micromachined Electrochemical Pump and Dosing System. *Biomedical Microdevices* **1**, 121–130 (1999).

27. Li, P. Y., Sheybani, R., Gutierrez, C. A., Kuo, J. T. W. & Meng, E. A parylene bellows electrochemical actuator. *Journal of Microelectromechanical Systems* **19**, 215–228 (2010).

28. Kabata, A. *et al.* Prototype micropump for insulin administration based on electrochemical bubble formation. *Journal of Pharmaceutical Sciences* **97**, 5037–5045 (2008).

29. Cobo, A., Sheybani, R., Tu, H. & Meng, E. A wireless implantable micropump for chronic drug infusion against cancer. *Sensors and Actuators, A: Physical* **239**, 18–25 (2016).

30. Gensler, H. *et al.* Implantable MEMS drug delivery device for cancer radiation reduction. *2010 IEEE 23rd International Conference on Micro Electro Mechanical Systems (MEMS)* (2010).

31. Urquhart, J., Fara, J. A. & Willis, K. L. Rate-controlled delivery systems in drug and hormone research. *Annual Review of Pharmacology and Toxicology* **24**, 199–236 (1984).

32. Ashraf, M. W., Tayyaba, S. & Afzulpurkar, N. Micro Electromechanical Systems (MEMS) based microfluidic devices for biomedical applications. *International Journal of Molecular Sciences* **12**, 3648–3704 (2011).

33. Smolensky, M. H. & Peppas, N. A. Chronobiology, drug delivery, and chronotherapeutics. *Advanced Drug Delivery Reviews* **59**, 828–851 (2007).

34. Youan, B. B. C. Chronopharmaceutics: Gimmick or clinically relevant approach to drug delivery? *Journal of Controlled Release* **98**, 337–353 (2004).

35. Lee, D. E., Soper, S. A. & Wang, W. Fabrication and mathematical analysis of an electrochemical microactuator (ECM) using electrodes coated with platinum nano-particles. *Microsystem Technologies* **16**, 381–390 (2010).

36. Sheybani, R. & Meng, E. High efficiency wireless electrochemical actuators: Design, fabrication and characterization by electrochemical impedance spectroscopy. *Micro Electro Mechanical Systems (MEMS), 2011 IEEE 24th International Conference, (Institute of Electrical and Electronics Engineers)* 1233–1236 (2011) doi:10.1109/MEMSYS.2011.5734655.

37. Mooney, M., A theory of large elastic deformation, *Journal of Applied Physics*, **11**, 582–592 (1940).

38. Marlow, R.S., A General First-Invariant Hyperelastic Constitutive Model. In: *Constitutive Models for Rubber III*, Busfield, J. (Ed.). AA Balkema Publishers, UK., pp: 157-160 (2003).

39. Dassault Systèmes. *Abaqus 6.11 Theory Manual*. vol. IV (2013).

40. Timoshenko, S., Woinowsky-Krieger, S. "*Symmetrical Bending of Circular Plates" in Theory of plates and shells.* (New York: McGraw-Hill, 1959). pp 51-78

41. Kumar, M. & Parul, Methods for solving singular perturbation problems arising in science and engineering. *Mathematical and Computer Modelling* **54**, 556–575 (2011).

42. Avila, R. *et al.* Electrochemical bioelectronics in drug delivery - effect of the initial gas volume. *Journal of Applied Mechanics* **89,** 011012 (2022).

43. Avila, R. *et al.* A mechanics model for injectable microsystems in drug delivery. *Journal of the Mechanics and Physics of Solids* **156**, 104622 (2021).

44. Avila, R. *et al.* Modeling programmable drug delivery in bioelectronics with electrochemical actuation. *Proceedings of the National Academy of Sciences of the United States of America* **118,** e2026405118 (2021).

45. Zoll, P.M. *et al.* External noninvasive temporary cardiac pacing: clinical trials *Circulation* **71**, 937–944 (1985).

46. Curtis, J.J. *et al.* A critical look at temporary ventricular pacing following cardiac surgery. *Surgery* **82**, 888–893 (1977).

47. Wilhelm, M.J. *et al.* Cardiac pacemaker infection: surgical management with and without extracorporeal circulation. *The Annals of Thoracic Surgery* **64**, 1707–1712 (1997).

48. Choo, M.H. *et al.* Permanent pacemaker infections: characterization and management. *American Journal of Cadiology* **48**, 559–564 (1981).

49. Imparato, A.M. & Kim, G.E. Electrode complications in patients with permanent cardiac pacemakers. *The Archives of Surgery* **105**, 705–710 (1972).

50. Bernstein, V., Rotem, C.E. & Peretz, D.I. Permanent pacemakers: 8-year follow-up study. Incidence and management of congestive cardiac failure and perforations. *Annals of Internal Medicine* **74**, 361–369 (1971).

51. Hartstein, A.I., Jackson, J. & Gilbert, D.N. Prophylactic antibiotics and the insertion of permanent transvenous cardiac pacemakers. *The Journal of Thoracic and Cardiovascular Surgery* **75**, 219–223 (1978).

52. Austin, J.L., Preis, L.K., Crampton, R.S., Beller, G.A. & Martin, R.P. Analysis of pacemaker malfunction and complications of temporary pacing in the coronary care unit. *American Journal of Cardiology* **49**, 301–306 (1982).

53. Lumia, F.J. & Rios, J.C. Temporary transvenous pacemaker therapy: an analysis of complications. *Chest* **64**, 604–608 (1973).

54. Donovan, K.D. & Lee, K.Y. Indications for and complications of temporary transvenous cardiac pacing. *Anaesthesia and Intensive Care* **13**, 63–70 (1985).

55. Braun, M.U. *et al.* Percutaneous lead implantation connected to an external device in stimulation-dependent patients with systemic infection – a prospective and controlled study. *Pacing and Clinical Electrophysioly* **29**, 875–879 (2006).

56. Del Nido, P. & Goldman, B.S. Temporary epicardial pacing after open heart surgery: complications and prevention. *Journal of Cardiac Surgery* **4**, 99–103 (1989).

57. Elmistekawy, E. Safety of temporary pacemaker wires. *Asian Cardiovascular and Thoracic Annals* **27**, 341–346 (2019).

58. Gutruf, P. *et al.* Wireless, battery-free, fully implantable multimodal and multisite pacemakers for applications in small animal models. *Nature Communications* **10**, 5742 (2019).

59. Koo, J. *et al.* Wireless bioresorbable electronic system enables sustained nonpharmacological neuroregenerative therapy. *Nature Medicine* **24**, 1830–1836 (2018).

60. Choi, Y.S. *et al.* Stretchable, dynamic covalent polymers for soft, long-lived bioresorbable electronic stimulators designed to facilitate neuromuscular regeneration. *Nature Communications* **11**, 5990 (2020).

61. Won, S.M. *et al.* Natural wax for transient electronics. *Advanced Funcitonal Materials* **28**, 1801819 (2018).

62. Choi, Y.S., Koo, J. & Rogers, J.A. Inorganic materials for transient electronics in biomedical applications. *MRS Bulletin* **45**, 103–112 (2020).

63. Makadia, H.K. & Siegel, S.J. Poly lactic-co-glycolic acid (PLGA) as biodegradable controlled drug delivery carrier. *Polymers (Basel)* **3**, 1377–1397 (2011).

64. Hwang, S.W. *et al.* Dissolution chemistry and biocompatibility of single-crystalline silicon nanomembranes and associated materials for transient electronics. *ACS Nano* **8**, 5843–5851 (2014).

65. Yin, L. *et al.* Mechanisms for hydrolysis of silicon nanomembranes as used in bioresorbable electronics. *Advanced Materials* **27**, 1857–1864 (2015).

66. Pichorim, S.F. *Design of circular and solenoid coils for maximum mutual inductance*. In Proc.14th International Symposium on Biotelemetry 71–77 (Tectum, 1998).

67. Kurs, A, *et al.* Wireless power transfer via strongly coupled magnetic resonances. *Science* **317**, 83–86 (2007).

68. Rahko, P.S. Evaluation of the skin-to-heart distance in the standing adult by two-dimensional echocardiography. *Journal of the American Society of Echocardiography* **21**, 761–764 (2008).

69. Winter, K.F., Hartmann, R. & Klinke, R. A. stimulator with wireless power and signal transmission for implantation in animal experiments and other applications. *Journal of Neuroscience Methods* **79**, 79–85 (1998).

70. Dinis, H., Colmiais, I. & Mendes, P.M. Extending the limits of wireless power transfer to miniaturized implantable electronic devices. *Micromachines* **8**, 359 (2017).

71. Sperelakis, N. & Hoshiko, T. Electrical impedance of cardiac muscle. *Circulation Research* **9**, 1280–1283 (1961).

72. Fry, C. H. *et al.* Cytoplasm resistivity of mammalian atrial myocardium determined by dielectrophoresis and impedance methods. *Biophysical Journal* **103**, 2287–2294 (2012).

73. Gabriel, S., Lau, R. W. & Gabriel, C. The dielectric properties of biological tissues: II. Measurements in the frequency range 10 Hz to 20 GHz. *Physics in Medicien & Biology* **41**, 2251–2269 (1996).

74. Rong, C. *et al.* Analysis of wireless power transfer based on metamaterial using equivalent circuit. *The Journal of Engineering* **2019**, 2032–2035 (2019).

75. Choi, S. & Kuchenbecker, K.J. Vibrotactile display: Perception, technology, and applications. *Proceedings of the IEEE* **101**, 2093-2104 (2012).

76. Jung, Y.H., Kim, J.H., & Rogers, J.A. Skin-Integrated Vibrohaptic Interfaces for Virtual and Augmented Reality. *Advanced Functional Materials* **31**, 2008805 (2021).

77. Jung, Y.H. *et al.* A wireless haptic interface for programmable patterns of touch across large areas of the skin. *Nature Electronics* **5**, 374-385 (2022).

78. Kim, M., Lee, S. & Choi, S. Saliency-driven real-time video-to-tactile translation. *IEEE Transactions on Haptics* **7**, 394-404 (2013).

79. Cheng, A., Nichols, K.A., Weeks, H.M., Gurari, N. & Okamura, A.M. Conveying the configuration of a virtual human hand using vibrotactile feedback, *2012 IEEE Haptics Symposium (HAPTICS)*, IEEE, pp. 155-162 (2012).

80. Dementyev, A., Getreuer, P., Kanevsky, D., Slaney, M. & Lyon, R.F. VHP: Vibrotactile Haptics Platform for On-body Applications, *The 34th Annual ACM Symposium on User Interface Software and Technology*, pp. 598-612 (2021).

81. Mortimer, B.J., Zets, G.A. & Cholewiak, R.W. Vibrotactile transduction and transducers. *The Journal of the Acoustical Society of America* **121**, 2970-2977 (2007).

82. Jones, L.A. & Singhal, A. Perceptual dimensions of vibrotactile actuators. *2018 IEEE Haptics Symposium (HAPTICS)*, IEEE , pp. 307-312 (2018).

83. Azadi, M. & Jones, L.A. Vibrotactile actuators: Effect of load and body site on performance. *2014 IEEE Haptics Symposium (HAPTICS)*, IEEE, pp. 351-356 (2014).

84. Handler, A. & Ginty, D.D. The mechanosensory neurons of touch and their mechanisms of activation. *Nature Reviews Neuroscience* **22**, 521-537 (2021).

85. Lamoré, P. & Keemink, C. Evidence for different types of mechanoreceptors from measurements of the psychophysical threshold for vibrations under different stimulation conditions. *The Journal of the Acoustical Society of America* **83**, 2339-2351 (1988).

86. Makous, J.C., Gescheider, G.A. & Bolanowski, S.J. The effects of static indentation on vibrotactile threshold. *The Journal of the Acoustical Society of America* **99**, 3149-3153 (1996).

87. Moore, T.J. & Mundie, J.R. Measurement of specific mechanical impedance of the skin: effects of static force, site of stimulation, area of probe, and presence of a surround. *The Journal of the Acoustical Society of America* **52**, 577-584 (1972).

88. Sofia, K.O. & Jones, L. Mechanical and psychophysical studies of surface wave propagation during vibrotactile stimulation. *IEEE Transactions on Haptics* **6**, 320-329 (2013).

89. Shah, V.A., Casadio, M., Scheidt, R.A. & Mrotek, L.A. Vibration Propagation on the Skin of the Arm. *Applied Sciences* **9**, 4329 (2019).

90. Morales-Hurtado, M., Zeng, X., Gonzalez-Rodriguez, P., Ten Elshof, J.E. & van der Heide, E. A new water absorbable mechanical Epidermal skin equivalent: The combination of hydrophobic PDMS and hydrophilic PVA hydrogel, *Journal of the Mechanical Behavior of Biomedical Materials* **46**, 305-317 (2015).

91. Kalra, A., Lowe, A. & Al-Jumaily, A. Mechanical behaviour of skin: a review. *Journal of Material Science & Engineering* **5**, 1000254 (2016).

92. Li, C., Guan, G., Reif, R., Huang, Z. & Wang R.K. Determining elastic properties of skin by measuring surface waves from an impulse mechanical stimulus using phase-sensitive optical coherence tomography. *Journal of The Royal Society Interface* **9**, 831-841 (2012).

93. Wheeler, D. S. & Wong, H. R. *Pediatric Critical Care Medicine: Basic Science And Clinical Evidence* (Springer Science & Business Media 2007).

94. Xu, J. Murphy, S. L., Kochanek, K. D., Bastian, B. & Arias, E. Deaths: Final Data for 2016. *National Vital Statistics Report* **67**, 1-76 (2018).

95. Bonner, O. Beardsall, K. Crilly, N. & Lasenby, J. 'There were more wires than him': the potential for wireless patient monitoring in neonatal intensive care. *BMJ Innovations **3***, 12-18 (2017).

96. Cartlidge, P.H.T., Fox, P. E. & Rutter, N. The scars of newborn intensive care. *Early Human Development* **21**, 1-10 (1990).

97. Lund, C. Medical Adhesives in the NICU. *Newborn and Infant Nursing Reviews* **14**, 160-165 (2014).

98. Tottman, A. C. Alsweiler, J. M. Bloomfield, F. H. & Harding, J. E. Presence and pattern of scarring in children born very preterm. *Archives of Disease in Childhood - Fetal and Neonatal Edition* **103**, F277-F279 (2018).

99. Kim, D.-H. *et al.* Epidermal Electronics. *Science* **333**, 838-43 (2011).

100. Gao, W. *et al.* Fully integrated wearable sensor arrays for multiplexed in situ perspiration analysis. *Nature* **529**, 509-514 (2016).

101. Walsh, J. A., Topol, E. J. & Steinhubl, S. R. Novel wireless devices for cardiac monitoring. *Circulation* **130**, 573-81 (2014).

102. Jang, K.-I. *et al.* Self-assembled three dimensional network designs for soft electronics. *Nature Communications* **8**, 15894 (2017).

103. Heo, S. Y. *et al.* Wireless, battery-free, flexible, miniaturized dosimeters monitor exposure to solar radiation and to light for phototherapy. *Science Translational Medicine* **10**, eaau1643 (2018).

104. Park, Y. *et al.* Wireless, skin-interfaced sensors for compression therapy. *Science Advances* **6**, eabe1655 (2020).

105. Rwei, A. Y. *et al.* A wireless, skin-interfaced biosensor for cerebral hemodynamic monitoring in pediatric care. *Proceedings of the National Academy of Sciences if the United States of America* **117**, 31674-31684 (2020).

106. Vogl, J. L. *et al.* Kangaroo father care: A pilot feasibility study of physiologic, biologic, and psychosocial measures to capture the effects of father–infant and mother–infant skin-to-skin contact in the Neonatal Intensive Care Unit. *Develomental Psychobiology* **63**, 1521-1533 (2021).

107. Jeong, H. *et al.* Differential cardiopulmonary monitoring system for artifact-canceled physiological tracking of athletes, workers, and COVID-19 patients. *Science Advances* **7**, eabg3092 (2021).

108. Liu, C. *et al.* Wireless, skin-interfaced devices for pediatric critical care: application to continuous, noninvasive blood pressure monitoring. *Advanced Healthcare Materials* **10**, 2100383 (2021).

109. Chung, H. U. *et al.* Binodal, wireless epidermal electronic systems with in-sensor analytics for neonatal intensive care. *Science* **363**, eaau0780 (2019).

110. Chung, H. U. *et al.* Skin-interfaced biosensors for advanced wireless physiological monitoring in neonatal and pediatric intensive-care units. *Nature Medicine* **26**, 418-429 (2020).

111. Hadush, M.Y., Berhe, A.H. & Medhanyie, A.A. Foot length, chest and head circumference measurements in detection of Low birth weight neonates in Mekelle, Ethiopia: a hospital based cross sectional study. *BMC Pediatrics* **17**, 111 (2017).

112. Peak, C.W., Wilker, J.J. & Schmidt, G. A review on tough and sticky hydrogels. *Colloid and Polymer Science* **291**, 2031-2047 (2013).

113. Michel, R. *et al.* Interfacial fluid transport is a key to hydrogel bioadhesion. *Proceedings of the National Academy of Sciences of the United States of America* **116**, 738-743 (2019).

114. Du, X. *et al.* An anti-infective hydrogel adhesive with non-swelling and robust mechanical properties for sutureless wound closure. *Journal of Materials Chemistry B* **8**, 5682-5693 (2020).

115. Miyamoto, A. *et al.* Inflammation-free, gas-permeable, lightweight, stretchable on-skin electronics with nanomeshes. *Nature Nanotechnoly* **12**, 907-913 (2017).

116. Yoon, S., Seok, M., Kim, M. & Cho, Y.-H. Wearable porous PDMS layer of high moisture permeability for skin trouble reduction. *Scientific Reports* **11**, 938 (2021).

117. August, D.L., New, K., Ray, R.A. & Kandasamy, Y. Frequency, location and risk factors of neonatal skin injuries from mechanical forces of pressure, friction, shear and stripping: A systematic literature review. *Journal of Neonatal Nursing* **24**, 173-180 (2018).

118. Oranges, T., Dini, V. & Romanelli, M. Skin Physiology of the Neonate and Infant: Clinical Implications. *Advanced Wound Care* **4**, 587-595 (2015).

119. Patil, S.S., Patil, S.R. & Durgawale, P.M. Physical growth pattern among adolescents from Satara District: Using sitting height, leg length, and other anthropometric measurements. *Journal of Datta Meghe Institute of Medical Sciences University* **13**, 143 (2018).

120. Azevedo, I. G. *et al.* Chest circumference in full-term newborns: how can it be predicted? *BMC Pediatrics* **19**, 341 (2019).

121. Zhang, Y. *et al.* Theoretical and Experimental Studies of Epidermal Heat Flux Sensors for Measurements of Core Body Temperature. *Advanced Healthcare Materials* **5**, 119-127 (2016).

122. Lee, Y.M., Kim, S.H. & Cho, C.S. Synthesis and swelling characteristics of pH and thermoresponsive interpenetrating polymer network hydrogel composed of poly(vinyl alcohol) and poly(acrylic acid). *Journal of Applied Polymer Science* **62**, 301 (1996).

123. Kim, S.J. Park, S.J. & Kim, S.I. Swelling behavior of interpenetrating polymer network hydrogels composed of poly(vinyl alcohol) and chitosan. *Reactive and Functional Polymers* **55**, 53-59 (2003).

124. Crank, J. *The Mathematics of Diffusion, Second Edition* (Oxford University Press, NY, USA 1975**)**.

125. Shen, C.-H. & Springer, G.S. Moisture Absorption and Desorption of Composite Materials. *Journal of Composite Materials* **10**, 2-20 (1976).

126. Jang, H.S. *et al.* A Bezel-Less Tetrahedral Image Sensor Formed by Solvent-Assisted Plasticization and Transformation of an Acrylonitrile Butadiene Styrene Framework. *Advanced Materials* **30**, 1801256 (2018).

VITA

Raudel Avila was born in the city of El Paso, Texas and raised in Ciudad Juarez and Chihuahua in Mexico. He received a B.S. in Mechanical Engineering from The University of Texas at El Paso in 2017. After, he moved to Northwestern University to complete a Ph.D. in Mechanical Engineering under the supervision of Prof. Yonggang Huang where he collaborated extensively with Prof. John A. Rogers' group. Raudel's research focuses on modeling the mechanics and electromagnetics in bioelectronics for health care and biomedical applications using both numerical and analytical techniques. As a Ph.D. candidate, he published more than 40 journal papers, many as first or co-first author in high profile journals such as the Proceedings of the National Academy of Sciences, Extreme Mechanics Letters, Advanced Materials, and the Journal of the Mechanics and Physics of Solids. During his Ph.D., he received multiple national fellowships such as the National Science Foundation Graduate Research Fellowship and the Ford Foundation Pre-Doctoral Fellowship. In 2019, Raudel received the Outstanding Researcher Award from the International Institute of Nanotechnology at Northwestern University. In 2022, he was selected as a Future Trailblazer in Engineering by Purdue University for his potential impact in expanding representation and diversity in engineering. Lastly, in 2022, he received a Terminal Year Fellowship from Northwestern University.